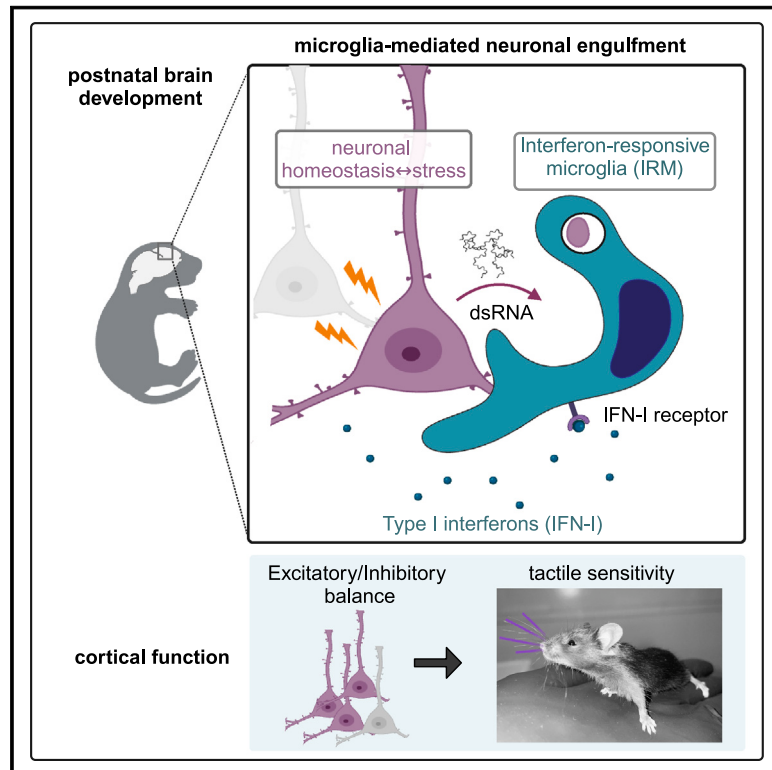


# Type-I-interferon-responsive microglia shape cortical development and behavior

## Graphical abstract



## Authors

Caroline C. Escoubas, Leah C. Dorman, Phi T. Nguyen, ..., Raul Andino, Tomasz J. Nowakowski, Anna V. Molofsky

## Correspondence

anna.molofsky@ucsf.edu

## In brief

A type-I-interferon-responsive microglial subset that engulfs neurons in the developing mouse cortex is required for normal cortical development and sensorimotor function. These data demonstrate a physiologic role for a canonical antiviral immune pathway in brain development.

## Highlights

- Type I interferon (IFN-I)-responsive microglia expand during developmental stress
- IFN-I-responsive microglial signature is conserved in brain pathology
- IFN-I-responsive microglia engulf whole neurons during cortical development
- IFN-I deficiency causes excitatory/inhibitory imbalance and tactile hypersensitivity



## Article

# Type-I-interferon-responsive microglia shape cortical development and behavior

Caroline C. Escoubas,<sup>1,18</sup> Leah C. Dorman,<sup>1,2,18</sup> Phi T. Nguyen,<sup>1,3</sup> Christian Lagares-Linares,<sup>1</sup> Haruna Nakajo,<sup>1</sup> Sarah R. Anderson,<sup>1</sup> Jerika J. Barron,<sup>1,3</sup> Sarah D. Wade,<sup>1,2</sup> Beatriz Cuevas,<sup>1,2</sup> Ilia D. Vainchtein,<sup>1</sup> Nicholas J. Silva,<sup>1</sup> Ricardo Guajardo,<sup>1,2,4</sup> Yinghong Xiao,<sup>5</sup> Peter V. Lidsky,<sup>5</sup> Ellen Y. Wang,<sup>1,6</sup> Brianna M. Rivera,<sup>7</sup> Sunrae E. Taloma,<sup>1,2</sup> Dong Kyu Kim,<sup>1</sup> Elizaveta Kaminskaya,<sup>1</sup> Hiromi Nakao-Inoue,<sup>1</sup> Bjoern Schwer,<sup>1,8,9,10,11,12</sup> Thomas D. Arnold,<sup>13</sup> Ari B. Molofsky,<sup>14</sup> Carlo Condello,<sup>7,15</sup> Raul Andino,<sup>5</sup> Tomasz J. Nowakowski,<sup>1,8,9,10,16,17</sup> and Anna V. Molofsky<sup>1,8,10,19,20,\*</sup>

<sup>1</sup>Departments of Psychiatry and Behavioral Sciences/Weill Institute for Neurosciences, University of California, San Francisco, San Francisco, CA 94158, USA

<sup>2</sup>Neuroscience Graduate Program, University of California, San Francisco, San Francisco, CA 94158, USA

<sup>3</sup>Biomedical Sciences Graduate Program, University of California, San Francisco, San Francisco, CA 94158, USA

<sup>4</sup>Medical Scientist Training Program, University of California, San Francisco, San Francisco, CA 94158, USA

<sup>5</sup>Department of Microbiology and Immunology, University of California, San Francisco, San Francisco, CA 94158, USA

<sup>6</sup>UCSF SRTP program, University of California, San Francisco, San Francisco, CA 94158, USA

<sup>7</sup>Institute for Neurodegenerative Diseases/Weill Institute for Neurosciences, University of California, San Francisco, San Francisco, CA 94158, USA

<sup>8</sup>Kavli Institute for Fundamental Neuroscience, University of California, San Francisco, San Francisco, CA 94158, USA

<sup>9</sup>Department of Neurological Surgery, University of California, San Francisco, San Francisco, CA 94158, USA

<sup>10</sup>Eli and Edythe Broad Center for Regeneration Medicine and Stem Cell Research, University of California, San Francisco, San Francisco, CA 94158, USA

<sup>11</sup>Department of Cellular and Molecular Pharmacology, University of California, San Francisco, San Francisco, CA 94158, USA

<sup>12</sup>Bakar Aging Research Institute, University of California, San Francisco, San Francisco, CA 94158, USA

<sup>13</sup>Department of Pediatrics, University of California, San Francisco, San Francisco, CA 94158, USA

<sup>14</sup>Department of Laboratory Medicine, University of California, San Francisco, San Francisco, CA 94158, USA

<sup>15</sup>Department of Neurology, University of California, San Francisco, San Francisco, CA 94158, USA

<sup>16</sup>Department of Anatomy, University of California, San Francisco, San Francisco, CA 94158, USA

<sup>17</sup>Chan-Zuckerberg Biohub, San Francisco, CA 94158, USA

<sup>18</sup>These authors contributed equally

<sup>19</sup>X (formerly Twitter): @AnnaMolofskyLab

<sup>20</sup>Lead contact

\*Correspondence: anna.molofsky@ucsf.edu

<https://doi.org/10.1016/j.cell.2024.02.020>

## SUMMARY

Microglia are brain-resident macrophages that shape neural circuit development and are implicated in neurodevelopmental diseases. Multiple microglial transcriptional states have been defined, but their functional significance is unclear. Here, we identify a type I interferon (IFN-I)-responsive microglial state in the developing somatosensory cortex (postnatal day 5) that is actively engulfing whole neurons. This population expands during cortical remodeling induced by partial whisker deprivation. Global or microglial-specific loss of the IFN-I receptor resulted in microglia with phagolysosomal dysfunction and an accumulation of neurons with nuclear DNA damage. IFN-I gain of function increased neuronal engulfment by microglia in both mouse and zebrafish and restricted the accumulation of DNA-damaged neurons. Finally, IFN-I deficiency resulted in excess cortical excitatory neurons and tactile hypersensitivity. These data define a role for neuron-engulfing microglia during a critical window of brain development and reveal homeostatic functions of a canonical antiviral signaling pathway in the brain.

## INTRODUCTION

Neural circuits undergo experience-dependent changes in connectivity during brain development, and even subtle alterations in this process are associated with neurodevelopmental diseases.<sup>1–4</sup> Microglia are the dominant immune cells in the brain

parenchyma and thus are potential links between the brain and the immune system. Microglia have multiple functions during brain development, including promoting synapse formation and elimination, regulating neuronal activity, and eliminating whole neurons,<sup>5,6</sup> and their dysfunction is associated with diseases of neurodevelopment including autism, epilepsy, and



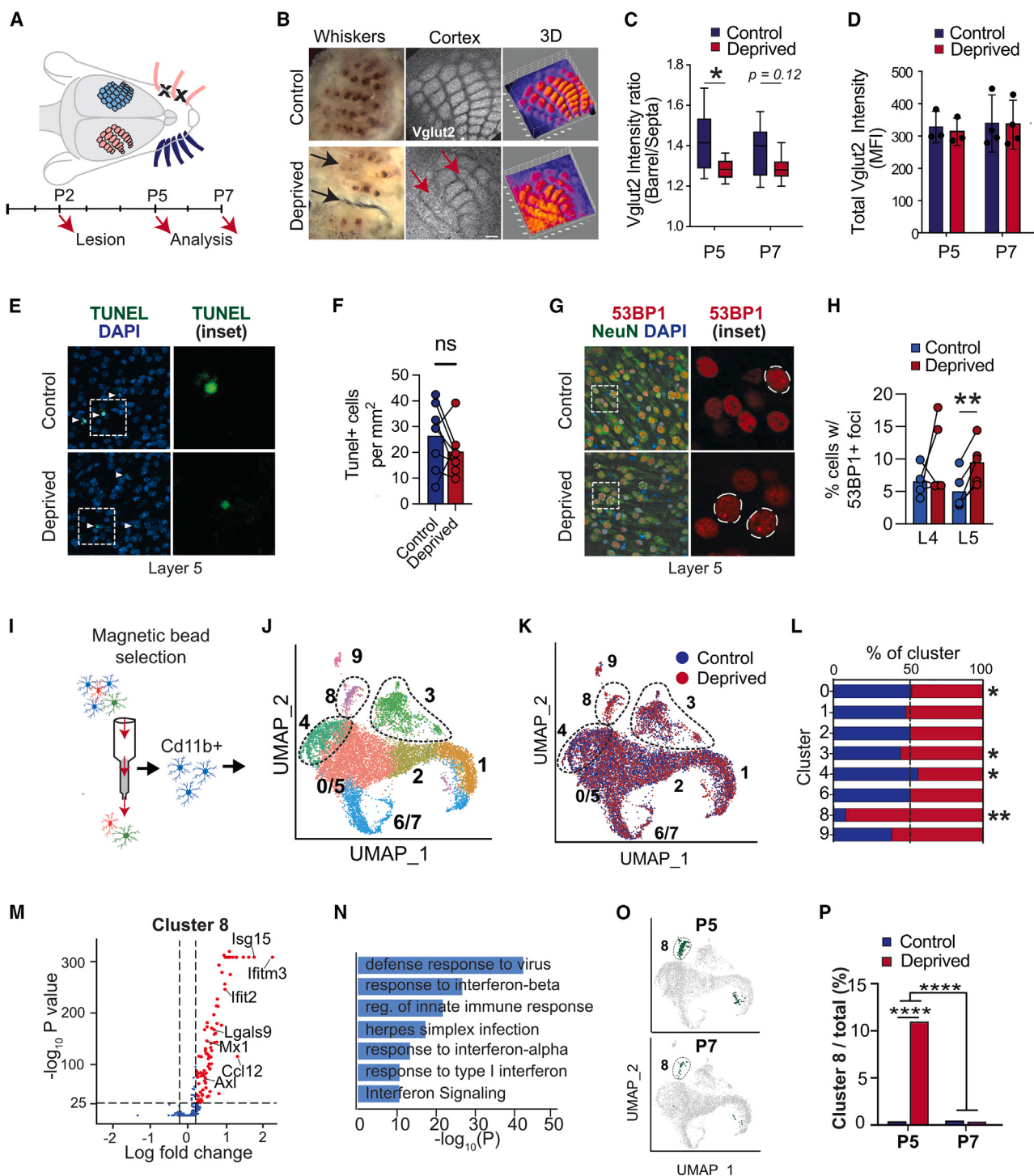


**Figure 1. A type I interferon-responsive microglial subset expands 20-fold during cortical remapping**

(A) Schematic of the partial whisker deprivation model.

(B) Representative images of control and lesioned whisker pad (left, P5), en face imaging of L4 somatosensory cortex, and topographical heatmap of cortex derived from VGLUT2 intensity data (right) (scale bars, 100 μm).

(C) Quantification of barrel distinctness based on VGLUT2 intensity in barrels vs. septa in control and deprived hemispheres. Plot shows range, median, and first and third quartiles (2–4 barrel/septum pairs per condition per mouse; P5 n = 3 mice; P7 n = 4 mice).

(D) VGLUT2 intensity averaged over the entire barrel field in control vs. deprived hemispheres. Error bars show SD (P5 n = 3 mice; P7 n = 4 mice).

(legend continued on next page)

schizophrenia.<sup>7</sup> Single-cell sequencing has revealed distinct microglial states, many of which are conserved in both development and disease. However, in most cases, the functional implications of these molecular signatures are unknown.

One conserved microglial state observed in aging, neurodegeneration, and other pathologies expresses a type I-interferon (IFN-I)-responsive signature.<sup>8</sup> This observation is puzzling because the literature on IFN-I signaling is focused on its roles in antiviral defenses<sup>9</sup> rather than its physiologic function. IFN-I cytokines are evolutionarily conserved, consisting of one IFN- $\beta$  transcript and multiple IFN- $\alpha$ , all of which signal through the canonical JAK/STAT pathway downstream of a receptor that includes the obligate IFNAR1 subunit. Most cells in the body are competent to produce IFN-I and may produce tonic amounts of IFN-I at rest, which are augmented in response to nucleic acids acting as damage-associated molecular patterns (DAMPs).<sup>9</sup> Whether endogenous nucleic acid sensing and IFN-I secretion play a physiologic role in the brain remains to be determined. IFN-responsive microglia are rare in most non-disease settings. However, given that microglial states are highly responsive to the local brain environment,<sup>10–12</sup> low-abundance subsets could reflect transient but functionally critical states.

Here, we identified a population of IFN-I-responsive microglia (IRMs) in the developing murine cortex. These cells were rare in the typically developing brain, comprising less than 0.5% of microglia at P5, but expanded 20-fold in the somatosensory (S1) cortex after a partial whisker lesion at P2 that led to cortical remodeling. *In situ*, we observed that IRMs had a distinct phagocytic morphology and were often in the process of engulfing whole neurons. Eliminating this microglial state via loss of IFN-I sensing led to microglia with distended phagosomes and accumulation of cortical neurons harboring double-strand DNA (dsDNA) breaks, a marker of cell stress or hyperexcitability. Exogenous IFN- $\beta$  was sufficient to drive microglial engulfment of neurons and restrict the number of cortical neurons with dsDNA breaks. Live-imaging studies in zebrafish revealed conservation of this pathway across species and demonstrated an acceleration of whole-neuron-engulfment after IFN-I activation. Furthermore, loss of IFN-I sensing during development led

to an increased density of deep cortical layer excitatory neurons, as well as tactile hypersensitivity in juvenile mice. Taken together, our data reveal a physiological role for IFN-I-driven microglial phagocytosis of whole neurons in brain development and function.

## RESULTS

### A Type I interferon-responsive microglial subset expands 20-fold during cortical remapping

To investigate whether microglia respond to structural rearrangement of neural circuits, we examined the rodent barrel cortex, a canonical model of developmental structural plasticity.<sup>13–17</sup> Lesions of the afferent whisker sensory neurons at postnatal day 2 (P2) lead to topographic remapping of the whisker representations in the contralateral cortex by P5,<sup>13,14,18</sup> during an active period of microglial proliferation and migration.<sup>19</sup> Thalamocortical afferents terminate in layer 4 (L4), which then projects to other cortical layers.<sup>20</sup> Whisker afferents synapse in the brainstem and thalamus en route to the cortex; thus, whisker lesion promotes cortical remodeling without inducing a local injury response. Complete whisker elimination leads to gradual synaptic loss and has been used to discover microglial mechanisms of synapse elimination.<sup>21</sup> Here, we established a subthreshold deprivation model, cauterizing 40% of whisker follicles to promote circuit rearrangement without synaptic loss (Figure 1A).

We first examined the impact of our model on the whisker topographic map. As expected, neonatal whisker removal led to redistribution of the VGLUT2<sup>+</sup> thalamocortical axonal boutons in L4, whereby the deprived cortical rows were smaller with indistinct barrel separation (Figures 1B and 1C).<sup>17</sup> However, mean VGLUT2 intensity across the barrel cortex was not significantly different, suggesting that thalamocortical synapse density was preserved (Figure 1D). We also examined cell death, which has been reported in some variations of this model and in other nodes of the somatosensory circuit.<sup>14</sup> We did not observe changes in the density of TUNEL<sup>+</sup> cells, a marker of end stage DNA damage (Figures 1E and 1F), although phagocytosis of dead cells may be too rapid to be captured by static imaging. However, a marker of

(E) Representative images of TUNEL<sup>+</sup> cells in L5 of the barrel cortex in wild-type (WT) control vs. deprived cortex, P5. White arrowheads: TUNEL<sup>+</sup>DAPI<sup>+</sup> cells. Insets show TUNEL<sup>+</sup> cell (scale bars, 20  $\mu$ m, scale bar inset, 10  $\mu$ m).

(F) TUNEL<sup>+</sup>DAPI<sup>+</sup> cells in barrel cortex of control vs. deprived hemispheres, P5 (n = 8 mice).

(G) Representative images of 53BP1<sup>+</sup> foci in L5 of the barrel cortex, P5. Insets show neurons with 53BP1<sup>+</sup> foci (dotted white line) (scale bars, 20  $\mu$ m, scale bar inset, 10  $\mu$ m).

(H) Neurons with 53BP1<sup>+</sup> foci in the barrel cortex in control vs. deprived hemispheres, P5 (n = 5 mice).

(I) Schematic of microglia isolation for single-cell sequencing.

(J) UMAP clustering of 12,000 CD11b<sup>+</sup> cells, pooling P5 and P7 time points from control and whisker deprived cortices, including microglia (clusters 0–8) and macrophages (cluster 9). Dotted lines highlight clusters for further analysis. Clusters 0/5 and 6/7 were merged due to low numbers of uniquely expressed genes.

(K) Clusters colored by condition (control blue vs. whisker-deprived red).

(L) Quantification of cluster composition by condition. x axis represents percent of cells in each cluster from the control (blue) or deprived (red) hemispheres, normalized for total number of cells per sample (\*pAdj < 0.01, \*\*pAdj < 10<sup>-25</sup>).

(M) Volcano plot of genes differentially expressed in cluster 8 relative to all other clusters.

(N) GO terms upregulated in cluster 8 (Metascape<sup>22</sup>).

(O) UMAP plots separated by age (P5 vs. P7) with cluster 8 highlighted in green.

(P) Cluster 8 abundance at P5 and P7 in control vs. deprived conditions. Data represented as percentage of total cells (\*\*pAdj < 10<sup>-10</sup>).

Data are represented as mean  $\pm$  SEM unless otherwise noted. Dots represent independent animals unless otherwise noted. Lines connect both hemispheres from the same mouse (H).

Statistics: two-way ANOVA with Sidak post hoc test (C and H); paired t test (F); chi-squared test with Bonferroni correction (L and P).

See also Figure S1 and Tables S2A and S2B.

dsDNA breaks (53BP1) revealed a significant increase in neurons with early-stage DNA lesions in whisker-deprived cortices (Figures 1G and 1H). These DNA lesions are observed during cell stress and damage, as well as with neuronal hyperexcitability.<sup>23–25</sup> Similar results were observed with dsDNA break marker γ-H2aX (Figures S1A–S1C). Microglial numbers and IBA1 expression were unaltered (Figures S1D–S1G). Thus, partial whisker deprivation leads to topographic rearrangement of synapses and an increase in neurons with DNA lesions without evidence of overall synaptic loss or cell death.

To molecularly define the microglial response to topographic remapping, we performed single-cell RNA sequencing of microglia at P5 and P7 after whisker removal at P2 (Figure 1).<sup>26,27</sup> We recovered 12,330 cells from 10 mice after filtering, quality control, and *in silico* selection of myeloid cells (Figures 1J and S1H–S1K). We obtained eight clusters after manually combining clusters with few differentially expressed genes. Four of these were altered by whisker deprivation (Figures 1K, 1L, and S1L; Tables S1, S2A, and S2B). Clusters 1, 2, and 6/7 clustered mainly by markers of the different stages of cell division (Figures S1M and S1N). A small border-associated macrophage subset (cluster 9, *Pf4*, and *Lyve1*) was not substantially changed by whisker deprivation. The remaining four clusters (0/5, 3, 4, and 8), all changed in relative abundance after cortical remodeling (Figures 1K and 1L). These included a decrease in two clusters: a homeostatic cluster (*P2ry12*, *Ccr5*, and cluster 0/5) and a cluster resembling “proliferative-region associated microglia” and “damage-associated microglia” (Figures S1O–S1R).<sup>28–30</sup> A cluster containing neuronal genes (cluster 3, *Rbfox3*, and *Grin1*) increased after whisker deprivation (Figure 1K; Table S2A).

Most notable was the emergence of a microglial subpopulation enriched in type I interferon (IFN-I) response genes (IRMs, cluster 8; Figures 1K–1N). This cluster was enriched 20-fold in P5 deprived vs. control cortices but was rare in both settings by P7 (Figures 1O and 1P). IRMs were clearly microglia, with no downregulation of microglial homeostatic genes, including *Tmem119*, *Tgfb1*, and *Hexb* (Figures 1M and S1S). Differential gene expression and Gene Ontology (GO) analysis revealed a robust interferon response signature (*Ifitm3*, *Mx1*, *Ifit3*, *Isg15*, *Irf7*, and *Stat1*) (Figure 1N). IFN-I signaling is a highly evolutionarily conserved antiviral response, but its functions in the developing brain are unknown,<sup>9</sup> raising the question of why these microglia are present during this restricted period of brain development.

### IFN-I responsive microglia are partially conserved across pathologies

To determine if our IRM subset correlated with IFN responses seen in other settings, we examined murine microglial bulk transcriptomic datasets from a variety of physiological and pathological conditions. We analyzed the expression of 39 genes upregulated in cluster 8 and expressed in each of the published datasets (Figure 1M) and highlighted *Ifitm3* and *Mx1*, two of the classically upregulated genes in the pathway (Figure 2A; Table S3A).<sup>31</sup> As expected, the IFN-I signature was most enriched after viral infection (lymphocytic choriomeningitis [LCMV]). However, we also detected prominent induction of an interferon response in sterile pathologies, including mouse models of brain tumors and Alzheimer’s disease (AD), suggest-

ing that IFN-I responses are conserved across multiple pathologic settings. To examine these findings at single-cell resolution, we compared our IFN-I cluster with single-cell datasets from AD models, glioblastoma models, severe acute respiratory syndrome coronavirus 2 (SARS-CoV-2) infection, demyelinating injury (lysophosphatidylcholine [LPC], cuprizone treatment), aging, and transient middle cerebral artery occlusion (tMCAO). These data revealed substantial overlap between our IRM state and the IFN-I responsive subsets in other pathologies, such as SARS-CoV-2 infection or AD models (Figures 2B and S2A; Table S3B).<sup>28,31–38</sup> The IFN-I signature was also enriched relative to controls in these various models, suggesting that IRMs might expand in response to diverse neuronal insults (Figure 2C).

To examine these findings *in situ*, we performed immunostaining of tissue sections for IFITM3, the top upregulated gene in IFN-I responsive cluster 8 (*Ifitm3*, Figure 1M), in two models of pathology. This IFN-α/β-stimulated gene encodes a transmembrane protein that is highly conserved in IFN-I responses.<sup>39–41</sup> Given the high correlation of our IFN-I responsive cluster with SARS-CoV-2 datasets and its neurologic sequelae,<sup>42–44</sup> we quantified IFITM3<sup>+</sup> microglia in a mouse model of neurotropic SARS-CoV-2 infection (K18-ACE2 transgenic mice<sup>45–47</sup>; Figures S2B and S2C). We observed high levels of IFITM3 in most microglia in brains with active viral replication, which correlated strongly with viral burden (Figures S2D–S2H).<sup>48</sup> Microglia expressing IFITM3 clustered around infected cells, formed phagocytic cups around infected neurons, and were more likely to have an amoeboid morphology (Figures S2E, S2G, and S2I). Because IFN-I responses are also implicated in aging and AD,<sup>49–52</sup> we examined the 5xFAD model of Alzheimer’s β-amyloid pathology. In this case, we observed increased number of IFITM3<sup>+</sup> microglia, particularly in the vicinity of amyloid plaques (Figures S2J and S2K), where they formed IFITM3<sup>+</sup> phagocytic cups that contained plaque material (Figures S2L–S2O). Taken together, our data suggest that IRMs are present and expand in multiple contexts, although their phenotype or function could differ across pathologies.

### IFN-I responsive microglia engulf neurons during cortical developmental remodeling

To characterize IRM phenotype and function in the developing brain, we used IFITM3 immunostaining to identify this population *in situ* (Figure 3A). We identified a rare population of IFITM3<sup>+</sup> microglia in deeper cortical layers (L4/5) that were significantly increased in deprived cortex as quantified *in situ* and by flow cytometry (Figures 3B, 3C, and S3A). We confirmed IFITM3 as a bona fide marker of our IRM population using several independent cluster markers. First, we showed that IFITM3<sup>+</sup> cells expressed the canonical IFN-stimulated transcription factor *Mx1*, which was also enriched in cluster 8, using an *Mx1*<sup>GFP</sup> reporter<sup>53</sup> (Figures S3A and S3B). Second, we observed similar results for an alternate cluster 8 marker, BST2 (a.k.a. Tetherin<sup>53,54</sup>), which was also increased after whisker deprivation and was expressed in most IFITM3<sup>+</sup> cells but was less specific than IFITM3 (Figures S3C–S3F). We conclude that IFITM3 is a sensitive and specific marker of IRMs *in situ*.

IRM morphology was distinct from the typical ramified morphology of most cortical microglia. A subtype primarily identified in L4 was elongated and projected toward L5

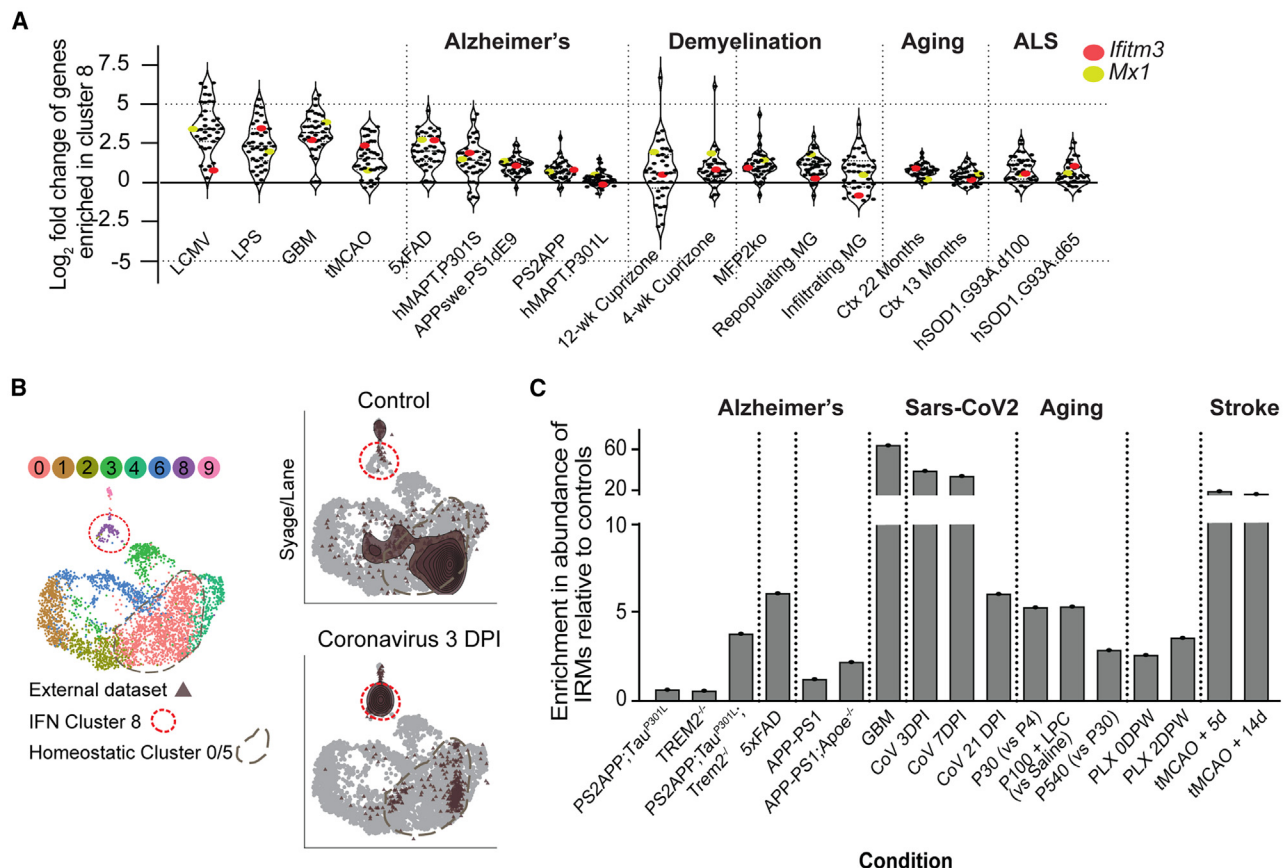


**Figure 2. An interferon-responsive microglia state is partly conserved across pathologies**

(A) Expression of 39 “cluster 8” marker genes (upregulated in cluster 8 by at least 20% at  $p\text{Adj} < 0.005$ , and gene detected in all external datasets) in published microglia sequencing data from bulk sorted CD11b<sup>+</sup> cells.<sup>31</sup> Dots represent individual genes, highlighting *Ifitm3* (red) and *Mx1* (yellow). y axis represents the log fold change relative to its own control. See Table S3A for full details of each sample set and experimental condition.

(B) Our microglial P5/P7 dataset was re-clustered to create a reference principal-component analysis (PCA) and UMAP to which external datasets (brown triangles) were aligned. Red circle: interferon-responsive microglia (cluster 8); gray circle: homeostatic microglia. Representative plots show a SARS-CoV-2 dataset (see Table S3B).

(C) Enrichment of cluster 8-like cells in microglial single-cell sequencing datasets relative to each study’s control. y axis represents fold change in percent cluster 8 overlap between the indicated condition and each dataset’s control. See Table S3B for references<sup>28,32–38</sup>. See also Figure S2 and Tables S3A and S3B.

(“projecting”), with a prominent trailing edge (“uropod”<sup>56</sup>), suggestive of migration toward L5. A second subset was localized to L5 and contained prominent IFITM3<sup>+</sup> phagocytic cups enveloping nuclei (“engulfing,” Figures 3D and 3E). These IRMs had more phagocytic cups than IFITM3<sup>-</sup> microglia (90% vs. 7%; Figures 3F and 3G) and were more likely to have multiple phagosomes per microglia (Figure 3H). They also had increased expression of the lysosomal marker CD68<sup>57</sup> (Figures S3G and S3H). We observed that IRMs contained both early (formation of a phagocytic cup) and late (CD68<sup>+</sup> phagolysosome) stages of phagocytosis in the same cell (Figures S3I and S3J), and that IFITM3 protein was most correlated with early stages of engulfment (Figures S3K and S3L).

Our data also suggested that neurons were the predominant cell type engulfed. First, RNA velocity analysis on our single-cell data<sup>55</sup> predicted a trajectory from IRMs toward microglial cluster 3, which was enriched for neuronal mRNAs (*Rbfox3*,

*Grin1*, and *Gria1*; Figures 3I and 3J; Table S2C). This finding was not due to an outlier effect as microglia in cluster 3 expressed more neuronal mRNAs than observed in 95% of all other cells (Figure S3M). Neuronal genes were mostly unspliced relative to known microglial genes, suggesting that they were derived from the engulfment of neuronal nuclear material (Figures S3N and S3O). Second, in a *Rorb*<sup>cre</sup>/*R26R-TdT* line, which labels most excitatory neurons in L4/5/6,<sup>58</sup> we observed that 9% of L4/5 microglia had TdT<sup>+</sup>CD68<sup>+</sup> phagolysosomes (Figures 3K–3M), whereas we found no TdT inside microglia in an astrocyte reporter line (*Aldh1l1*<sup>TdT</sup>; Figures 3L and 3M). Third, using *in situ* hybridization, we observed that 80% of phagocytic cup-containing microglia surrounded *Grin1* mRNA containing neuronal soma at P5 (Figures S3P and S3Q). Fourth, fate mapping IRMs using an *Mx1*<sup>CRE</sup>/*R26R-TdT* reporter<sup>59</sup> line to capture IFN-I responses revealed the expected increase in *Mx1*<sup>CRE</sup>TdT<sup>+</sup> microglia after whisker deprivation (Figures S3R and S3S) and

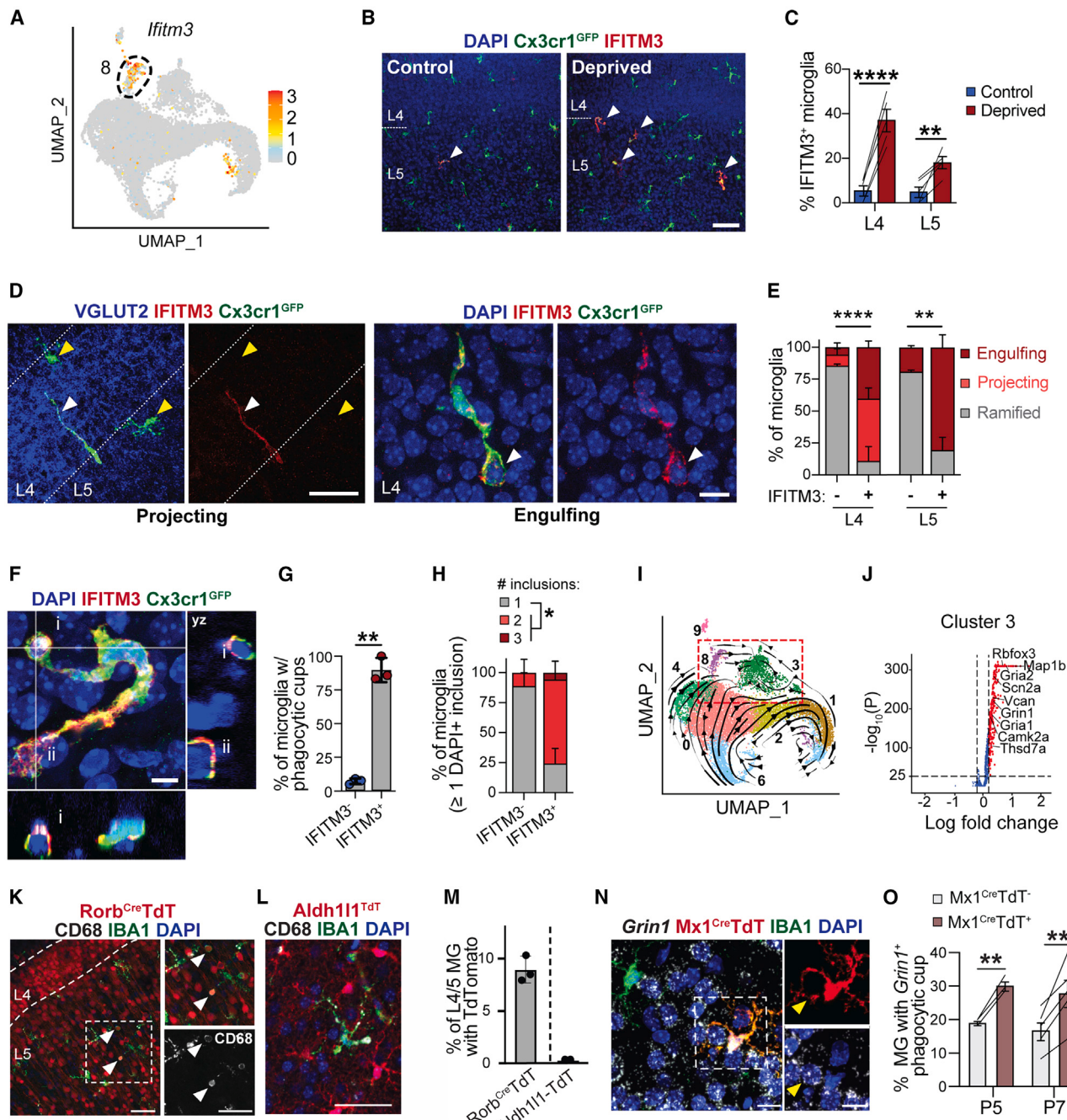


**Figure 3. IFN-I responsive microglia engulf neurons during cortical developmental remodeling**

- (A) UMAP feature plot showing normalized expression of cluster 8 marker gene *Ifitm3*.
- (B) Representative image showing IFITM3<sup>+</sup>*Cx3cr1*<sup>GFP</sup><sup>+</sup> microglia (white arrowheads) in control or deprived hemispheres, P5 (scale bars, 50 μm).
- (C) Percent of IFITM3<sup>+</sup> microglia in L4 vs. L5, P5 ( $n = 5$  mice).
- (D) Representative image of projecting and engulfing IFITM3<sup>+</sup> microglia in deprived barrel cortex, P5 (scale bars, 20 μm [left], 5 μm [right]).
- (E) Quantification of microglial morphological subtypes described in Figure 3D, P5. Data represented as stacked bar graphs  $\pm$  SEM ( $n = 4$  mice).
- (F) Confocal image and orthogonal views of an IFITM3<sup>+</sup> microglia (P5) containing multiple phagocytic cups (i and ii show nuclei-containing phagocytic cups that are distinct from the microglia nucleus) (scale bars, 5 μm).
- (G) Percent of IFITM3<sup>-</sup> and IFITM3<sup>+</sup> microglia with phagocytic cups in P5 barrel cortex ( $n = 3$  mice).
- (H) Distribution of inclusion-containing microglia by number of inclusions, P5. Data represented as stacked bar graphs  $\pm$  SEM ( $n = 3$  mice).
- (I) RNA velocity analysis of data from Figure 1J, showing predicted future cell state colored by cluster (scVelo<sup>55</sup>). Red dotted rectangle highlights transition from IFN-I responsive cluster 8 toward cluster 3 (see Table S2C).

(legend continued on next page)

demonstrated that  $Mx1^{CRE-TdT^+}$  microglia were significantly more likely to contain phagocytic cups around  $Grin1^+$  neurons than  $TdT^-$  cells (Figures 3N and 3O). Together these data suggest that IRMs were primarily engulfing neurons.

### IFN-I promotes microglial phagocytosis and restricts accumulation of DNA-damaged neurons

To determine whether IFN-I signaling was required for microglial phagocytosis and neuronal engulfment, we examined mice lacking the obligate IFN-I receptor *Ifnar1* (Figure 4A). These mice failed to expand IRMs after whisker lesion, consistent with a canonical IFN-I response (Figure 4B). We found that many microglia from *Ifnar1<sup>-/-</sup>* mice had multiple distended phagocytic compartments enclosing diffuse DAPI<sup>+</sup> material (Figures 4C–4F; Video S1). This lysosomal distension phenotype was reminiscent of “bubble” microglia observed in zebrafish with deficits in phago-lysosomal fusion.<sup>60</sup> For subsequent quantifications, we defined “bubble microglia” as those containing phagosomes with a diameter larger than the cell nucleus (Figures 4G and 4H). Bubble microglia were rare in control mice but represented up to 40% of barrel cortex microglia from *Ifnar1<sup>-/-</sup>* mice at P5 (Figure 4I). In both *Ifnar1<sup>-/-</sup>* and littermate controls, bubble microglia were only detected in the early postnatal period (P5–P7) and were no longer detectable by P15 (Figure 4J). These data suggested that IFN-I signaling was required for some aspects of microglial phagocytic function during early cortical development.

To examine how IFN-I signaling impacted microglial phagocytosis, we quantified lysosome acidification using the pH sensitive dye LysoTracker (Figure S4A). LysoTracker intensity did not differ between *Ifnar1<sup>+/+)</sup>* and *Ifnar1<sup>-/-</sup>* mice, suggesting that the bubble phenotype is not a direct consequence of a phagolysosomal acidification defect (Figures S4B and S4F). However, *in vitro* phagocytosis assays using mouse primary microglia (see STAR Methods; Figures S4G and S4I) revealed that poly(I:C) treatment accelerated the digestion of apoptotic cells (Figures S4J and S4K), whereas *Ifnar1* deficiency decreased digestion efficiency (Figures S4L and S4M). These data suggest that IFN-I signaling increases microglial ability to efficiently digest whole-cell cargo, consistent with the observation that IRMs *in vivo* were frequently engulfing and digesting multiple cells at once (Figures 3F–3H and S3J).

We next examined the impact of IFN-I deficiency on cortical neurons. We initially observed that IRM expansion after whisker deprivation correlated with an increase in neurons with dsDNA breaks, suggesting a relationship between these phenotypes

(Figures 1G and 1H). We found a significant increase in the percentage of DNA-damaged neurons in *Ifnar1<sup>-/-</sup>* mice at P5 (Figures 4K and 4L). Similar to the bubble microglia phenotype, this increase in dsDNA breaks was restricted to this early postnatal window and was no longer detectable in either genotype by P15 (Figure 4M). As in the whisker-deprived context, we did not observe a change in the density of TUNEL<sup>+</sup> cells (Figure S4N). Although our studies focused on the barrel cortex, we also found abundant dysmorphic microglia in other regions of the *Ifnar1<sup>-/-</sup>* brain, including the corpus callosum and thalamus, indicating that this pathway may impact microglial function broadly at this stage of development (Figures S4O and S4P). Microglial density was not altered (Figure S4Q). Taken together, these data suggested that IFN-I signaling may promote elimination of neurons that had accumulated DNA damage.

### Microglial-autonomous IFN-I signaling and dsRNA sensing restricts the accumulation of DNA-damaged neurons

To define the cellular mechanisms mediating the IFN-I dependent impacts on neurons and microglia, we first examined which cell types were responding to IFN-I. *In situ* hybridization for *Ifnar1* mRNA revealed receptor expression in most CNS cell types, including microglia, neurons, astrocytes, and endothelial cells (Figures 5A and 5B), consistent with the known broad expression of IFN-I signaling in many tissues.<sup>9,61</sup> We next established two independent approaches to deplete *Ifnar1* from myeloid cells and microglia. We used a *Cx3cr1<sup>CRE</sup>* allele to deplete *Ifnar1* from microglia and other myeloid cells (*Cx3cr1<sup>CRE</sup>:Ifnar1<sup>flox/flox</sup>*). This allele induced CRE protein expression in 90% of microglia, was only detected in myeloid cells, and reduced IFNAR1 protein in microglia by 77% (Figures S5A–S5D). We also used an inducible CRE line (*P2ry12<sup>CreERT2</sup>*, 50 µg tamoxifen at P1, P3, and P4, see STAR Methods), which was microglial specific but reduced microglial IFNAR1 by only 48%, consistent with other studies<sup>63</sup> (Figures S5E–S5H).

We found that loss of *Ifnar1* in microglia/myeloid cells or only in microglia led to a significant increase in bubble microglia, as seen in global IFN-I deficiency (Figures 5C–5F). However, the magnitude of the effect was directly proportional to its deletion efficiency. By contrast, loss of IFN-I sensing by neurons had no effect (Figure S5I; *Syn1<sup>CRE</sup>:Ifnar1<sup>flox/flox</sup>*). We also quantified DNA-damaged neurons after conditional deletion and found that loss of IFN-I sensing by microglia/myeloid cells phenocopied the accumulation of DNA-damaged neurons seen in *Ifnar1<sup>-/-</sup>* animals (Figures 5G and 5H), whereas loss of IFN-I sensing by

(J) Volcano plot of differentially expressed genes in cluster 3.

(K) Representative image of IBA1<sup>+</sup> microglia engulfing Rorb<sup>cre-TdT^+</sup> neurons in L5 barrel cortex, P5. Inset in L5 (right). White arrowheads show Rorb<sup>cre-TdT^+CD68^+</sup> phagolysosomes (scale bars, 50 µm).

(L) Representative image of IBA1<sup>+</sup> microglia and Aldh1l1<sup>TdT^+</sup> astrocytes in the barrel cortex, P5 (scale bars, 50 µm).

(M) Percent microglia containing TdT signal in Rorb<sup>cre-TdT</sup> or Aldh1l1<sup>TdT</sup> transgenic mice in barrel cortex, P5 (n = 3 mice per group).

(N) Representative image of a TdT<sup>+</sup> (*Mx1<sup>CRE</sup>:Rosa26<sup>LSL-TdT</sup>*) IBA1<sup>+</sup> microglial phagocytic cup forming around a  $Grin1^+$  nucleus, P5. Inset (right) with yellow arrowhead showing phagocytic cup around neuronal nucleus (scale bars, 10 µm).

(O) Percent of microglia forming phagocytic cups around  $Grin1^+$  nuclei in the barrel cortex plotted by  $Mx1^{Cre-TdT}$  expression (P5 n = 3 mice; P7 n = 5 mice). Data are represented as mean ± SEM unless otherwise noted. Dots represent independent animals unless otherwise noted. Lines connect both hemispheres from the same mouse (C and O).

Statistics: two-way ANOVA with Sidak post hoc test (C and O); Fisher's exact test (E); Welch's t test (G); chi-squared test (H).

See also Figure S3 and Table S2C.

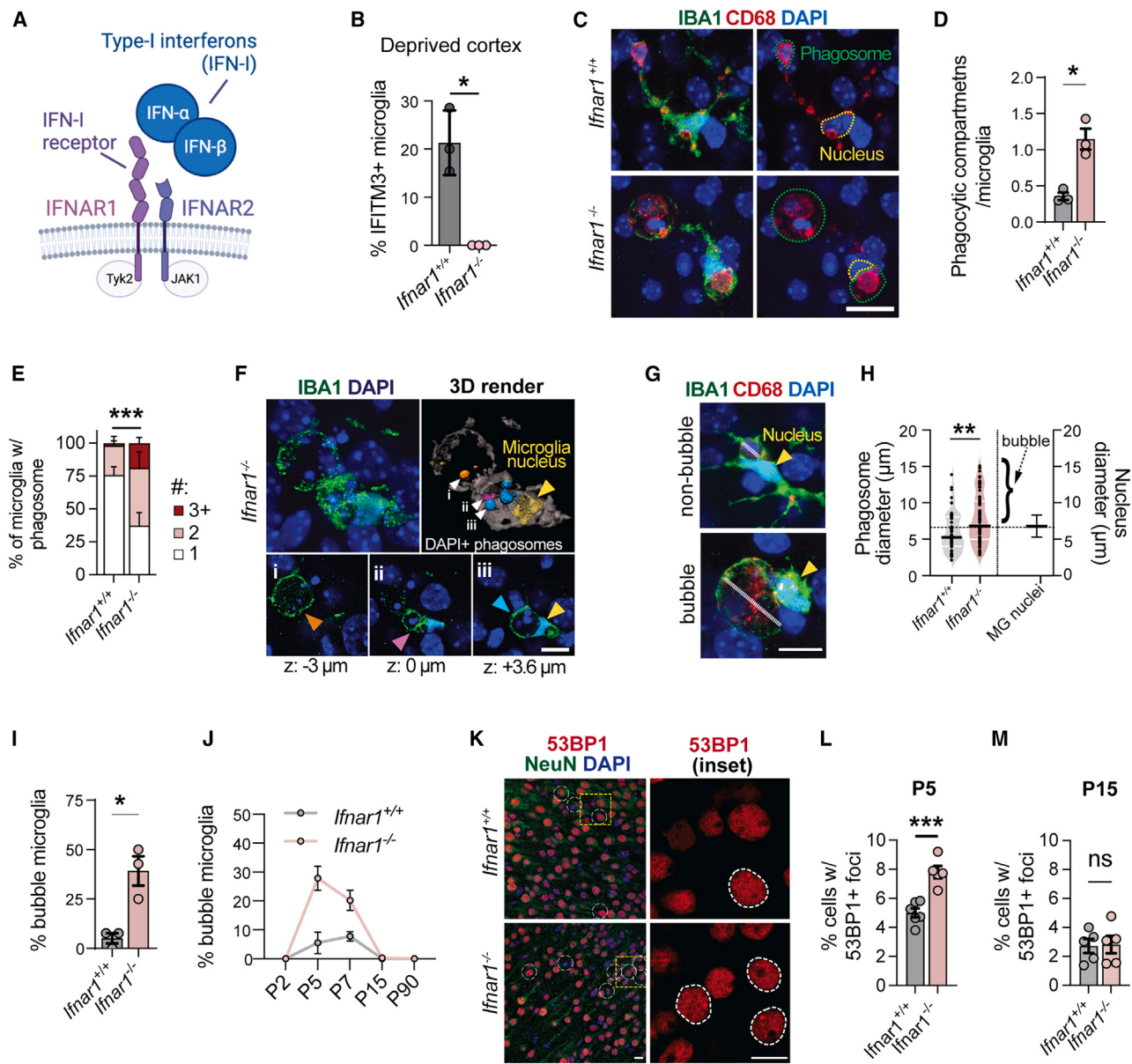


**Figure 4. IFN-I signaling promotes microglial phagocytic function and restricts accumulation of DNA-damaged neurons**

(A) Schematic of type I interferon receptor and ligands.

(B) IFITM3<sup>+</sup> microglia in deprived barrel cortex from *Ifnar1*<sup>+/+</sup> and *Ifnar1*<sup>-/-</sup> mice, P5 (n = 3 mice per group).

(C) Representative images of microglia in barrel cortex from *Ifnar1*<sup>+/+</sup> and *Ifnar1*<sup>-/-</sup> mice, P5. Yellow outline shows microglia nucleus, and green outlines show phagosomes (scale bars, 15  $\mu$ m).

(D) Phagocytic compartments per microglia in barrel cortex of *Ifnar1*<sup>+/+</sup> and *Ifnar1*<sup>-/-</sup> mice, P5 (n = 3 mice per group).

(E) Distribution of phagocytic compartments per microglia in *Ifnar1*<sup>+/+</sup> and *Ifnar1*<sup>-/-</sup> mice, P5. Data represented as stacked bar graph  $\pm$  SEM (n = 3 mice).

(F) Representative image and 3D render of microglia with multiple phagosomes in barrel cortex of *Ifnar1*<sup>-/-</sup> mice, P5. White arrowheads show DAPI<sup>+</sup> phagosomes; yellow arrowheads show microglial nucleus. Insets highlight cross sections through each phagosome, colored as in 3Drender (scale bars, 10  $\mu$ m). See also Video S1.

(G) Representative images of non-bubble microglia with a compact phagosome and a bubble microglia with an enlarged phagosome, P5. Yellow arrowhead shows nucleus, and dashed line shows phagosome diameter in H (scale bars, 10  $\mu$ m).

(H) Left axis: diameter of largest microglial phagosome in barrel cortex from *Ifnar1*<sup>+/+</sup> and *Ifnar1*<sup>-/-</sup> mice, P5. Violin plots show line at mean, and dots show individual microglia. Right axis: mean diameter of microglial nuclei (n = 57–76 microglia from 3 mice per group). Bubble microglia defined as those with phagosomes larger than mean nucleus diameter.

(I) Percent bubble microglia in barrel cortex from *Ifnar1*<sup>+/+</sup> and *Ifnar1*<sup>-/-</sup> mice, P5 (n = 3 mice per group).

(J) Developmental time course of bubble morphology microglia in barrel cortex from *Ifnar1*<sup>+/+</sup> and *Ifnar1*<sup>-/-</sup> mice (P2 n = 2; P5/P7/P90 n = 3; P15 n = 4).

(legend continued on next page)

neurons had no effect (Figure S5J). These data indicate that IFN-I signals cell-autonomously to microglia to promote their phagocytic function and that IFN-I signaling to microglia/myeloid cells restricts the accumulation of DNA-damaged neurons, suggesting that the neuronal impact of IFN-I signaling likely results from alterations in microglial function.

Tonic IFN signaling within tissues occurs in response to low levels of secreted IFNs, which can act both cell-autonomously and non-cell-autonomously.<sup>64</sup> These responses are amplified via sensing of nucleic acid molecular patterns.<sup>9</sup> Double stranded RNA (dsRNA) sensing requires mitochondrial antiviral signaling protein (MAVS), a key adapter protein downstream of cytoplasmic dsRNA sensor RIG-I/MDA5,<sup>9</sup> whereas extracellular dsRNA sensing by microglia requires TLR3.<sup>65</sup> By contrast, cytoplasmic dsDNA sensing requires cGAS and acts via the downstream effector STING<sup>9</sup> (Figure 5I). Similar to *Ifnar1*<sup>-/-</sup> mice (Figure 4B), mice deficient for *Mavs* failed to expand IRMs after whisker deprivation (Figure 5J). The IFN-I response in *Cgas*<sup>-/-</sup> mice was attenuated, whereas *Tlr3*<sup>-/-</sup> had no impact (Figure 5J). *Mavs*<sup>-/-</sup> mice had a significant increase in bubble microglia as seen in IFN-I deficiency, whereas *Cgas*<sup>-/-</sup> and *Tlr3*<sup>-/-</sup> had no effect (Figures 5K and 5L). Furthermore, we observed a significant increase in DNA-damaged neurons in *Mavs*<sup>-/-</sup> mice, but not *Cgas*<sup>-/-</sup> mice (Figures 5M and 5N). These data show that cytoplasmic dsRNA sensing via MAVS phenocopies the neuronal and microglial impact of IFN-I deficiency.

### Exogenous IFN-I promotes neuronal engulfment by microglia in mice and zebrafish

To test whether IFN-I was sufficient to induce neuron-engulfing microglia, we injected IFN- $\beta$  or vehicle intracerebroventricularly (i.c.v.) at P4 and collected tissues at P5 (Figure 6A). We observed robust induction of IFITM3 in 86% of microglia within 300  $\mu$ m of the injection site (Figures 6B and 6C) with no evidence of overt damage or increased cell death (Figure S6A). Conditional deletion of *Ifnar1* from microglia/myeloid cells completely abrogated IFITM3 induction, whereas deletion of *Ifnar1* from neurons had no significant effect (Figures 6D and 6E). IFITM3<sup>+</sup> microglia in IFN- $\beta$ -injected mice had increased numbers of phagocytic cups and phagosomes relative to vehicle controls and included both projecting and soma-associated phagosomes (Figures 6F, 6H, and S6B). These phagosomes were not distended, as observed in bubble microglia (Figure S6C), suggesting that this phenotype reflects accelerated, rather than stalled, phagocytosis. We also found that IFN- $\beta$ -injected mice had a significant reduction in DNA-damaged neurons (Figures 6I and 6J). Using a viral strategy to increase IFN- $\beta$  in neurons, which were the primary cell types expressing *Ifnb1* at baseline (Figures S6D–S6F), we observed similar effects on microglial phagocytic morphology, including the enrich-

ment of IFITM3 around phagocytic cups (Figures 6K–6O, S6G, and S6H). These data suggest that IFN-I is sufficient to drive phagocytic microglia and restrict the accumulation of DNA-damaged neurons.

Phagocytosis is dynamic, and morphology alone is insufficient to determine whether the phagocytic process is accelerated or stalled. To examine the dynamics of IFN-I-dependent phagocytosis, we performed live imaging in larval zebrafish (*Danio rerio*; 7 days post fertilization, Figure 6O). This model system is ideal for imaging the intact, developing brain and contains an evolutionarily conserved antiviral IFN-I system.<sup>66,67</sup> We focused on the zebrafish optic tectum, where a dedicated population of microglia engulf neuronal soma during development.<sup>60,68</sup> We injected poly(I:C) in the ventricles of zebrafish expressing the green myeloid reporter *Tg(mpeg:EGFP-CAAX)* and the red pan-neuronal reporter *Tg(NBT:dsRed)*.<sup>68,69</sup> We found that IFN-I activation significantly increased phagocytic cup formation and led to accelerated envelopment, engulfment, and retraction of neuronal soma (Figures 6P, 6Q, and S6I; Videos S2 and S3). During the imaging window, we observed a 4-fold increase in the percent of neuron-engulfing microglia and of microglia engulfing multiple neurons relative to vehicle-treated controls (Figures 6R and 6S). These phenotypes were similar to what we observed in mice after whisker deprivation or with IFN- $\beta$  overexpression. These data indicate that IFN-I accelerates microglial engulfment of neurons in both murine and zebrafish models.

### IFN-I responsive microglia restrict excitatory neuron numbers and prevent tactile hypersensitivity

We next examined the impact of IFN-I signaling on somatosensory cortical development. Afferent input from the whiskers targets L4 barrels before projecting to other cortical layers, including L5, a key output layer that projects to other sensory regions and modalities (Figure 7A). Because L5 was also the region where most bubble microglia and DNA-damaged neurons were located, we used CTIP2 to highlight L5 excitatory neurons and examine their relationship with microglia (Figure 7B). We did not observe any difference in the density of CTIP2<sup>+</sup> neurons at P5, either in global or microglia-specific *Ifnar1*-deleted animals (Figures 7B, 7C, and S7A). However, we found that most DNA-damaged neurons were also CTIP2<sup>+</sup> (Figures 7D and 7E). We also found that in the whisker-deprived cortex, IRMs were more likely to contact CTIP2<sup>+</sup> neurons (Figures S7B–S7D). These data raised the possibility that loss of IRMs might prevent the elimination of CTIP2<sup>+</sup> DNA-damaged neurons.

We quantified excitatory and inhibitory neuronal subsets in *Ifnar1*<sup>-/-</sup> mice vs. littermate controls at P15, once neuronal numbers are stabilized.<sup>70</sup> We found a significant increase in the density of CTIP2<sup>+</sup> excitatory neurons, which by P15 are no

(K) Representative image of 53BP1 foci-containing neurons in barrel cortex of *Ifnar1*<sup>+/+</sup> and *Ifnar1*<sup>-/-</sup> mice, P5. White circles outline nuclei with 53BP1<sup>+</sup> foci, and yellow square insets highlight 53BP1 staining (left) (scale bars, 10  $\mu$ m).

(L) Percent of all cells containing 53BP1<sup>+</sup> foci in the barrel cortex from *Ifnar1*<sup>+/+</sup> and *Ifnar1*<sup>-/-</sup> mice at P5. Data are represented as mean  $\pm$  SEM. Dot per mouse (n = 6 mice for *Ifnar1*<sup>+/+</sup>, 5 for *Ifnar1*<sup>-/-</sup>).

(M) Percent of all cells containing 53BP1<sup>+</sup> foci in barrel cortex from *Ifnar1*<sup>+/+</sup> and *Ifnar1*<sup>-/-</sup> mice, P15 (n = 5 mice per group).

Data are represented as mean  $\pm$  SEM unless otherwise noted. Dots represent independent animals unless otherwise noted.

Statistics: Welch's t test (B, D, I, L, and M); Fisher's exact test (E); Mann-Whitney test (H).

See also Figure S4.

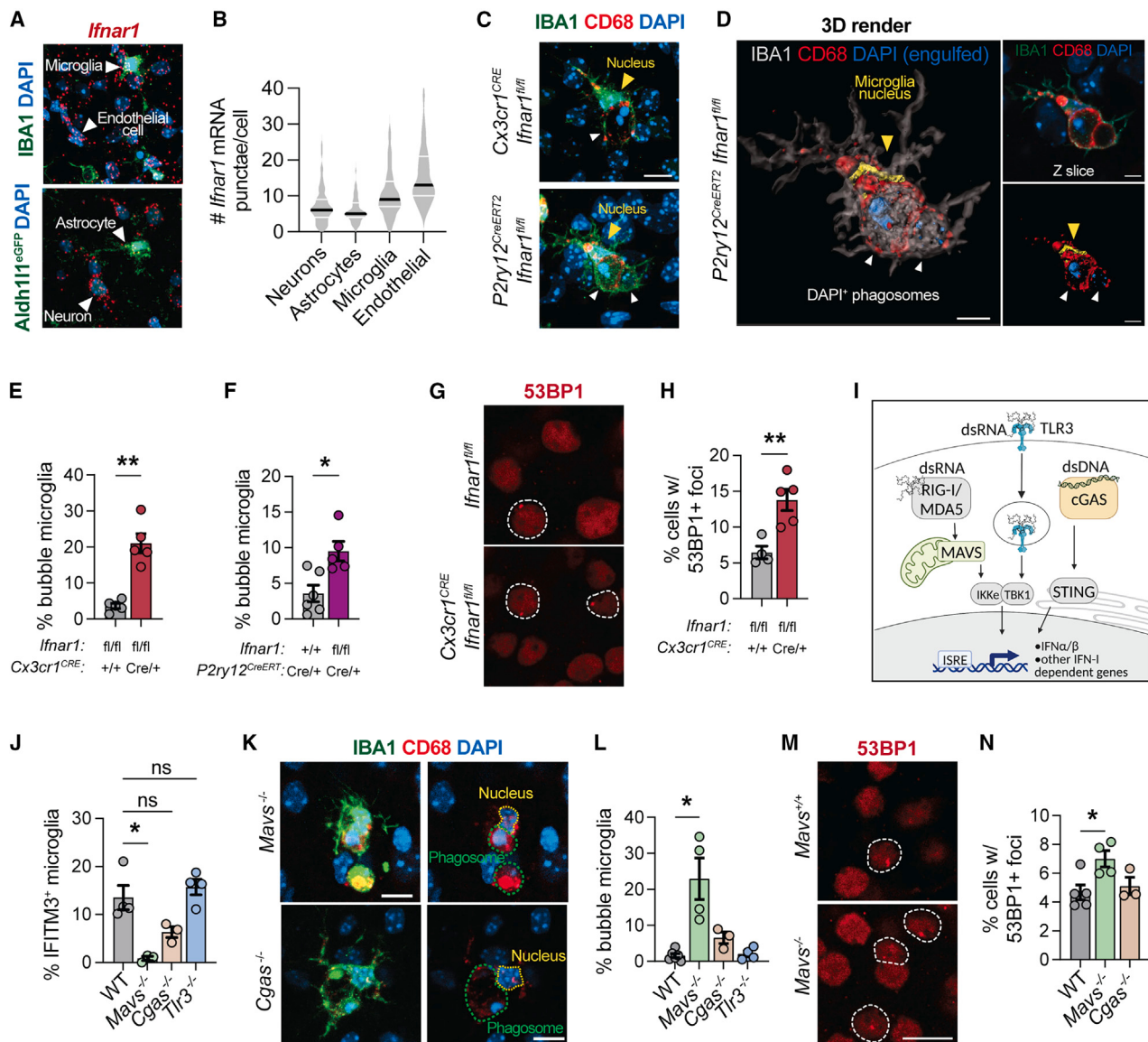


**Figure 5. Microglial-autonomous IFN-I signaling and dsRNA sensing restricts the accumulation of DNA-damaged neurons**

(A) Representative confocal image of *Ifnar1* mRNA transcript co-stained with IBA1 (top) or Aldh1I1<sup>eGFP</sup> reporter (bottom) in P5 somatosensory cortex (scale bars, 50  $\mu$ m).

(B) Quantification of *Ifnar1* mRNA puncta in nuclei of microglia (IBA1 $^{+}$ ), astrocytes (Aldh1I1<sup>eGFP+</sup>), neurons (NeuN $^{+}$ ), and endothelial cells (based on elongated morphology), P5. Data represented as violin plot (mean in black; quartiles in white).

(C) Representative image of IBA1 $^{+}$  microglia in P5 barrel cortex from Cx3cr1<sup>CRE</sup>:*Ifnar1*<sup>flox/flox</sup> mice or P2ry12<sup>CreERT2</sup>:*Ifnar1*<sup>flox/flox</sup> (50  $\mu$ g tamoxifen at P1, P3, and P4) showing enlarged CD68 $^{+}$ DAPI $^{+}$  phagosome. Yellow arrow shows microglia nucleus, and white arrows show phagosome (scale bars, 10  $\mu$ m).

(D) Left: 3D render of IBA1 $^{+}$  microglia in (C) (P2ry12<sup>CreERT2</sup>:*Ifnar1*<sup>flox/flox</sup>) showing enlarged DAPI $^{+}$  CD68 $^{+}$  phagosome. Top right shows a single Z slice. Bottom right shows the 3D render without IBA1 volume (scale bars, 5  $\mu$ m).

(E) Percent bubble microglia in barrel cortex from *Ifnar1*<sup>flox/flox</sup> vs. Cx3cr1<sup>CRE</sup>:*Ifnar1*<sup>flox/flox</sup> mice, P5 (n = 5 mice per group).

(F) Percent bubble microglia in barrel cortex from *Ifnar1*<sup>flox/flox</sup> vs. P2ry12<sup>CreERT2</sup>:*Ifnar1*<sup>flox/flox</sup> mice, P5 (50  $\mu$ g tamoxifen at P1, P3, and P4) (n = 6 mice for *Ifnar1*<sup>flox/flox</sup> and 5 for P2ry12<sup>CreERT2</sup>:*Ifnar1*<sup>flox/flox</sup>).

(G) 53BP1 foci+ neurons in barrel cortex from *Ifnar1*<sup>flox/flox</sup> vs. Cx3cr1<sup>CRE</sup>:*Ifnar1*<sup>flox/flox</sup> mice, P5. White circles outline nuclei with 53BP1+ foci (scale bars, 10  $\mu$ m).

(H) Percent of all cells containing 53BP1+ foci in barrel cortex from *Ifnar1*<sup>flox/flox</sup> vs. Cx3cr1<sup>CRE</sup>:*Ifnar1*<sup>flox/flox</sup> mice, P5 (n = 4 mice for *Ifnar1*<sup>flox/flox</sup> and 5 for Cx3cr1<sup>CRE</sup>:*Ifnar1*<sup>flox/flox</sup>).

(I) Schematic of nucleic acid sensing pathways inducing IFN-I responses.

(J) Percent IFITM3 $^{+}$  microglia in deprived barrel cortex from WT, Mavs<sup>-/-</sup>, Cgas<sup>-/-</sup>, and Tlr3<sup>-/-</sup> mice, P5 (n = 4 mice for WT and Tlr3<sup>-/-</sup> and n = 3 for Mavs<sup>-/-</sup> and Cgas<sup>-/-</sup>).

(K) Representative image of IBA1 $^{+}$  microglia in barrel cortex of Mavs<sup>-/-</sup> and Cgas<sup>-/-</sup> mice showing DAPI $^{+}$  phagosome, P5. Yellow outline shows microglia nucleus, and green outline shows phagocytic compartments (scale bars, 10  $\mu$ m).

(legend continued on next page)

longer restricted to L5 but distributed throughout L5/6 (Figures 7F and 7G), without alterations in overall number of cells (DAPI<sup>+</sup>), total neurons (NeuN<sup>+</sup>), or total excitatory neurons (SATB2<sup>+</sup>) in *Ifnar1*<sup>-/-</sup> mice (Figures S7E–S7I). Conversely, we found a significant decrease in the density of Parvalbumin<sup>+</sup> inhibitory neurons, which are enriched in L4/5 (Figures 7H and 7I), and a trend toward fewer Somatostatin<sup>+</sup> and GAD67<sup>+</sup> interneurons (Figures S7J–S7M). Thus, IFN-I deficiency leads to an increased ratio of excitatory vs. inhibitory neurons in deeper cortical layers. These findings are consistent with a model whereby IFN-I signaling promotes elimination of some deep layer cortical excitatory neurons, although a more general impact on cortical maturation<sup>71</sup> cannot be ruled out.

We next examined the impact of IFN-I signaling on somatosensory function using a whisker nuisance assay to quantify behavioral responses to tactile stimulation (Figure 7J)<sup>72–74</sup> at P15, the age at which we observed alterations in neuronal composition. Following habituation to context and probe, mice underwent three brief episodes of unilateral whisker stimulation, and tactile sensitivity was tabulated via blinded visual scoring of behavioral responses.<sup>73</sup> Both global and microglial-specific deletion of *Ifnar1*<sup>-/-</sup> led to a significant increase in tactile sensitivity as reflected by aggression and increased avoidance of the probe (Figures 7K, 7L, S7N, and S7O). By contrast, neuronal-specific deletion of *Ifnar1* had no impact on tactile sensitivity responses (Figures 7M and S7P). These data directly demonstrate a role for microglial IFN-I responses in restricting tactile hypersensitivity.

## DISCUSSION

IFN-I responses are central to antiviral defense, but their role in physiology is comparatively unknown.<sup>75–77</sup> Here, we define a IFN-I responsive microglial state and reveal an unexpected role for IFN-I signaling in driving microglial engulfment of neurons and shaping circuit connectivity during a temporally restricted window of brain development (Figure 7). The major implications of this finding are discussed below.

### A transient IFN-I-responsive signaling state emerges during neuronal phagocytosis

Our data indicate that the IRM state promotes a unique mode of phagocytosis: surrounding and engulfing whole neurons. Although the engulfment of whole cells is an established function of microglia in brain regions with neuronal turnover,<sup>78</sup> these data reveal a key role for this process in cortical development. Our data suggest that the IRM state is transient and context dependent: although they are rare during typical development, they expand in response to stress, and despite their rarity, preventing the IRM state by microglia-specific deletion of *Ifnar1* resulted in a large fraction of microglia with phagocytic dysfunction (20%–

30%). These findings suggest that IRMs represent a transient but critical cell state adopted during phagocytosis.

What triggers a subset of microglia to become IFN-I responsive? Damage-associated molecular patterns, including dsRNA and dsDNA,<sup>79–82</sup> both initiate and amplify IFN-I responses by increasing production of IFN-I. Our data in *Mavs*<sup>-/-</sup> animals indicate that dsRNA sensing is required for the emergence of IRMs after whisker deprivation, with MAVS deficiency phenocopying key features of IFN-I deficiency. This is consistent with studies showing that neurons contain unusually high levels of dsRNA compared with other cell types.<sup>83</sup> Sensing of dsRNA from engulfed neurons could occur within the microglial cytoplasm<sup>84</sup> to enable more efficient engulfment and digestion of subsequent neurons. Alternately, neurons could selectively produce IFN-I in a *Mavs*-dependent manner based on their dsRNA content<sup>83</sup> driving the local emergence of IRMs. Cell-type-specific deletion of dsRNA sensing will be required to definitively answer this question.

### Microglial IFN-I responses promote neuronal development and cortical function

Cortical L5 plays a critical role in somatosensory function by integrating information from contralateral S1 and other sensory modalities.<sup>85</sup> Our data suggested that most IFN-I-dependent phenotypes occurred in L5, including DNA-damaged neurons and bubble microglia. Both these phenotypes peaked at P5 and decreased in frequency by P15 and were conserved across both loss- and gain-of-function models. These data argue that microglial IFN-I responses in microglia enable a phagocytic response that limits the accumulation of DNA-damaged neurons in L5 and is later critical for somatosensory function. Given the widespread microglial dysmorphia in brains of *Ifnar1*-deficient mice, this pathway could be relevant to the maturation of other brain regions beyond the somatosensory cortex.

One potential implication of our model is that IRMs could promote elimination of neurons that are damaged but not yet irreversibly so. We did not observe a relationship between IFN-I-signaling and cell death, and IRMs often formed phagocytic cups around non-pyknotic nuclei (e.g., Figures 3D, 3F, 3M, and S3P). These data suggest that IFN-I-dependent neuronal engulfment may be distinct from microglial elimination of apoptotic cells (efferocytosis) as seen in the murine hippocampus and the zebrafish optic tectum.<sup>86,87</sup> Further characterization of this neuronal state will be critical. The accumulation of DNA-damaged neurons in *Mavs*<sup>-/-</sup> animals suggests that the dsDNA breaks are a correlate and not the direct cause of microglial IFN-I responses. Because dsDNA breaks in neurons can be a sign of early neuronal stress but can also be observed with neuronal hyperexcitability,<sup>23–25</sup> further studies of the relationship between neuronal stress, activity, and IFN-I responses will help clarify this relationship.

(L) Percent bubble microglia in barrel cortex from WT, *Mavs*<sup>-/-</sup>, *Cgas*<sup>-/-</sup>, and *Tlr3*<sup>-/-</sup> mice, P5 (n = 3 mice for *Cgas*<sup>-/-</sup>, 4 *Mavs*<sup>-/-</sup> and *Tlr3*<sup>-/-</sup>, and 6 WT).

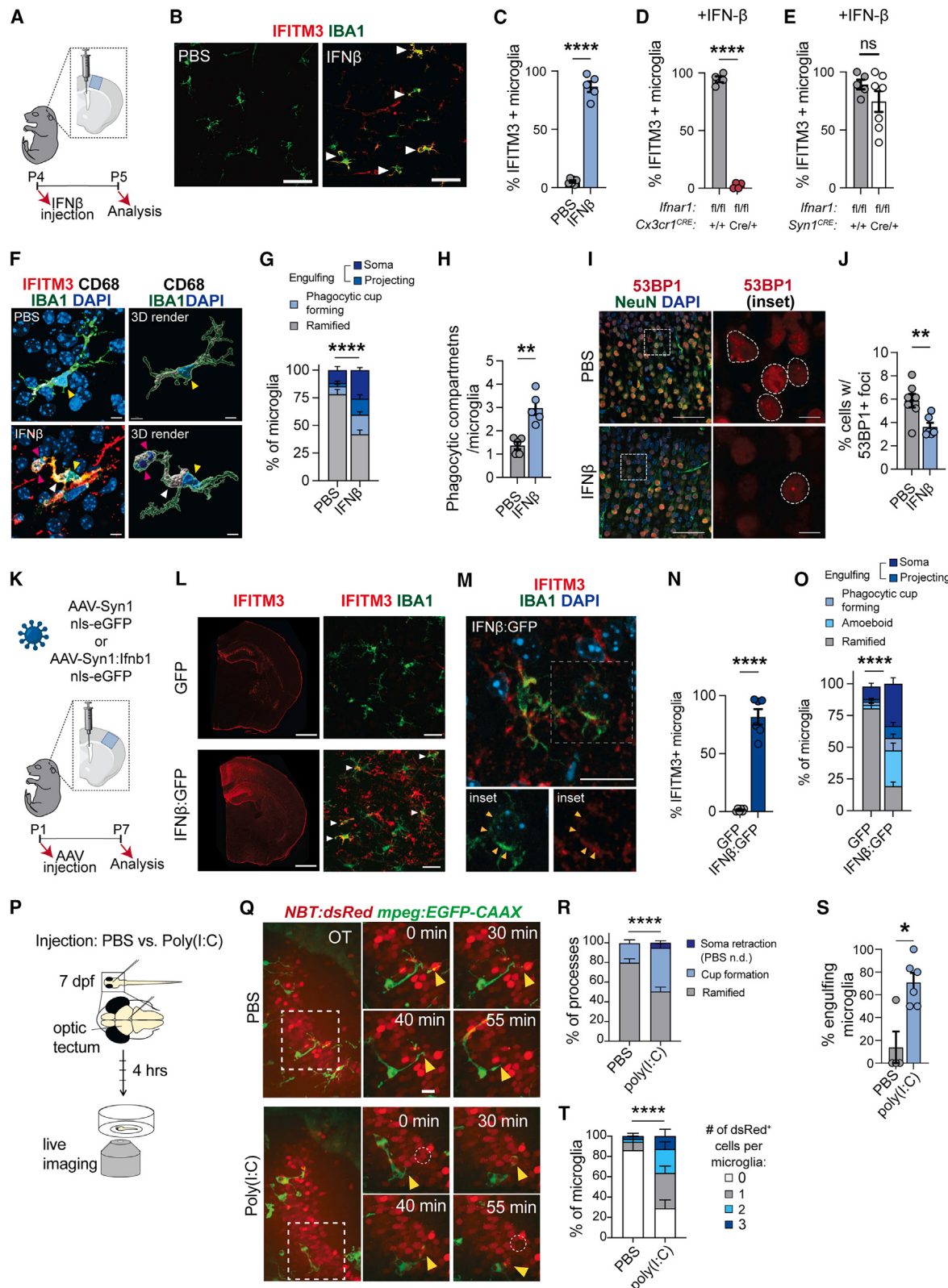
(M) 53BP1 foci+ neurons in the barrel cortex from *Mavs*<sup>+/-</sup> vs. *Mavs*<sup>-/-</sup> mice, P5. White dotted lines outline nuclei with 53BP1<sup>+</sup> foci (scale bars, 10 μm).

(N) Percent of cells with foci in barrel cortex from WT, *Mavs*<sup>-/-</sup>, and *Cgas*<sup>-/-</sup> mice, P5 (n = 3 mice for *Cgas*<sup>-/-</sup>, 4 *Mavs*<sup>-/-</sup>, and 5 WT).

Data are represented as mean ± SEM unless otherwise noted. Dots represent independent animals unless otherwise noted.

Statistics: Welch's t test (E, F, and H); Kruskal-Wallis with Dunn's multiple comparisons (J and L); one-way ANOVA with Dunnett's multiple comparisons (N).

See also Figure S5 and Video S1.



(legend on next page)

## Interferon responsive microglia in development and disease

Our model also suggests a mechanism by which homeostatic IFN-I responses could become pathologic. External triggers that increase IFN-I tone, such as viral infection, could drive IFN-I secretion from microglia<sup>88,89</sup> or from neurons,<sup>90</sup> thus recruiting a widespread microglial response that could drive indiscriminate neuronal cell death and neuroinflammation. However, the function and ontogeny of IRMs could vary across model systems. They promote synapse removal during neurodegeneration<sup>50,51</sup> where they may emerge in response to cGAS/STING signaling rather than RIG-I/MAVS.<sup>52</sup> Defining to what extent the neuron-engulfing role of IRMs is conserved across pathologic contexts will be critical.

Balanced IFN-I signaling is required for normal brain development and function.<sup>89</sup> Elevated IFN-I signaling can cause diverse type I interferonopathies with neurocognitive impacts, including Aicardi-Goutières syndrome (AGS), USP18 deficiency, and systemic lupus erythematosus (SLE).<sup>91</sup> Down syndrome, which is associated with intellectual disability and early-onset AD, includes triplication of multiple IFN-I receptors, resulting in elevated IFN-I signaling in both humans and in mouse models.<sup>92–95</sup> Neurodevelopmental disorders, such as schizophrenia and autism spectrum disorders (ASDs), are epidemiologically linked to maternal immune activation,<sup>96</sup> suggesting a link between antiviral immune responses and cortical develop-

ment. As in our study, deficits in sensory processing are common in ASD<sup>97,98</sup> and in animal models of ASD-like behaviors.<sup>99</sup> Further defining of the role of IRMs in these contexts could reveal further mechanistic links between developmental immune activation and neuropsychiatric diseases.

## Limitations of the study

This study identifies a transient neuron-engulfing microglial state and shows a requirement for microglial IFN-I responses in cortical development and behavior. However, we cannot directly observe which neurons are targeted for elimination and whether they are eaten “dead or alive.” Although we did not observe changes in cell death in our gain- or loss-of-function settings, cell death happens extremely quickly and can be difficult to capture, and there are modes of cell death that are still being discovered. In addition, further experiments will be required to define the mechanism by which cytoplasmic nucleic acid sensing pathways lead to neuronal elimination. Thus, mechanistic and temporal questions remain regarding how IRMs selectively shape cortical development.

## STAR METHODS

Detailed methods are provided in the online version of this paper and include the following:

### Figure 6. IFN-I is sufficient to promote neuronal engulfment by microglia

- (A) Experimental design: 10 ng of IFN-β or vehicle (PBS) injected i.c.v. at P4, tissue collection at P5. Blue square shows region of motor cortex analyzed (within 300 μm of injection site).
- (B) Representative images of IFITM3<sup>+</sup> microglia (white arrowheads) in PBS- vs. IFN-β-injected mice, P5 (scale bars, 50 μm).
- (C) Percent IFITM3<sup>+</sup> microglia in cortex of PBS- vs. IFN-β-injected mice, P5 (n = 6 mice for PBS, 5 for IFN-β).
- (D) Percent IFITM3<sup>+</sup> microglia in cortex of *Ifnar1*<sup>fl/fl</sup> vs. *Cx3cr1*<sup>CRE</sup>:*Ifnar1*<sup>fl/fl</sup> mice injected with IFN-β, P5 (n = 4 mice per group).
- (E) Percent IFITM3<sup>+</sup> microglia in cortex of *Ifnar1*<sup>fl/fl</sup> vs. *Syn1*<sup>CRE</sup>:*Ifnar1*<sup>fl/fl</sup> mice injected with IFN-β, P5 (n = 5 mice for *Ifnar1*<sup>fl/fl</sup> and 7 for *Syn1*<sup>CRE</sup>:*Ifnar1*<sup>fl/fl</sup>).
- (F) Representative images and 3D render of microglia in PBS- vs. IFN-β-injected mice, P5. Pink arrowheads show “projecting phagosomes,” white arrowhead shows CD68<sup>+</sup> “soma phagosome,” and yellow arrowhead shows nucleus (scale bars, 5 μm).
- (G) Quantification of microglial morphology subtypes (“soma-associated” and projecting phagosomes as in F, “phagocytic cup forming,” or “ramified/homeostatic”) from PBS- vs. IFN-β-injected mice. Data represented as stacked bar graphs ± SEM (n = 6 mice for PBS, 5 for IFN-β).
- (H) Phagocytic compartments per microglia (IFITM3<sup>-</sup> vs. IFITM3<sup>+</sup>) in PBS- vs. IFN-β-injected mice (n = 5 mice per group).
- (I) Representative images of neurons with 53BP1<sup>+</sup> foci in PBS- vs. IFN-β-injected mice. White circles in inset outline nuclei with 53BP1<sup>+</sup> foci (scale bars, 50 μm and inset scale bars, 10 μm).
- (J) Percent of all cells containing 53BP1<sup>+</sup> foci in PBS- vs. IFN-β-injected mice (n = 7 mice for PBS, 6 for IFN-β).
- (K) Schematic of viral overexpression strategy (nls-eGFP, nuclear-localized green fluorescent protein).
- (L) Representative low-power image of IFITM3 induction following viral infection, P7. White square shows inset, and white arrowheads show IFITM3<sup>+</sup> microglia (scale bars, 1 mm, and inset scale bars, 30 μm).
- (M) Representative image of a phagocytic microglia in an AAV-Syn1:*Ifnb1*-nls-eGFP-injected brain, P7. White square shows inset, and yellow arrowheads show IFITM3<sup>+</sup> phagocytic cup around a nucleus (scale bars, 5 μm).
- (N) Percent IFITM3<sup>+</sup> microglia in barrel cortex of virally infected mice, P7 (n = 6 per group).
- (O) Quantification of microglial morphology subtypes (as in F and G) from virally infected mice, P7. Data represented as stacked bar graph ± SEM (n = 6 mice per group).
- (P) Schematic of zebrafish poly(I:C) injection and live-imaging experiment. See STAR Methods for details.
- (Q) Time series of microglia (green, Tg(mpeg:EGFP-CAAX)) and neurons (red; Tg(NBT:dsRed)) in the zebrafish optic tectum. Yellow arrowhead, top: a neuron contacted by a microglial process but not engulfed. Yellow arrowhead, bottom: a neuron engulfed and retracted toward the microglial soma. White circle shows original position of the engulfed neuron (scale bars, 10 μm). See also Videos S2 and S3.
- (R) Distribution of process morphologies as indicated (see also Figure S6l). Data represented as stacked bar graphs ± SEM (n = 4 zebrafish for PBS, 6 for poly(I:C)). Morphologies defined further in Figure S6l.
- (S) Percent of microglia engulfing at least one dsRed<sup>+</sup> neuron during 1 h (n = 4 zebrafish for PBS, 6 for poly(I:C)).
- (T) Percent of microglia engulfing 0, 1, 2, or 3 dsRed<sup>+</sup> neurons during image acquisition. Data are represented as stacked bar graphs ± SEM (n = 4 zebrafish for PBS, 6 for poly(I:C)).

Data are represented as mean ± SEM unless otherwise noted. Dots represent independent animals unless otherwise noted.

Statistics: Welch’s t test (C, D, E, H, J, N, and S); Fisher’s exact test (G, O, R, and T).

See also Figure S6 and Videos S2 and S3.

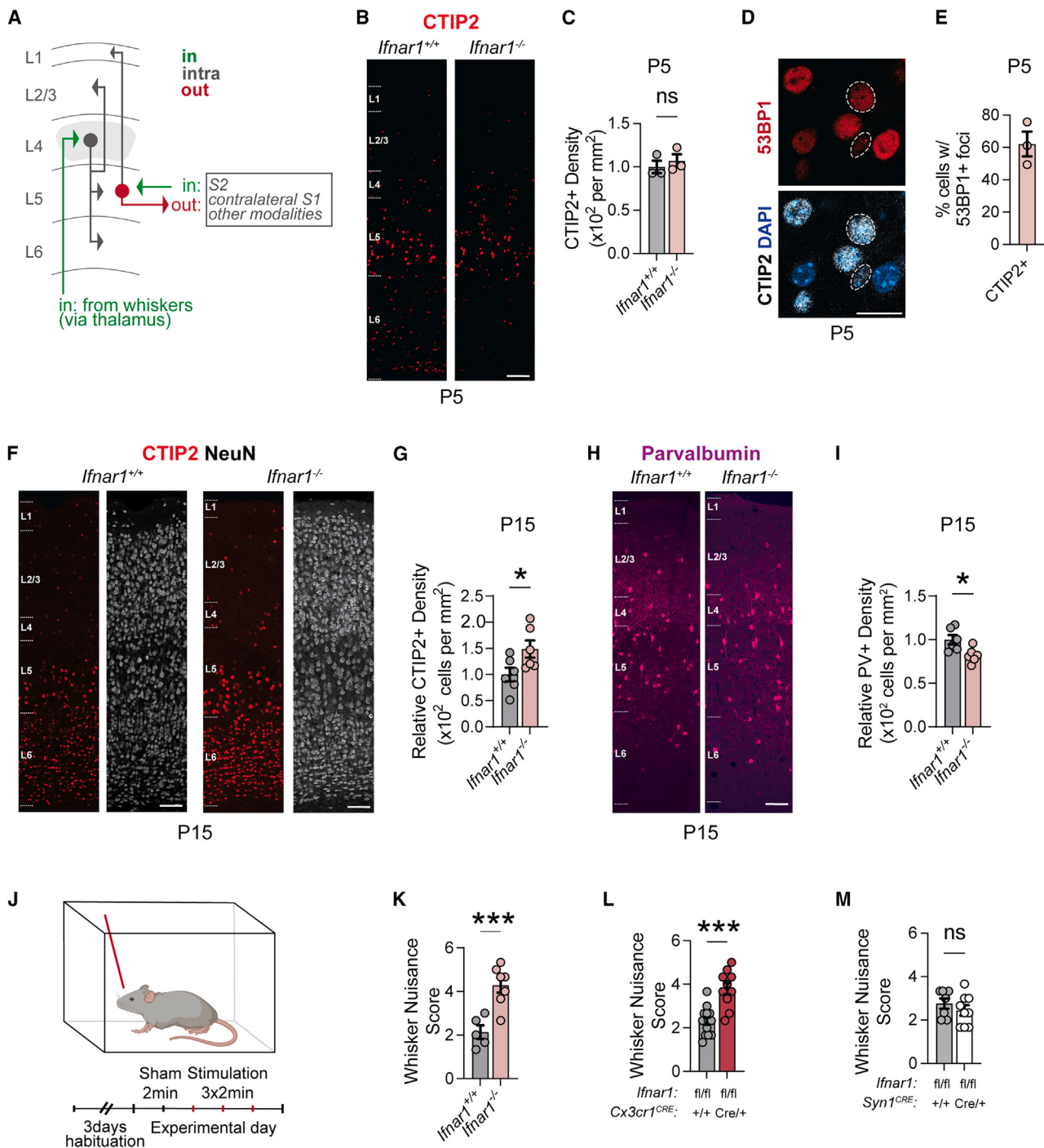


**Figure 7. IFN-I responsive microglia prevent tactile hypersensitivity**

- (A) Schematic of barrel cortex circuits.
- (B) Representative images of CTIP2 in somatosensory cortex of P5 *Ifnar1<sup>+/+</sup>* and *Ifnar1<sup>-/-</sup>* mice. White lines on the left highlight cortical layers (scale bars, 100 μm).
- (C) Relative CTIP2+ neuron density per mm $^2$  in L5 in *Ifnar1<sup>+/+</sup>* and *Ifnar1<sup>-/-</sup>* mice, P5 (n = 3 mice per group).
- (D) Representative image showing co-localization of 53BP1 foci with CTIP2 in barrel cortex L5 from *Ifnar1<sup>-/-</sup>* mice, P5. White circles outline the CTIP2+ 53BP1 foci+ neurons (scale bars, 10 μm).
- (E) Percent of 53BP1 foci+ neurons co-localizing with CTIP2 in barrel cortex L5 from *Ifnar1<sup>-/-</sup>* mice, P5 (n = 3 mice).
- (F) Representative images of CTIP2+ neurons in somatosensory cortex of P15 *Ifnar1<sup>+/+</sup>* and *Ifnar1<sup>-/-</sup>* mice. White lines on the left highlight cortical layers (scale bars, 100 μm).
- (G) Relative CTIP2+ neuron density in all cortical layers of the somatosensory cortex in P15 *Ifnar1<sup>+/+</sup>* and *Ifnar1<sup>-/-</sup>* mice (n = 6 mice per group).

(legend continued on next page)

- **KEY RESOURCES TABLE**
- **RESOURCE AVAILABILITY**
  - Lead contact
  - Materials availability
  - Data and code availability
- **EXPERIMENTAL MODEL AND STUDY PARTICIPANT DETAILS**
  - Mice
  - Zebrafish
- **METHOD DETAILS**
  - Tamoxifen injections
  - Whisker lesions
  - Immunohistochemistry and confocal microscopy
  - Microglia CD68 volume
  - Microglia phagocytic compartment analyses
  - Neuronal subtype counts
  - Tunel staining
  - Fluorescent *in situ* hybridization
  - Flow cytometry
  - Measurement of lysosomal pH using Lysotracker
  - SARS-CoV-2 virus propagation and plaque assay
  - SARS-CoV-2 infection
  - Tissue processing for MERFISH
  - MERFISH data processing and analysis
  - Interferon β injection
  - Viral gain of function
  - Poly(I:C) microinjection into zebrafish larvae
  - Zebrafish live imaging
  - Quantitative PCR
  - Generation of apoptotic cells
  - Primary microglia culture and engulfment assay
  - Behavioral assay—Whisker nuisance test
  - Single-cell sequencing preparation
  - Microglial single-cell sequencing and analysis
- **QUANTIFICATION AND STATISTICAL ANALYSIS**
  - Statistical analysis

#### SUPPLEMENTAL INFORMATION

Supplemental information can be found online at <https://doi.org/10.1016/j.cell.2024.02.020>.

#### ACKNOWLEDGMENTS

We are grateful to Molofsky Lab members for helpful comments, Dr. Rafael Han for assistance with tissue preparation, John Boscardin for statistical support, Karl Garcia for technical support with MERFISH, Dr. William Weiss and Dr. Ekin Guney for access to the Incucyte and SH-S5Y5 cell line, and to the Chan Zuckerberg Biohub for sequencing. We acknowledge the following funding support: to A.V.M.: Pew Charitable Trusts, NIMH (R01MH119349 and

DP2MH116507), and the Burroughs Wellcome Fund; to T.J.N.: NIMH RF1MH121268; to L.C.D.: Matilda Edlund Scholarship and the Genentech Fellowship; to P.T.N.: the National Science Foundation Grant #1650113; to C.C.E.: gift from Marilyn Waldman and T32 training grant (5T32AI007334); to S.R.A.: Weill Neurohub Fellowship; to C.C.: NIA RF1AG061874; and to B.S.: NIH R01AG064363 and the UCSF Program for Breakthrough Biomedical Research (partially funded by the Sandler Foundation). This study was supported in part by the HDFCCC Laboratory for Cell Analysis Shared Resource Facility through a grant from the NIH (P30CA082103). Schematics were created with [Biorender.com](#).

#### AUTHOR CONTRIBUTIONS

Conceptualization, A.V.M., L.C.D., C.C.E., and P.T.N.; methodology, L.C.D., A.V.M., P.T.N., I.D.V., C.C.E., H.N.-I., Y.X., R.A. B.S., H.N., N.J.S., T.J.N., C.C., and T.D.A.; investigation: L.C.D., P.T.N., I.D.V., S.E.T., C.C.E., E.Y.W., Y.X., P.V.L., C.L.-L., B.C., H.N., N.J.S., S.R.A., J.J.B., S.D.W., R.G., D.K.K., and E.K.; writing – original draft, L.C.D., P.T.N., C.C.E., and A.V.M.; writing – review & editing, all co-authors; funding acquisition, A.V.M.; resources, A.V.M., R.A., C.C., and T.D.A.; supervision, A.V.M., T.J.N., R.A., B.S., and I.D.V.

#### DECLARATION OF INTERESTS

The authors declare no competing interests.

Received: July 14, 2023

Revised: December 31, 2023

Accepted: February 19, 2024

Published: March 14, 2024

#### REFERENCES

1. Forrest, M.P., Parnell, E., and Penzes, P. (2018). Dendritic structural plasticity and neuropsychiatric disease. *Nat. Rev. Neurosci.* 19, 215–234.
2. Bitzenhofer, S.H., Pöplau, J.A., Chini, M., Marquardt, A., and Hangartner, I.L. (2021). A transient developmental increase in prefrontal activity alters network maturation and causes cognitive dysfunction in adult mice. *Neuron* 109, 1350–1364.e6.
3. Medendorp, W.E., Bjorefeldt, A., Crespo, E.L., Prakash, M., Pal, A., Waddell, M.L., Moore, C.I., and Hochgeschwender, U. (2021). Selective postnatal excitation of neocortical pyramidal neurons results in distinctive behavioral and circuit deficits in adulthood. *iScience* 24, 102157.
4. Arguello, P.A., and Gogos, J.A. (2012). Genetic and cognitive windows into circuit mechanisms of psychiatric disease. *Trends Neurosci.* 35, 3–13.
5. Prinz, M., Jung, S., and Priller, J. (2019). Microglia Biology: One Century of Evolving Concepts. *Cell* 179, 292–311.
6. Frost, J.L., and Schafer, D.P. (2016). Microglia: Architects of the Developing Nervous System. *Trends Cell Biol.* 26, 587–597.
7. Bennett, F.C., and Molofsky, A.V. (2019). The immune system and psychiatric disease: a basic science perspective. *Clin. Exp. Immunol.* 197, 294–307.

(H) Representative images of Parvalbumin<sup>+</sup> neurons in somatosensory cortex of P15 *Ifnar1*<sup>+/+</sup> and *Ifnar1*<sup>-/-</sup> mice. White lines on the left highlight cortical layers (scale bars, 100 μm).

(I) Relative Parvalbumin<sup>+</sup> neuron density in all cortical layers of the somatosensory cortex in P15 *Ifnar1*<sup>+/+</sup> and *Ifnar1*<sup>-/-</sup> mice (n = 6 mice per group).

(J) Schematic of whisker nuisance assay. A higher score reflects increased aversive response to tactile stimulus. See [STAR Methods](#).

(K) Whisker nuisance score in P15 *Ifnar1*<sup>+/+</sup> and *Ifnar1*<sup>-/-</sup> mice (n = 5 *Ifnar1*<sup>+/+</sup> mice, 7 *Ifnar1*<sup>-/-</sup>, 3 independent experiments).

(L) Whisker nuisance score in P15 *Ifnar1*<sup>fl/fl</sup> vs. *Cx3cr1*<sup>CRE</sup>:*Ifnar1*<sup>fl/fl</sup> mice (n = 10 *Ifnar1*<sup>fl/fl</sup> mice, 14 *Cx3cr1*<sup>CRE</sup>:*Ifnar1*<sup>fl/fl</sup>, 4 independent experiments).

(M) Whisker nuisance score in P15 *Ifnar1*<sup>fl/fl</sup> vs. *Syn1*<sup>CRE</sup>:*Ifnar1*<sup>fl/fl</sup> mice (n = 7 *Ifnar1*<sup>fl/fl</sup> mice, 9 *Syn1*<sup>CRE</sup>:*Ifnar1*<sup>fl/fl</sup>, 2 independent experiments).

Data are represented as mean ± SEM unless otherwise noted. Dots represent independent animals unless otherwise noted.

Statistics: Welch's t test (C, G, I, K, L, and M).

See also [Figure S7](#).

8. Srinivasan, K., Friedman, B.A., Larson, J.L., Lauffer, B.E., Goldstein, L.D., Appling, L.L., Borneo, J., Poon, C., Ho, T., Cai, F., et al. (2016). Untangling the brain's neuroinflammatory and neurodegenerative transcriptional responses. *Nat. Commun.* 7, 11295.
9. McNab, F., Mayer-Barber, K., Sher, A., Wack, A., and O'Garra, A. (2015). Type I interferons in infectious disease. *Nat. Rev. Immunol.* 15, 87–103.
10. Vainchtein, I.D., and Molofsky, A.V. (2020). Astrocytes and Microglia: In Sickness and in Health. *Trends Neurosci.* 43, 144–154.
11. Gosselin, D., Skola, D., Coufal, N.G., Holtman, I.R., Schlachetzki, J.C.M., Sajti, E., Jaeger, B.N., O'Connor, C., Fitzpatrick, C., Pasillas, M.P., et al. (2017). An environment-dependent transcriptional network specifies human microglia identity. *Science* 356, eaal3222.
12. Badimon, A., Strasburger, H.J., Ayata, P., Chen, X., Nair, A., Ikegami, A., Hwang, P., Chan, A.T., Graves, S.M., Uweru, J.O., et al. (2020). Negative feedback control of neuronal activity by microglia. *Nature* 586, 417–423.
13. Van der Loos, H., and Woolsey, T.A. (1973). Somatosensory cortex: structural alterations following early injury to sense organs. *Science* 179, 395–398.
14. Erzurumlu, R.S., and Gaspar, P. (2012). Development and critical period plasticity of the barrel cortex. *Eur. J. Neurosci.* 35, 1540–1553.
15. Sehara, K., and Kawasaki, H. (2011). Neuronal circuits with whisker-related patterns. *Mol. Neurobiol.* 43, 155–162.
16. Woolsey, T.A., and Wann, J.R. (1976). Areal changes in mouse cortical barrels following vibrissal damage at different postnatal ages. *J. Comp. Neurol.* 170, 53–66.
17. Jeammonod, D., Rice, F.L., and Van der Loos, H. (1981). Mouse somatosensory cortex: alterations in the barrelfield following receptor injury at different early postnatal ages. *Neuroscience* 6, 1503–1535.
18. Sehara, K., Toda, T., Iwai, L., Wakimoto, M., Tanno, K., Matsubayashi, Y., and Kawasaki, H. (2010). Whisker-related axonal patterns and plasticity of layer 2/3 neurons in the mouse barrel cortex. *J. Neurosci.* 30, 3082–3092.
19. Hoshiko, M., Arnoux, I., Avignone, E., Yamamoto, N., and Audinat, E. (2012). Deficiency of the microglial receptor CX3CR1 impairs postnatal functional development of thalamocortical synapses in the barrel cortex. *J. Neurosci.* 32, 15106–15111.
20. Feldmeyer, D., Brecht, M., Helmchen, F., Petersen, C.C.H., Poulet, J.F.A., Staiger, J.F., Luhmann, H.J., and Schwarz, C. (2013). Barrel cortex function. *Prog. Neurobiol.* 103, 3–27.
21. Gunner, G., Cheadle, L., Johnson, K.M., Ayata, P., Badimon, A., Mondo, E., Nagy, M.A., Liu, L., Bemiller, S.M., Kim, K.W., et al. (2019). Sensory lesioning induces microglial synapse elimination via ADAM10 and fractalkine signaling. *Nat. Neurosci.* 22, 1075–1088.
22. Zhou, Y., Zhou, B., Pache, L., Chang, M., Khodabakhshi, A.H., Tanaseichuk, O., Benner, C., and Chanda, S.K. (2019). Metascape provides a biologist-oriented resource for the analysis of systems-level datasets. *Nat. Commun.* 10, 1523.
23. Pollina, E.A., Gilliam, D.T., Landau, A.T., Lin, C., Pajarillo, N., Davis, C.P., Harmin, D.A., Yap, E.L., Vogel, I.R., Griffith, E.C., et al. (2023). A NPAS4-NuA4 complex couples synaptic activity to DNA repair. *Nature* 614, 732–741.
24. Madabhushi, R., Gao, F., Pfenning, A.R., Pan, L., Yamakawa, S., Seo, J., Rueda, R., Phan, T.X., Yamakawa, H., Pao, P.C., et al. (2015). Activity-Induced DNA Breaks Govern the Expression of Neuronal Early-Response Genes. *Cell* 161, 1592–1605.
25. Suberbelle, E., Sanchez, P.E., Kravitz, A.V., Wang, X., Ho, K., Eilertson, K., Devidze, N., Kreitzer, A.C., and Mucke, L. (2013). Physiologic brain activity causes DNA double-strand breaks in neurons, with exacerbation by amyloid- $\beta$ . *Nat. Neurosci.* 16, 613–621.
26. Marek, R., Caruso, M., Rostami, A., Grinspan, J.B., and Das Sarma, J. (2008). Magnetic cell sorting: a fast and effective method of concurrent isolation of high purity viable astrocytes and microglia from neonatal mouse brain tissue. *J. Neurosci. Methods* 175, 108–118.
27. Bennett, F.C., Bennett, M.L., Yaqoob, F., Mulinyawe, S.B., Grant, G.A., Hayden Gephart, M., Plowey, E.D., and Barres, B.A. (2018). A Combination of Ontogeny and CNS Environment Establishes Microglial Identity. *Neuron* 98, 1170–1183.e8.
28. Hammond, T.R., Dufort, C., Dissing-Olesen, L., Giera, S., Young, A., Wysocki, A., Walker, A.J., Gergits, F., Segel, M., Nemesh, J., et al. (2019). Single-Cell RNA Sequencing of Microglia throughout the Mouse Lifespan and in the Injured Brain Reveals Complex Cell-State Changes. *Immunity* 50, 253–271.e6.
29. Li, Q., Cheng, Z., Zhou, L., Darmanis, S., Neff, N.F., Okamoto, J., Gulati, G., Bennett, M.L., Sun, L.O., Clarke, L.E., et al. (2019). Developmental Heterogeneity of Microglia and Brain Myeloid Cells Revealed by Deep Single-Cell RNA Sequencing. *Neuron* 101, 207–223.e10.
30. Keren-Shaul, H., Spinrad, A., Weiner, A., Matcovitch-Natan, O., Dvir-Szternfeld, R., Ulland, T.K., David, E., Baruch, K., Lara-Astaiso, D., Toth, B., et al. (2017). A Unique Microglia Type Associated with Restricting Development of Alzheimer's Disease. *Cell* 169, 1276–1290.e17.
31. Friedman, B.A., Srinivasan, K., Ayalon, G., Meilandt, W.J., Lin, H., Huntley, M.A., Cao, Y., Lee, S.H., Haddick, P.C.G., Ngu, H., et al. (2018). Diverse Brain Myeloid Expression Profiles Reveal Distinct Microglial Activation States and Aspects of Alzheimer's Disease Not Evident in Mouse Models. *Cell Rep.* 22, 832–847.
32. Sala Frigerio, C., Wolfs, L., Fattorelli, N., Thrupp, N., Voytyuk, I., Schmidt, I., Mancuso, R., Chen, W.T., Woodbury, M.E., Srivastava, G., et al. (2019). The Major Risk Factors for Alzheimer's Disease: Age, Sex, and Genes Modulate the Microglia Response to  $\text{A}\beta$  Plaques. *Cell Rep.* 27, 1293–1306.e6.
33. Zhan, L., Fan, L., Kodama, L., Sohn, P.D., Wong, M.Y., Mousa, G.A., Zhou, Y., Li, Y., and Gan, L. (2020). A MAC2-positive progenitor-like microglial population is resistant to CSF1R inhibition in adult mouse brain. *eLife* 9, e51796.
34. Ochocka, N., Segit, P., Walentynowicz, K.A., Wojnicki, K., Cyranowski, S., Swatler, J., Mieczkowski, J., and Kaminska, B. (2021). Single-cell RNA sequencing reveals functional heterogeneity of glioma-associated brain macrophages. *Nat. Commun.* 12, 1151.
35. Masuda, T., Sankowski, R., Staszewski, O., Böttcher, C., Amann, L., Sagar, S., Scheiwe, C., Nessler, S., Kunz, P., van Loo, G., et al. (2019). Spatial and temporal heterogeneity of mouse and human microglia at single-cell resolution. *Nature* 566, 388–392.
36. Shi, L., Sun, Z., Su, W., Xu, F., Xie, D., Zhang, Q., Dai, X., Iyer, K., Hitchens, T.K., Foley, L.M., et al. (2021). Treg cell-derived osteopontin promotes microglia-mediated white matter repair after ischemic stroke. *Immunity* 54, 1527–1542.e8.
37. Lee, S.-H., Meilandt, W.J., Xie, L., Gandham, V.D., Ngu, H., Barck, K.H., Rezzonico, M.G., Imperio, J., Lalehzadeh, G., Huntley, M.A., et al. (2021). Trem2 restrains the enhancement of tau accumulation and neurodegeneration by  $\beta$ -amyloid pathology. *Neuron* 109, 1283–1301.e6.
38. Syage, A.R., Ekiz, H.A., Skinner, D.D., Stone, C., O'Connell, R.M., and Lane, T.E. (2020). Single-Cell RNA Sequencing Reveals the Diversity of the Immunological Landscape following Central Nervous System Infection by a Murine Coronavirus. *J. Virol.* 94, e01295-20.
39. Hur, J.Y., Frost, G.R., Wu, X., Crump, C., Pan, S.J., Wong, E., Barros, M., Li, T., Nie, P., Zhai, Y., et al. (2020). The innate immunity protein IFITM3 modulates  $\gamma$ -secretase in Alzheimer's disease. *Nature* 586, 735–740.
40. Bailey, C.C., Zhong, G., Huang, I.C., and Farzan, M. (2014). IFITM-Family Proteins: The Cell's First Line of Antiviral Defense. *Annu. Rev. Virol.* 1, 261–283.
41. Brass, A.L., Huang, I.C., Benita, Y., John, S.P., Krishnan, M.N., Feeley, E.M., Ryan, B.J., Weyer, J.L., van der Weyden, L., Fikrig, E., et al. (2009). The IFITM proteins mediate cellular resistance to influenza A H1N1 virus, West Nile virus, and dengue virus. *Cell* 139, 1243–1254.
42. (2022). Long-term neurological sequelae of SARS-CoV-2 infection. *Nat. Med.* 28, 2269–2270.

43. Xu, E., Xie, Y., and Al-Aly, Z. (2022). Long-term neurologic outcomes of COVID-19. *Nat. Med.* 28, 2406–2415.
44. Taquet, M., Sillett, R., Zhu, L., Mendel, J., Campilisso, I., Dercon, Q., and Harrison, P.J. (2022). Neurological and psychiatric risk trajectories after SARS-CoV-2 infection: an analysis of 2-year retrospective cohort studies including 1 284 437 patients. *Lancet Psychiatry* 9, 815–827.
45. Moreau, G.B., Burgess, S.L., Sturek, J.M., Donlan, A.N., Petri, W.A., and Mann, B.J. (2020). Evaluation of K18-hACE2 Mice as a Model of SARS-CoV-2 Infection. *Am. J. Trop. Med. Hyg.* 103, 1215–1219.
46. Winkler, E.S., Bailey, A.L., Kafai, N.M., Nair, S., McCune, B.T., Yu, J., Fox, J.M., Chen, R.E., Earnest, J.T., Keeler, S.P., et al. (2020). SARS-CoV-2 infection of human ACE2-transgenic mice causes severe lung inflammation and impaired function. *Nat. Immunol.* 21, 1327–1335.
47. McCray, P.B., Jr., Pewe, L., Wohlford-Lenane, C., Hickey, M., Manzel, L., Shi, L., Netland, J., Jia, H.P., Halabi, C., Sigmund, C.D., et al. (2007). Lethal infection of K18-hACE2 mice infected with severe acute respiratory syndrome coronavirus. *J. Virol.* 81, 813–821.
48. Kumari, P., Rothan, H.A., Natekar, J.P., Stone, S., Pathak, H., Strate, P.G., Arora, K., Brinton, M.A., and Kumar, M. (2021). Neuroinvasion and Encephalitis Following Intranasal Inoculation of SARS-CoV-2 in K18-hACE2 Mice. *Viruses* 13, 132.
49. Baruch, K., Deczkowska, A., David, E., Castellano, J.M., Miller, O., Kertser, A., Berkutzki, T., Barnett-Itzhaki, Z., Bezalel, D., Wyss-Coray, T., et al. (2014). Aging. Aging-induced type I interferon response at the choroid plexus negatively affects brain function. *Science* 346, 89–93.
50. Roy, E.R., Wang, B., Wan, Y.W., Chiu, G., Cole, A., Yin, Z., Propson, N.E., Xu, Y., Jankowsky, J.L., Liu, Z., et al. (2020). Type I interferon response drives neuroinflammation and synapse loss in Alzheimer disease. *J. Clin. Invest.* 130, 1912–1930.
51. Roy, E.R., Chiu, G., Li, S., Propson, N.E., Kanchi, R., Wang, B., Coarfa, C., Zheng, H., and Cao, W. (2022). Concerted type I interferon signaling in microglia and neural cells promotes memory impairment associated with amyloid  $\beta$  plaques. *Immunity* 55, 879–894.e6.
52. Udeochu, J.C., Amin, S., Huang, Y., Fan, L., Torres, E.R.S., Carling, G.K., Liu, B., McGurran, H., Coronas-Samano, G., Kauwe, G., et al. (2023). Tau activation of microglial cGAS-IFN reduces MEF2C-mediated cognitive resilience. *Nat. Neurosci.* 26, 737–750.
53. Uccellini, M.B., and García-Sastre, A. (2018). ISRE-Reporter Mouse Reveals High Basal and Induced Type I IFN Responses in Inflammatory Monocytes. *Cell Rep.* 25, 2784–2796.e3.
54. Liberatore, R.A., and Bieniasz, P.D. (2011). Tetherin is a key effector of the antiretroviral activity of type I interferon in vitro and in vivo. *Proc. Natl. Acad. Sci. USA* 108, 18097–18101.
55. Bergen, V., Lange, M., Peidli, S., Wolf, F.A., and Theis, F.J. (2020). Generalizing RNA velocity to transient cell states through dynamical modeling. *Nat. Biotechnol.* 38, 1408–1414.
56. Sánchez-Madrid, F., and Serrador, J.M. (2009). Bringing up the rear: defining the roles of the uropod. *Nat. Rev. Mol. Cell Biol.* 10, 353–359.
57. Chistiakov, D.A., Killingsworth, M.C., Myasoedova, V.A., Orekhov, A.N., and Bobryshev, Y.V. (2017). CD68/macrosialin: not just a histochemical marker. *Lab. Invest.* 97, 4–13.
58. Harris, J.A., Hirokawa, K.E., Sorensen, S.A., Gu, H., Mills, M., Ng, L.L., Bohn, P., Mortrud, M., Ouellette, B., Kidney, J., et al. (2014). Anatomical characterization of Cre driver mice for neural circuit mapping and manipulation. *Front. Neural Circuits* 8, 76.
59. Madisen, L., Zwingman, T.A., Sunkin, S.M., Oh, S.W., Zariwala, H.A., Gu, H., Ng, L.L., Palmiter, R.D., Hawrylycz, M.J., Jones, A.R., et al. (2010). A robust and high-throughput Cre reporting and characterization system for the whole mouse brain. *Nat. Neurosci.* 13, 133–140.
60. Villani, A., Benjamin, J., Moritz, C., Henke, K., Hartmann, J., Norlin, N., Richter, K., Schieber, N.L., Franke, T., Schwab, Y., et al. (2019). Clearance by Microglia Depends on Packaging of Phagosomes into a Unique Cellular Compartment. *Dev. Cell* 49, 77–88.e7.
61. Zhang, Y., Chen, K., Sloan, S.A., Bennett, M.L., Scholze, A.R., O'Keeffe, S., Phatnani, H.P., Guarneri, P., Caneda, C., Ruderisch, N., et al. (2014). An RNA-sequencing transcriptome and splicing database of glia, neurons, and vascular cells of the cerebral cortex. *J. Neurosci.* 34, 11929–11947.
62. McKinsey, G.L., Lizama, C.O., Keown-Lang, A.E., Niu, A., Santander, N., Larphaveesarp, A., Chee, E., Gonzalez, F.F., and Arnold, T.D. (2020). A new genetic strategy for targeting microglia in development and disease. *eLife* 9, e54590.
63. Faust, T.E., Feinberg, P.A., O'Connor, C., Kawaguchi, R., Chan, A., Strasburger, H., Frosch, M., Boyle, M.A., Masuda, T., Amann, L., et al. (2023). A comparative analysis of microglial inducible Cre lines. *Cell Rep.* 42, 113031.
64. Gough, D.J., Messina, N.L., Clarke, C.J.P., Johnstone, R.W., and Levy, D.E. (2012). Constitutive type I interferon modulates homeostatic balance through tonic signaling. *Immunity* 36, 166–174.
65. Town, T., Jeng, D., Alexopoulou, L., Tan, J., and Flavell, R.A. (2006). Microglia recognize double-stranded RNA via TLR3. *J. Immunol.* 176, 3804–3812.
66. Secombes, C.J., and Zou, J. (2017). Evolution of Interferons and Interferon Receptors. *Front. Immunol.* 8, 209.
67. Boudinot, P., Langevin, C., Secombes, C.J., and Levraud, J.P. (2016). The Peculiar Characteristics of Fish Type I Interferons. *Viruses* 8, 298.
68. Silva, N.J., Dorman, L.C., Vainchtein, I.D., Horneck, N.C., and Molofsky, A.V. (2021). In situ and transcriptomic identification of microglia in synapse-rich regions of the developing zebrafish brain. *Nat. Commun.* 12, 5916.
69. Peri, F., and Nüsslein-Volhard, C. (2008). Live Imaging of Neuronal Degradation by Microglia Reveals a Role for v0-ATPase a1 in Phagosomal Fusion In Vivo. *Cell* 133, 916–927.
70. Wong, F.K., and Marín, O. (2019). Developmental Cell Death in the Cerebral Cortex. *Annu. Rev. Cell Dev. Biol.* 35, 523–542.
71. Harb, K., Magrinelli, E., Nicolas, C.S., Lukianets, N., Frangeul, L., Pietri, M., Sun, T., Sandoz, G., Grammont, F., Jabaudon, D., et al. (2016). Area-specific development of distinct projection neuron subclasses is regulated by postnatal epigenetic modifications. *eLife* 5, e09531.
72. McNamara, K.C.S., Lisembee, A.M., and Lifshitz, J. (2010). The whisker nuisance task identifies a late-onset, persistent sensory sensitivity in diffuse brain-injured rats. *J. Neurotrauma* 27, 695–706.
73. Balasco, L., Chelini, G., Bozzi, Y., and Provenzano, G. (2019). Whisker Nuisance Test: A Valuable Tool to Assess Tactile Hypersensitivity in Mice. *Bio Protoc.* 9, e3331.
74. Chelini, G., Zerbi, V., Cimino, L., Grigoli, A., Markicevic, M., Libera, F., Robbiati, S., Gadler, M., Bronzoni, S., Miorelli, S., et al. (2019). Aberrant Somatosensory Processing and Connectivity in Mice Lacking *Engrailed-2*. *J. Neurosci.* 39, 1525–1538.
75. Ivashkiv, L.B., and Donlin, L.T. (2014). Regulation of type I interferon responses. *Nat. Rev. Immunol.* 14, 36–49.
76. Brendecke, S.M., and Prinz, M. (2012). How type I interferons shape myeloid cell function in CNS autoimmunity. *J. Leukoc. Biol.* 92, 479–488.
77. Kumaran Satyanarayanan, S., El Kebir, D., Soboh, S., Butenko, S., Sekheri, M., Saadi, J., Peled, N., Assi, S., Othman, A., Schif-Zuck, S., et al. (2019). IFN- $\beta$  is a macrophage-derived effector cytokine facilitating the resolution of bacterial inflammation. *Nat. Commun.* 10, 3471.
78. Diaz-Aparicio, I., Paris, I., Sierra-Torre, V., Plaza-Zabala, A., Rodríguez-Iglesias, N., Márquez-Ropero, M., Beccari, S., Huguet, P., Abiega, O., Alberdi, E., et al. (2020). Microglia Actively Remodel Adult Hippocampal Neurogenesis through the Phagocytosis Secretome. *J. Neurosci.* 40, 1453–1482.
79. Li, X., Deng, M., Petrucci, A.S., Zhu, C., Mo, J., Zhang, L., Tam, J.W., Ariel, P., Zhao, B., Zhang, S., et al. (2019). Viral DNA Binding to NLRC3, an Inhibitory Nucleic Acid Sensor, Unleashes STING, a Cyclic

- Dinucleotide Receptor that Activates Type I Interferon. *Immunity* 50, 591–599.e6.
80. Takaoka, A., and Yamada, T. (2019). Regulation of signaling mediated by nucleic acid sensors for innate interferon-mediated responses during viral infection. *Int. Immunol.* 31, 477–488.
  81. Boada-Romero, E., Martinez, J., Heckmann, B.L., and Green, D.R. (2020). The clearance of dead cells by efferocytosis. *Nat. Rev. Mol. Cell Biol.* 21, 398–414.
  82. Chen, Q., Sun, L., and Chen, Z.J. (2016). Regulation and function of the cGAS-STING pathway of cytosolic DNA sensing. *Nat. Immunol.* 17, 1142–1149.
  83. Dorrity, T.J., Shin, H., Wiegand, K.A., Aruda, J., Closser, M., Jung, E., Gertie, J.A., Leone, A., Polfer, R., Culbertson, B., et al. (2023). Long 3'UTRs predispose neurons to inflammation by promoting immunostimulatory double-stranded RNA formation. *Sci. Immunol.* 8, eadg2979.
  84. Chauhan, S., Kumar, S., Jain, A., Ponpuak, M., Mudd, M.H., Kimura, T., Choi, S.W., Peters, R., Mandell, M., Bruun, J.A., et al. (2016). TRIMs and galectins globally cooperate and TRIM16 and galectin-3 co-direct autophagy in endomembrane damage homeostasis. *Dev. Cell* 39, 13–27.
  85. Feldmeyer, D. (2012). Excitatory neuronal connectivity in the barrel cortex. *Front. Neuroanat.* 6, 24.
  86. Zhao, J., Zhang, W., Wu, T., Wang, H., Mao, J., Liu, J., Zhou, Z., Lin, X., Yan, H., and Wang, Q. (2021). Efferocytosis in the Central Nervous System. *Front. Cell Dev. Biol.* 9, 773344.
  87. Möller, K., Brambach, M., Villani, A., Gallo, E., Gilmour, D., and Peri, F. (2022). A role for the centrosome in regulating the rate of neuronal efferocytosis by microglia *in vivo*. *eLife* 11, e82094.
  88. Kocur, M., Schneider, R., Pulm, A.K., Bauer, J., Kropp, S., Gliem, M., In-gwersen, J., Goebels, N., Alferink, J., Prozorovski, T., et al. (2015). IFN $\beta$  secreted by microglia mediates clearance of myelin debris in CNS autoimmunity. *Acta Neuropathol. Commun.* 3, 20.
  89. Blank, T., and Prinz, M. (2017). Type I interferon pathway in CNS homeostasis and neurological disorders. *Glia* 65, 1397–1406.
  90. Mukherjee, P., Woods, T.A., Moore, R.A., and Peterson, K.E. (2013). Activation of the innate signaling molecule MAVS by bunyavirus infection upregulates the adaptor protein SARM1, leading to neuronal death. *Immunity* 38, 705–716.
  91. Viengkhou, B., and Hofer, M.J. (2023). Breaking down the cellular responses to type I interferon neurotoxicity in the brain. *Front. Immunol.* 14, 1110593.
  92. Malle, L., and Bogunovic, D. (2021). Down syndrome and type I interferon: not so simple. *Curr. Opin. Immunol.* 72, 196–205.
  93. Chung, H., Green, P.H.R., Wang, T.C., and Kong, X.F. (2021). Interferon-Driven Immune Dysregulation in Down Syndrome: A Review of the Evidence. *J. Inflamm. Res.* 14, 5187–5200.
  94. Waugh, K.A., Minter, R., Baxter, J., Chi, C., Galbraith, M.D., Tuttle, K.D., Eduthan, N.P., Kinning, K.T., Andrysiak, Z., Araya, P., et al. (2023). Triplification of the interferon receptor locus contributes to hallmarks of Down syndrome in a mouse model. *Nat. Genet.* 55, 1034–1047.
  95. Jin, M., Xu, R., Wang, L., Alam, M.M., Ma, Z., Zhu, S., Martini, A.C., Jadalali, A., Bernabucci, M., Xie, P., et al. (2022). Type-I-interferon signaling drives microglial dysfunction and senescence in human iPSC models of Down syndrome and Alzheimer's disease. *Cell Stem Cell* 29, 1135–1153.e8.
  96. Knuesel, I., Chicha, L., Britschgi, M., Schobel, S.A., Bodmer, M., Hellings, J.A., Toovey, S., and Prinsen, E.P. (2014). Maternal immune activation and abnormal brain development across CNS disorders. *Nat. Rev. Neurol.* 10, 643–660.
  97. Website American Psychiatric Association (2013). Diagnostic and Statistical Manual of Mental Disorders, Fifth Edition (American Psychiatric Association).
  98. Mikkelsen, M., Wodka, E.L., Mostofsky, S.H., and Puts, N.A.J. (2018). Autism spectrum disorder in the scope of tactile processing. *Dev. Cogn. Neurosci.* 29, 140–150.
  99. Malkova, N.V., Yu, C.Z., Hsiao, E.Y., Moore, M.J., and Patterson, P.H. (2012). Maternal immune activation yields offspring displaying mouse versions of the three core symptoms of autism. *Brain Behav. Immun.* 26, 607–616.
  100. Masuda, T., Amann, L., Sankowski, R., Staszewski, O., Lenz, M., Errico, P.D., Snaidero, N., Costa Jordão, M.J., Böttcher, C., Kierdorf, K., et al. (2020). Novel Hexb-based tools for studying microglia in the CNS. *Nat. Immunol.* 21, 802–815.
  101. Wang, Y., Cella, M., Mallinson, K., Ulrich, J.D., Young, K.L., Robinette, M.L., Gilfillan, S., Krishnan, G.M., Sudhakar, S., Zinselmeyer, B.H., et al. (2015). TREM2 lipid sensing sustains the microglial response in an Alzheimer's disease model. *Cell* 160, 1061–1071.
  102. Orre, M., Kamphuis, W., Osborn, L.M., Jansen, A.H.P., Kooijman, L., Bossers, K., and Hol, E.M. (2014). Isolation of glia from Alzheimer's mice reveals inflammation and dysfunction. *Neurobiol. Aging* 35, 2746–2760.
  103. Chiu, I.M., Morimoto, E.T.A., Goodarzi, H., Liao, J.T., O'Keefe, S., Phatnani, H.P., Muratet, M., Carroll, M.C., Levy, S., Tavazoie, S., et al. (2013). A neurodegeneration-specific gene-expression signature of acutely isolated microglia from an amyotrophic lateral sclerosis mouse model. *Cell Rep.* 4, 385–401.
  104. Verheijden, S., Beckers, L., Casazza, A., Butovsky, O., Mazzone, M., and Baes, M. (2015). Identification of a chronic non-neurodegenerative microglia activation state in a mouse model of peroxisomal β-oxidation deficiency. *Glia* 63, 1606–1620.
  105. Arumugam, T.V., Manzanero, S., Furtado, M., Biggins, P.J., Hsieh, Y.H., Gelderblom, M., MacDonald, K.P., Salimova, E., Li, Y.I., Korn, O., et al. (2017). An atypical role for the myeloid receptor Mincle in central nervous system injury. *J. Cereb. Blood Flow Metab.* 37, 2098–2111.
  106. Poliani, P.L., Wang, Y., Fontana, E., Robinette, M.L., Yamanishi, Y., Gilfillan, S., and Colonna, M. (2015). TREM2 sustains microglial expansion during aging and response to demyelination. *J. Clin. Invest.* 125, 2161–2170.
  107. Erny, D., Hrabé de Angelis, A.L., Jaitin, D., Wieghofer, P., Staszewski, O., David, E., Keren-Shaul, H., Mahlková, T., Jakobshagen, K., Buch, T., et al. (2015). Host microbiota constantly control maturation and function of microglia in the CNS. *Nat. Neurosci.* 18, 965–977.
  108. Szulzewsky, F., Pelz, A., Feng, X., Synowitz, M., Markovic, D., Langmann, T., Holtzman, I.R., Wang, X., Eggen, B.J.L., Boddeke, H.W.G.M., et al. (2015). Glioma-associated microglia/macrophages display an expression profile different from M1 and M2 polarization and highly express Gpnmb and Spp1. *PLoS One* 10, e0116644.
  109. Bruttger, J., Karram, K., Wörtge, S., Regen, T., Marini, F., Hoppmann, N., Klein, M., Blank, T., Yona, S., Wolf, Y., et al. (2015). Genetic cell ablation reveals clusters of local self-renewing microglia in the mammalian central nervous system. *Immunity* 43, 92–106.
  110. Grabert, K., Michoel, T., Karavolos, M.H., Clohissey, S., Baillie, J.K., Stevens, M.P., Freeman, T.C., Summers, K.M., and McColl, B.W. (2016). Microglial brain region-dependent diversity and selective regional sensitivities to aging. *Nat. Neurosci.* 19, 504–516.
  111. Jung, S., Alberti, J., Graemmel, P., Sunshine, M.J., Kreutzberg, G.W., Sher, A., and Litman, D.R. (2000). Analysis of fractalkine receptor CX(3)CR1 function by targeted deletion and green fluorescent protein reporter gene insertion. *Mol. Cell. Biol.* 20, 4106–4114.
  112. Gong, S., Zheng, C., Doughty, M.L., Losos, K., Didkovsky, N., Schambra, U.B., Nowak, N.J., Joyner, A., Leblanc, G., Hatten, M.E., et al. (2003). A gene expression atlas of the central nervous system based on bacterial artificial chromosomes. *Nature* 425, 917–925.
  113. Prigge, J.R., Hoyt, T.R., Dobrin, E., Capecchi, M.R., Schmidt, E.E., and Meissner, N. (2015). Type I IFNs Act upon Hematopoietic Progenitors To

- Protect and Maintain Hematopoiesis during *Pneumocystis* Lung Infection in Mice. *J. Immunol.* 195, 5347–5357.
114. Zhao, X.F., Alam, M.M., Liao, Y., Huang, T., Mathur, R., Zhu, X., and Huang, Y. (2019). Targeting Microglia Using Cx3cr1-Cre Lines: Revisiting the Specificity. *eNeuro* 6. ENEURO.0114-19.2019.
  115. Oakley, H., Cole, S.L., Logan, S., Maus, E., Shao, P., Craft, J., Guillozet-Bongaarts, A., Ohno, M., Disterhoft, J., Van Eldik, L., et al. (2006). Intraneuronal beta-amyloid aggregates, neurodegeneration, and neuron loss in transgenic mice with five familial Alzheimer's disease mutations: potential factors in amyloid plaque formation. *J. Neurosci.* 26, 10129–10140.
  116. La Manno, G., Soldatov, R., Zeisel, A., Braun, E., Hochgerner, H., Petukhov, V., Lidschreiber, K., Kastriti, M.E., Lönnberg, P., Furlan, A., et al. (2018). RNA velocity of single cells. *Nature* 560, 494–498.
  117. Paredes, M.F., Li, G., Berger, O., Baraban, S.C., and Pleasure, S.J. (2006). Stromal-derived factor-1 (CXCL12) regulates laminar position of Cajal-Retzius cells in normal and dysplastic brains. *J. Neurosci.* 26, 9404–9412.
  118. Galatro, T.F., Vainchtein, I.D., Brouwer, N., Boddeke, E.W.G.M., and Eggen, B.J.L. (2017). Isolation of Microglia and Immune Infiltrates from Mouse and Primate Central Nervous System. *Methods Mol. Biol.* 1559, 333–342.
  119. Negrini, M., Wang, G., Heuer, A., Björklund, T., and Davidsson, M. (2020). AAV Production Everywhere: A Simple, Fast, and Reliable Protocol for In-house AAV Vector Production Based on Chloroform Extraction. *Curr. Protoc. Neurosci.* 93, e103.
  120. Tse, C., Shoemaker, A.R., Adickes, J., Anderson, M.G., Chen, J., Jin, S., Johnson, E.F., Marsh, K.C., Mitten, M.J., Nimmer, P., et al. (2008). ABT-263: a potent and orally bioavailable Bcl-2 family inhibitor. *Cancer Res.* 68, 3421–3428.
  121. Butler, A., Hoffman, P., Smibert, P., Papalexi, E., and Satija, R. (2018). Integrating single-cell transcriptomic data across different conditions, technologies, and species. *Nat. Biotechnol.* 36, 411–420.
  122. Macosko, E.Z., Basu, A., Satija, R., Nemesh, J., Shekhar, K., Goldman, M., Tirosh, I., Bialas, A.R., Kamitaki, N., Martersteck, E.M., et al. (2015). Highly Parallel Genome-wide Expression Profiling of Individual Cells Using Nanoliter Droplets. *Cell* 161, 1202–1214.
  123. Hoffman, G.E., and Schadt, E.E. (2016). variancePartition: interpreting drivers of variation in complex gene expression studies. *BMC Bioinformatics* 17, 483.
  124. Kowalczyk, M.S., Tirosh, I., Heckl, D., Rao, T.N., Dixit, A., Haas, B.J., Schneider, R.K., Wagers, A.J., Ebert, B.L., and Regev, A. (2015). Single-cell RNA-seq reveals changes in cell cycle and differentiation programs upon aging of hematopoietic stem cells. *Genome Res.* 25, 1860–1872.

## STAR★METHODS

## KEY RESOURCES TABLE

REAGENT or RESOURCE	SOURCE	IDENTIFIER
<b>Antibodies</b>		
Rabbit anti -dsRed 1:1000	Clontech	Cat#632496; RRID:AB_10013483
Rat anti-mCherry 1:1000	Invitrogen	Cat#M11217
Chicken anti-GFP 1:1000	Aves Labs	Cat#1020; RRID:AB_10000240
Chicken anti -NeuN 1:1000	Millipore	Cat#ABN91; RRID:AB_11205760
Rabbit anti -Iba1 1:1000	Wako Chemicals	Cat#019-19741; RRID:AB_839504
Mouse anti -Iba1 1:1000	Wako Chemicals	Cat#016-26721; RRID:AB_2811160
Guinea pig anti-Iba1 1:2000	Synaptic Systems	Cat#234-004; RRID:AB_2493179
Rabbit anti -IFITM3 1:1:1000	Proteintech	Cat#11714-1-AP; RRID:AB_2295684
Guinea pig anti-VGLUT2 1:2000	Synaptic Systems	Cat#135404; RRID:AB_887884
Rat anti -CD68 1:500	Bio-Rad	Cat#MCA1957GA; RRID:AB_322219
Goat anti-rabbit IgG; HRP-linked	Cell Signaling Technology	Cat#7074P2; RRID:AB_2099233
Rabbit anti-SARS-CoV-2-N protein 1 :1000	GeneTex	Cat#GTX135361; RRID:AB_2887484
Mouse anti-SARS-CoV-2-Spike 1:1000	GeneTex	Cat#GTX632604; RRID:AB_2864418
Mouse anti beta amyloid (4G8) 1:500	Biolegend	Cat#800708; RRID:AB_2565324
Rat anti-Bst2/Tetherin	R&D Systems	Cat#MAB8660-SP
Mouse anti p-H2AX 1:500	EMD Millipore	Cat#05-636; RRID:AB_2924829
Rabbit anti-53BP 1:500	Novus Biologicals	Cat#NB100-304; RRID:AB_350221
Rat anti-CTIP2 1:500	Biolegend	Cat#650601; RRID:AB_10896795
Rabbit anti-SATB2 1:500	Abcam	Cat#ab92446; RRID:AB_10563678
Mouse anti-Parvalbumin 1:500	Sigma-Aldrich	Cat#P3088; RRID:AB_477329
Rat anti-Somatostatin 1:500	Thermo Fisher	Cat#MA516987; RRID:AB_2538460
Rabbit anti-GAD67 1:500	Thermo Fisher	Cat#PA521397; RRID:AB_11153284
Goat anti-rabbit AF488 1:500	Thermo Fisher	Cat#A-11034; RRID:AB_2576217
Goat anti-rat AF488 1:500	Thermo Fisher	Cat#A-11006; RRID:AB_2534074
Goat anti-guinea pig AF488 1:500	Thermo Fisher	Cat#A-11073; RRID:AB_2534117
Goat anti-chicken AF488 1:500	Thermo Fisher	Cat#A-11039; RRID:AB_2534096
Goat anti-mouse AF488 1:500	Thermo Fisher	Cat#A-11001; RRID:AB_2534069
Goat anti-rabbit AF555 1:500	Thermo Fisher	Cat#A-21428; RRID:AB_2535849
Goat anti-rat AF555 1:500	Thermo Fisher	Cat#A21434; RRID:AB_141733
Goat anti-guinea pig AF555 1:500	Thermo Fisher	Cat#A-21435; RRID:AB_2535856
Goat anti-mouse AF555 1:500	Thermo Fisher	Cat#A-11003; RRID:AB_2534071
Goat anti-chicken AF555 1:500	Thermo Fisher	Cat#A-21437; RRID:AB_2535858
Goat anti-rabbit AF647 1:500	Thermo Fisher	Cat#A-21244; RRID:AB_2535812
Goat anti-rat AF647 1:500	Thermo Fisher	Cat#A-21247; RRID:AB_141778
Goat anti-guinea pig AF647 1:500	Thermo Fisher	Cat#A-21450; RRID:AB_141882
Goat anti-mouse AF647 1:500	Thermo Fisher	Cat#A-21236; RRID:AB_2535805
Goat anti-chicken AF647 1:500	Thermo Fisher	Cat#A-21449; RRID:AB_2535866
Hoechst 33342 solution 1:5000	Thermo Fisher	Cat#62249
TruStain rat anti-CD16/32 1:100	BioLegend	Cat#101319; RRID:AB_1574973
Rabbit anti-IFITM3 1:1:1000	Proteintech	Cat#11714-1-AP; RRID:AB_2295684
FITC rat anti-CD45 1:250	BioLegend	Cat#103108; RRID:AB_312973
APC-Cy7 rat anti-CD45 1:250	Biolegend	Cat#103115; RRID:AB_312981
PE rat anti-CD11b 1:170	eBioscience	Cat#12-0112-81; RRID:AB_465546

(Continued on next page)

**Continued**

REAGENT or RESOURCE	SOURCE	IDENTIFIER
APC rat anti-CD11b 1:170	BioLegend	Cat#101212; RRID:AB_312795
PE-Cy7 rat anti-CD11b 1:170	eBioscience	Cat#25-0112-81; RRID:AB_469587
APC rat anti-P2RY12 1:200	Biolegend	Cat#848005; RRID:AB_2721469
Goat anti-rabbit AF647 1:500	Thermo Fisher	Cat#A-21244; RRID:AB_2535812
PE mouse anti-IFNAR1 1:150	Biolegend	Cat#127311; RRID:AB_2248800
APC mouse anti-IFNAR1 1:150	Biolegend	Cat#127313; RRID:AB_2122746
<b>Chemicals, peptides, and recombinant proteins</b>		
Recombinant IFN-β	R&D Systems	Cat#8234-MB-010/CF
Poly(I:C) HMW	Invivogen	Cat#tlrl-pic
Bafilomycin A1	Tocris	Cat#1334
Tamoxifen, >99%	Sigma-Aldrich	Cat#T5648
ABT-263 (Navitoclax)	MedChemExpress	Cat#HY-10087
Lysotracker Red	Thermo Fisher	Cat#L7528
<b>Critical commercial assays</b>		
DeadEnd Fluorometric TUNEL system	Promega	Cat#G3250
RNAscope® Fluorescent Multiplex Detection Reagents	Advanced Cell Diagnostics	Cat#320851
RNAscope® Multiplex Fluorescent Reagent Kit v2	Advanced Cell Diagnostics	Cat#323100
TSA Plus Cyanine 3 detection kit	Akoya Biosciences	Cat#NEL744001KT
TSA Plus Cyanine 5 detection kit	Akoya Biosciences	Cat#NEL745001KT
TSA Plus Fluorescein detection kit	Akoya Biosciences	Cat#NEL701A001KT
Chromium single cell gene expression platform, version 3 (Microglial RNA-seq)	10x Genomics	Library and gel bead kit – V3, 1000075: Chip B kit: 1000074
MERSCOPE Cell Boundary Staining Kit	Vizgen	PN#10400118
Rneasy Plus Mini Kit	Qiagen	Cat#74134
High Capacity cDNA Reverse Transcription kit	Life Technologies	Cat#4374966
<b>Deposited data</b>		
Single cell RNA-sequencing of microglia from postnatal day 5 and 7 barrel cortex after partial whisker follicle cauterization at postnatal day 2	This paper	GeneExpression Omnibus (GEO) GEO: GSE173173
scRNA-seq: PS2APP;TauP301L with and without Trem2/-	Lee et al. <sup>37</sup>	GEO: GSE153895
scRNA-seq: 5xFAD	Masuda et al. <sup>100</sup>	GEO: GSE148405
scRNA-seq: APP-PS1 with and without Apoe/-	Sala Frigerio et al. <sup>32</sup>	GEO: GSE127884
scRNA-seq: GBM model in mouse	Ochocka et al. <sup>34</sup>	GEO: GSE136001
scRNA-seq: Coronavirus infection (3 days, 7 days post infection)	Syage et al. <sup>38</sup>	Received from author
scRNA-seq: Young (P4-P5), aging (P100, P540), LPC injection	Hammond et al. <sup>28</sup>	GEO: GSE121654
scRNA-seq: PLX5622 recovery	Zhan et al. <sup>33</sup>	GEO: GSE150169
scRNA-seq: tMCAO (5 days and 14 days post occlusion)	Shi et al. <sup>36</sup>	GEO: GSE171169
Bulk seq: PS2APP	Friedman et al. <sup>31</sup>	GEO: GSE89482
Bulk seq: 5XFAD	Wang et al. <sup>101</sup>	GEO: GSE65067
Bulk seq: WT, APPswe/PS1dE9	Orre et al. <sup>102</sup>	GEO: GSE74615
Bulk seq: Thy1::hMAPT-P301L	Friedman et al. <sup>31</sup>	GEO: GSE93179

(Continued on next page)

**Continued**

REAGENT or RESOURCE	SOURCE	IDENTIFIER
Bulk seq: Prnp::hMAPT-P301S	Friedman et al. <sup>31</sup>	GEO: GSE93180
Bulk seq: hSOD1G93A, hSODWT, Non-tg	Chiu et al. <sup>103</sup>	GEO: GSE43366
Bulk seq: Mfp2-/-	Verheijden et al. <sup>104</sup>	GEO: GSE66420
Bulk seq: tMCAO (Ischemia/Reperfusion Injury)	Arumugam et al. <sup>105</sup>	GEO: GSE77986
Bulk seq: Cuprizone, recovery; Trem2-/-	Poliani et al. <sup>106</sup>	GEO: GSE66926
Bulk seq: Intraperitoneal LPS	Srinivasan et al. <sup>8</sup>	GEO: GSE75246
Bulk seq: Germ-free housing; Intraventricular LPS or LCMV	Erny et al. <sup>107</sup>	GEO: GSE67858
Bulk seq: Glioma	Szulzewsky et al. <sup>108</sup>	E-MTAB-2660
Bulk seq: Resting microglia, repopulating microglia, infiltrating macrophages	Bruttger et al. <sup>109</sup>	GEO: GSE68376
Bulk seq: Microglia versus bulk tissue homogenate; Cortex, Hippocampus, Striatum, Cerebellum; 4, 12, 22 months	Grabert et al. <sup>110</sup>	GEO: GSE62420
<b>Experimental models: Cell lines</b>		
HEK293T	Gift of Dr. Martin Kampmann	RRID:CVCL_0063
SH-S5Y5	Gift of Dr. William Weiss	RRID:CVCL_0019
<b>Experimental models: Mouse strains</b>		
Cx3cr1 <sup>GFP</sup>	The Jackson Laboratory, Jung et al. <sup>111</sup>	RRID:IMSR_JAX:005582
C57Bl/6J	The Jackson Laboratory	RRID:IMSR_JAX:000664
Aldh1l1 <sup>eGFP</sup>	The Jackson Laboratory, Gong et al. <sup>112</sup>	GENSAT MGI:3843271
Ifnar1 <sup>-/-</sup>	The Jackson Laboratory, Prigge et al. <sup>113</sup>	RRID:IMSR_JAX:028288
Mx1 <sup>GFP</sup>	The Jackson Laboratory, Uccellini et al. <sup>53</sup>	RRID:IMSR_JAX:033219
Mx1 <sup>CRE</sup>	The Jackson Laboratory	RRID:IMSR_JAX:003556
Ai14 reporter	The Jackson Laboratory, Madisen et al. <sup>59</sup>	RRID:IMSR_JAX:007908
K18-ACE2	The Jackson Laboratory, McCray et al. <sup>47</sup>	RRID:IMSR_JAX:034860
Aldh1l1 <sup>tdTomato</sup>	MMRC	RRID:MMRRC_036700-UCD
Rorb <sup>CRE</sup>	The Jackson Laboratory	RRID:IMSR_JAX:023526
Syn1 <sup>CRE</sup>	The Jackson Laboratory	RRID:IMSR_JAX:003966
Ifnar1 <sup>fl/fl</sup>	The Jackson Laboratory	RRID:IMSR_JAX:028256
Cx3cr1 <sup>CRE</sup>	MMRC, Zhao et al. <sup>114</sup>	RRID:MMRRC_036395-UCD
P2ry12 <sup>CreERT2</sup>	Gift of Dr. Tom Arnold	RRID:IMSR_JAX:034727
Mavs <sup>-/-</sup>	The Jackson Laboratory	RRID:IMSR_JAX:008634
Tlr3 <sup>-/-</sup>	The Jackson Laboratory	RRID:IMSR_JAX:005217
Cgas <sup>-/-</sup>	The Jackson Laboratory	RRID:IMSR_JAX:026554
5xFAD	The Jackson Laboratory, Oakley et al. <sup>115</sup>	RRID:MMRRC_034840-JAX
<b>Experimental models: Zebrafish lines</b>		
Tg(mpeg:EGFP-CAAX)	Francesca Peri Lab, Villani et al. <sup>60</sup>	ZFIN ID: ZDB-TGCONSTRCT-191211-1
Tg(NBT:dsRed)	Christiane Nüsslein-Volhard Lab, Peri et al. <sup>69</sup>	ZFIN ID: ZDB-TGCONSTRCT-081023-2
<b>Oligonucleotides</b>		
Mouse <i>Grin1</i> RNAscope probe	Advanced Cell Diagnostics	Cat#431611
Mouse <i>Rbfox3</i> RNAscope probe	Advanced Cell Diagnostics	Cat#313311-C2
Mouse <i>Ifnar1</i> RNAscope probe	Advanced Cell Diagnostics	Cat#512971-C2
<b>Recombinant DNA</b>		
pAdDeltaF6	Addgene	RRID:Addgene_112867
pUCmini-iCAP-PHP.eB	Addgene	RRID:Addgene_103005
Syn1:NLS-EGFP	This paper	N/A

(Continued on next page)

**Continued**

REAGENT or RESOURCE	SOURCE	IDENTIFIER
Syn1:mifnb1-NLS-EGFP	This paper	N/A
<b>Software and algorithms</b>		
FIJI	Open source	<a href="https://imagej.net/software/fiji/">https://imagej.net/software/fiji/</a>
Imaris v9	Oxford Instruments	<a href="https://imaris.oxinst.com/">https://imaris.oxinst.com/</a>
GraphPad Prism 9.3.1	GraphPad	<a href="https://www.graphpad.com/">https://www.graphpad.com/</a>
Zeiss Zen 2.6 software	Zeiss	N/A
Cell Ranger 2.1	10X Genomics	<a href="https://www.10xgenomics.com/support/software/cell-ranger/latest">https://www.10xgenomics.com/support/software/cell-ranger/latest</a>
Seurat 3.1.4	Satija Lab	<a href="https://satijalab.org/seurat">https://satijalab.org/seurat</a>
Velocyto 0.17	La Manno et al. <sup>116</sup>	<a href="https://velocyto.org/">https://velocyto.org/</a>
ScVelo 0.2.0	Bergen et al. <sup>55</sup>	<a href="https://scvelo.readthedocs.io/en/stable/">https://scvelo.readthedocs.io/en/stable/</a>
Code	This paper	<a href="https://github.com/lcdorman/IFNresponseCode">https://github.com/lcdorman/IFNresponseCode</a>
<b>Other</b>		
MACS beads (LS columns)	Miltenyi Biotec	Cat#130-042-401
MERSCOPE slides	Vizgen	PN#20400001
MERSCOPE Sample Prep Wash Buffer	Vizgen	PN#20300001
MERSCOPE Formamide Wash Buffer	Vizgen	PN#20300002
MERSCOPE PolyT Staining Reagent	Vizgen	PN#20300021

## RESOURCE AVAILABILITY

### Lead contact

Further information and requests for resources and reagents should be directed to and will be fulfilled by the lead contact, Anna Molofsky ([anna.molofsky@ucsf.edu](mailto:anna.molofsky@ucsf.edu)).

### Materials availability

All unique/stable reagents generated in this study are available from the [Lead Contact](#) without restriction.

### Data and code availability

Data availability: RNA sequencing data is available through Gene Expression Omnibus at GEO: GSE173173. Searchable database of this data is also available at <https://www.annamolofskylab.org/microglia-sequencing>. This paper also reanalyzes existing, publicly available data. These accession numbers for the datasets are listed in the [key resources table](#). Microscopy and behavior data reported in this paper will be shared by the [lead contact](#) upon request.

Code availability: R and Python code used to analyze single cell datasets is available on GitHub at <https://github.com/lcdorman/IFNresponseCode>.

Any additional information required to reanalyze the data reported in this paper is available from the [lead contacts](#) upon request.

## EXPERIMENTAL MODEL AND STUDY PARTICIPANT DETAILS

### Mice

All mouse strains were maintained in the University of California, San Francisco specific pathogen-free animal facility, and all animal protocols were approved by and in accordance with the guidelines established by the Institutional Animal Care and Use Committee and Laboratory Animal Resource Center. Mice were housed in a 12-hour light/dark cycle (7am-7pm) at 68-79°F and 30-70% humidity. Male and female mice were group-housed when possible with up to 5 mice per cage. Littermate controls were used for all experiments when feasible. The following mouse strains used are described in the table below and are as referenced in the text: Cx3cr1<sup>GFP</sup> (Jax#00582); Aldh1l1<sup>eGFP</sup> (Gensat); Ifnar1<sup>-/-</sup> (Jax#028288); Mx1<sup>GFP</sup> (Jax#033219); Mx1<sup>CRE</sup> (Jax#003556); Ai14 (Jax#007908); B6.Cg-Tg(K18-ACE2) 2PrIrn/J (Jax#034860); Rorb-Ires2-Cre-D (Jax#023526); Aldh1l1<sup>tdTomato</sup> (MMRRC, RRID:MMRRC\_036700-UCD); B6.Cg-Tg(Syn1-cre)671Jxm/J (Jax#003966); Ifnar1<sup>fl/fl</sup> B6(Cg)-Ifnar1tm1.1Ees/J (Jax#028256); Cx3cr1<sup>CRE</sup> (MMRRC, RRID:MMRRC\_036395-UCD), P2ry12<sup>CreERT2</sup> (Jax#034727, donated by Dr. Tom Arnold), Mavs<sup>-/-</sup> (Jax#008634), Cgas<sup>-/-</sup> (Jax#026554), Tlr3<sup>-/-</sup> (Jax#005217), 5xFAD (B6SJL-Tg(APPSwFILon,PSEN1<sup>+/+</sup>M146L<sup>+/+</sup>L286V<sup>+/+</sup>)6799Vas/Mmjx, RRID:MMRRC\_034840-JAX). In all experiments, both male and female mice were used with ages specified in the legends.

### Zebrafish

Fish were maintained in recirculating habitats at 28.5 °C and on a 14/10-h light/dark cycle. Embryos were collected after natural spawns and incubated at 28.5 °C. Larvae were imaged at 7 days post fertilization (dpf), a developmental stage at which sex cannot be determined. In this study, we used the double transgenic fish *Tg(mpeg:EGFP-CAAX);Tg(NBT:dsRed)* (zfin ID: ZDB-TGCONSTRCT-191211-1 and ZDB-TGCONSTRCT-081023-2) on a casper background to visualize microglia and neurons. All zebrafish protocols were approved by and in accordance with the ethical guidelines established by the UCSF Institutional Animal Care and Use Committee and Laboratory Animal Resource Center (LARC).

### METHOD DETAILS

#### Tamoxifen injections

To induce CreER activity in *P2ry12<sup>CreERT2</sup>* neonatal animals, pups were injected intra-gastric with 2 mg/mL tamoxifen (Sigma T5648) dissolved in corn oil (Sigma-Aldrich C8267) on days P1/P3/P4 (50 µg tamoxifen per day). Control pups were injected with 25 µl corn oil.

#### Whisker lesions

Whisker deprivation was performed under hypothermia-induced anesthesia and followed by topical application of lidocaine for pain management. Postnatal day 2 pups were anesthetized for 3 minutes in ice. An incision was made in the whisker pad along whisker rows B and D of one side of the face, and silver nitrate was used to cauterize the exposed whisker follicles in that row. After topical 2% lidocaine application the mice were reacclimated on a heating pad for at least 15 minutes before being returned to their home cage.

#### Immunohistochemistry and confocal microscopy

For all analyses of the barrel cortex, mice were perfused transcardially with ~10mL of ice-cold PBS followed by ~10 mL of 4% (weight/volume) paraformaldehyde (PFA) diluted in PBS. For analyses of SARS-CoV-2 infected brains, animals were not perfused and were postfixed by immersion in 4% PFA for 72 hours prior to cryoprotection and sectioning. All other brains were post-fixed in 4% PFA for a minimum of 4 hours and then transferred to a 30% sucrose solution for a minimum of 24 hours. Tangential sections (flat mounts) of the barrel cortex were obtained by dissecting the cortex from the diencephalon following perfusion and flattening the dissected cortices ventral side down between two cryomolds. The sections were placed in between flat toothpicks laid horizontally in the cryomold, and the second mold was pressed down on top of the toothpicks to maintain uniform thickness. Brains were then flash frozen and sliced on a HM 440E freezing microtome (GMI Instruments) or embedded in OCT following 30% sucrose treatment and frozen at -80°C for a minimum of 1 day and then sectioned on a CryoStar NX70 Cryostat (Thermo Fisher): glass mounted 16 µm sections or 35 µm floating sections were obtained for staining. Sections from control and deprived hemispheres of individual mice were mounted on the same slides for all experiments.

Immunohistochemistry was performed as follows: brain sections were incubated in a blocking solution consisting of 5% normal goat serum (Thermo Fisher) and 0.1% Triton (Sigma-Aldrich) diluted in 1X PBS. Primary antibodies were diluted in 5% normal goat serum in 0.1% Triton and tissue was incubated on a shaker overnight at 4°C. Secondary antibodies were diluted in 5% normal goat serum and tissue was incubated on a shaker for 2 hours at room temperature. Brain sections were mounted on coverslips with ProLong Gold or Glass (Thermo Fisher) for all imaging. For staining with IFITM3 (Thermo Fisher #11714-1-AP), secondary antibody staining was done with goat anti-rabbit IgG, HRP-linked (Cell Signaling Technology #7074) and visualized with TSA Plus Cy3 detection system (Akoya Biosciences #NEL744001KT). For staining with SARS-CoV-2 Spike and N protein antibodies (GeneTex) and BST2 antibody (R&D Systems, MAB8660-SP), an additional antigen retrieval step (70°C for 10min in 1X citrate buffer) was performed prior to blocking. For staining with 53BP1 and γH2AX, 1X TBS was used instead of 1X PBS and additional quenching step (50 mM NH4Cl/TBS for 5 min at RT) and permeabilization (1% TX-100/TBS for 20 min on ice) were performed prior to primary antibody incubation. Slides were imaged on an LSM 800 confocal microscope (Zeiss, Zen 2.6 software) using 20x, 40x, and 63x objectives. For analysis of phagocytic cups in Figure 3, slides were imaged on LSM 880 confocal microscope with AiryScan (Zeiss) using a 63x objective. The antibodies used are listed in the [key resources table](#).

#### Microglia CD68 volume

Z-stacks were collected on an LSM 880 confocal microscope with AiryScan (Zeiss) on Superresolution mode and a 63x objective (NA 1.4). Laser power and gain were consistent across each image. AiryScan processing was performed in Zen software (Zeiss) at a setting of 6 (“optimal” setting). Images were analyzed using Imaris software (Bitplane) by creating a 3D surface rendering of individual microglia, thresholded to ensure microglia processes were accurately reconstructed, and maintained consistent thereafter. Microglia rendering was used to mask and render the CD68 channel within each microglia. CD68 volume per microglia was then calculated as the total volume of masked CD68 volume within the masked GFP volume.

#### Microglia phagocytic compartment analyses

Phagocytic compartments, including phagocytic cups, phagosomes, and phagolysosomes, were identified as DAPI-enveloping structures that are distinct from the microglia nuclei. Unlike the microglia nuclear compartment, phagosomes lacked staining for IBA1 or GFP. Phagocytic cups lacked CD68 and only partially enveloped a DAPI+ and non-pyknotic cell. Microglia with bubble

morphology were identified by enlarged and rounded phagosomes or phagolysosomes that were larger than the microglia nucleus as described in Figure 4H. These phagocytic compartments contained DAPI<sup>+</sup> nuclear material undergoing pyknosis or karyorrhexis, which were very sparsely distributed within the phagosome. By contrast, non-bubble phagosomes tightly enveloped engulfed nuclear material such that the DAPI signal saturated the phagosome area.

Z-stacks were acquired using an LSM 880 confocal microscope with AiryScan (Zeiss) on Superresolution mode and a 63x objective (NA 1.4, 0.04mm pixel size, 16-bit depth) and processed as described above. Phagocytic compartments were analyzed in FIJI and ROI's were drawn around phagosomes using the Versatile Wand Tool plugin. The "tolerance" setting was manually adjusted to envelop the microglia phagocytic compartment surface and "connectedness" was set to 8-connected. An optical section was selected from the z-stack that represented the center of the compartment and mean intensity, integrated density, and area were then recorded for each phagocytic compartment. For analysis of phagocytic compartments in SARS-CoV-2 infected mice, images were first binned by average IFITM3 MFI per microglia. The maximum microglial IFITM3 mean fluorescence intensity per image across all samples was called 100%. The lower bin represents images with 0-50% of the maximum expression, and the higher bin represents images with 50-100% of the maximum expression. Each microglia was then manually scored for presence or absence of a phagocytic compartment as described above.

### Neuronal subtype counts

Images of the somatosensory cortex from P15 mice were acquired using an LSM800 confocal microscope at 20x magnification and 5x5 tiling in order to cover all cortical layers. All images were acquired in the same anatomical region, using the dorsal hippocampus as an anatomical reference point. Using FIJI software, ROI were drawn around each cortical layer identified using DAPI staining and measured. PV, SST and Gad67 staining were manually scored. CTIP2 and SATB2 analysis was automated: images were first corrected with Gaussian blur 2.0, then each cortical layer was individually analyzed after Li thresholding and numbers of positive neurons were determined with particle analysis (circularity 0.2-1.0, size 10µm-infinity and water-shedding). For each mouse, 3-4 sections were imaged and quantified. Stainings were done in at least 2 batches, each containing WT and mutant samples to control for technical differences and the data was normalized within each batch.

### Tunel staining

Tunel staining was conducted using the DeadEnd Fluorometric TUNEL system from Promega with adaptations from Paredes et al.<sup>117</sup> A hydrophobic barrier was drawn onto each slide surrounding 6-8 brain hemispheres. Tissue was postfixed in 4% PFA on ice for 20 minutes and rinsed in PBS 3X 5 minutes at room temperature. The tissue was then permeabilized using 20 ug/mL proteinase K (diluting the provided proteinase 1:500 in PBS) for 4 minutes at room temperature before washing in PBS 3X 5 minutes. Then 100 ul of equilibration buffer was added to the slide for 5 minutes while the incubation buffer was prepared as directed in the kit. The equilibration buffer was poured off and replaced with 50 ul of incubation buffer (45 ul Equilibration buffer, 5 ul nucleotide mix, 1 ul rTdT enzyme per slide) and covered with a provided plastic coverslip. The slides were then incubated in a humidified chamber in an oven at 37°C for 1h. The slides were immersed in provided 20X SSC diluted 1:10 with DI water for 15 minutes at room temperature, then washed in PBS 3X 5 minutes. Standard blocking, primary and secondary stains for other marker proteins (Iba1, CD68) were then carried out as described above.

### Fluorescent *in situ* hybridization

Fluorescent *in situ* hybridization (FISH) experiments were performed using the RNAscope Multiplex Fluorescent Reagent Kit v2 assay as described by the manufacturer for fixed-frozen tissue, but eliminating the 60°C incubation and post-fixation steps prior to tissue dehydration. Brains were embedded in OCT following 30% sucrose treatment and frozen at -80°C for a minimum of 1 day prior to sectioning. Mouse *Grin1* RNAscope Probe (ACD Bio #431611-C1), Mouse *Rbfox3* Probe (ACD Bio #313311-C2) and Mouse *Ifnar1* RNAscope probe (ACD Bio #512971-C2) were used to detect each transcript. For immunohistochemical labeling with antibodies following the RNAscope assay, tissues were incubated with blocking and antibody solutions as described above immediately after RNAscope and washing four times, 5 minutes each. Confocal optical sections were imaged on a Zeiss 700 at 63x magnification through layer IV of flattened *en face* cortical sections of the barrel cortex. The *Ifnar1* probe quantification was performed in the somatosensory cortex at P5-P7. Three images each from at least two sections each of three separate mice were counted per condition.

### Flow cytometry

For flow cytometry experiments, mice were transcardially perfused with ice-cold dPBS and brains were dissected out and placed in cold isolation media iMed<sup>+</sup>. Both cortices were then dissected out and processed. Microglia were isolated following this protocol.<sup>118</sup> Briefly, cortices dissected as described above were mechanically dissociated using a glass tissue homogenizer in isolation medium iMed<sup>+</sup>. Cells were filtered and then pelleted at 300g for 10min at 4°C before being resuspended in 22% Percoll (GE Healthcare Cat#17-0891-01) and centrifuged at 900g for 20min with acceleration set to 4 and deceleration set to 1 in order to remove cellular debris. Cells were then resuspended and stained in iMed<sup>-</sup> in either eppendorf tubes or a 96-well plate. Cells were analyzed on an BD FACSAria Fusion. Buffers were prepared as described in Galatro et al.<sup>118</sup>

iMed<sup>-</sup> [50 mL of HBSS 1× without phenol red; 750 $\mu$ L HEPES 1 M (f.c. 15 mM); 650 $\mu$ L glucose 45% (f.c. 0.6%); 100 $\mu$ L 0.5 M EDTA pH 8.0 (f.c. 1 mM)], iMed<sup>+</sup> [500mL HBSS 1× with phenol red, 7.5mL HEPES 1 M (f.c. 15 mM), 6.5mL glucose 45% (f.c. 0.6%)], Myelin gradient buffer [prepare 1.5 L of NaH<sub>2</sub>PO<sub>4</sub>·H<sub>2</sub>O (0.78 g/L; f.c. 5.6 mM), solution 1. Prepare 1.5 L of Na<sub>2</sub>HPO<sub>4</sub> 2H<sub>2</sub>O (3.56 g/L; f.c. 20 mM), solution 2. Adjust solution 1 to pH 7.4 with solution 2. Measure the final volume and add: 8 g/L NaCl (f.c. 140 mM); 0.4 g/L KCl (f.c. 5.4 mM); 2 g/L glucose (f.c. 11 mM). Autoclave and keep sterile at 4 °C], 22% Percoll [110 mL Percoll; 12 mL NaCl 1.5 M; 378 mL myelin gradient buffer]

### Measurement of lysosomal pH using Lysotracker

To assess the acidification of microglial phagolysosomes, we used LysoTracker staining, a pH sensitive dye which stains acidic compartments within a cell. For fixed tissue imaging, mice were perfused with ice-cold dPBS and cut into 200mm coronal sections on a vibratome in a supplemented media (HBSS Gibco Cat#14170161, 15mM HEPES, 0.6% glucose, 1mM EDTA pH 8.0). Sections containing the barrel cortex were incubated with Lysotracker Red at 1:5000 for 10 minutes, then washed and fixed overnight in 4% PFA before staining and mounting. 15mm z-stacks were acquired on a LSM800 and analyzed in FIJI. For flow cytometry based analysis of Lysotracker, we isolated live microglia from P5 mice cortex as described above and incubated cells in Lysotracker (100nM final concentration) together with the conjugated primary antibodies on ice for 20min before washing 3 times with cold iMed<sup>-</sup>. Samples were gated on CD45<sup>+</sup>CD11b<sup>+</sup> double positivity and MFI of Lysotracker signal was measured. To validate our staining, we included samples treated with Baflomycin A (lysosomal acidification inhibitor, 100nM final concentration) for 1h on ice prior to staining.

### SARS-CoV-2 virus propagation and plaque assay

All SARS-CoV-2 cell culture and animal work were performed in the Biosafety level 3 (BSL3). African green monkey kidney Vero-E6 cell line (ATCC#1586) and Calu-3 cells (ATCC# HTB-55) was obtained from American Type Culture Collection and maintained in Minimum Essential Medium (MEM, Gibco/Invitrogen) supplemented with 10% fetal bovine serum (FBS, Gibco 0437028), 1% Penicillin-Streptomycin-Glutamine (Gibco/Invitrogen) at 37°C in a humidified 5% CO<sub>2</sub> incubator. A clinical isolate of SARS-CoV-2 from a UCSF patient was propagated in Vero E6 cells and Calu-3 cells. 80% Confluent monolayers of Vero E6 cells grown in 6-well plates were incubated with the serial dilutions of virus samples (250 ul/well) at 37°C for 1 hour. Next, the cells were overlayed with 1% agarose (Invitrogen) prepared with MEM supplemented containing 2% fetal bovine serum(sigma), 1x penicillin/streptomycin/glutamine (100xPSG, Gibco). Three days later, the cells were fixed with 4% formaldehyde (PFA) for 2 hours, the overlay was discarded, and samples were stained with crystal violet dye.

### SARS-CoV-2 infection

5-6 weeks old hemizygous K18-hACE2 mice (Jax#034860, B6.Cg-Tg(K18-ACE2)2PrImn/J) were anesthetized with isofluorane and inoculated with 6x10<sup>4</sup> PFU of SARS-CoV-2 intranasally in a BSL3 facility. The mice were sacrificed at 3 and 6 days post- infection, and the brain was removed and fixed in 4% PFA for 72 hours before being sunk in 30% sucrose and embedded in OCT. 40  $\mu$ m sections were cut on a cryostat and stained as described above with 2 minute antigen retrieval at 95 degrees. Antibodies used include the following: rabbit anti-SARS-CoV-2 Nucleocapsid(N) (GeneTex, GTX135361), mouse anti-SARS-CoV-2-spike(S), (GeneTex, GTX632604).

### Tissue processing for MERFISH

For MERFISH experiments, nuclease-free reagents were used when possible. Two P7 C57Bl/6J and two P7 Aldh1l1<sup>eGFP</sup> animals were anesthetized by hypothermia and transcardially perfused with PBS, followed by 4% PFA. Brains were extracted and post-fixed in 4% PFA overnight. The brains were then put in a 30% sucrose solution for at least 24h, frozen in OCT, and stored at -80°C until sectioning. 10-12 $\mu$ m thick sections were cut using an NX70 cryostat at -18°C and adhered to MERSCOPE slides. Slides with tissue sections were processed as detailed in the MERSCOPE Sample Preparation protocol (Vizgen). Briefly, slides were washed three times in PBS and stored at 4°C in 70% ethanol until use. Samples from C57Bl/6J animals were stained using the MERSCOPE Cell Boundary Staining Kit. Samples from Aldh1l1<sup>eGFP</sup> animals were stained using rabbit anti-IBA1 and chicken anti-GFP. Samples were washed with Sample Prep Wash Buffer and then incubated with Formamide Wash Buffer at 37°C for 30min. Then, the Gene Panel Mix, which contains the MERFISH probes, was added and samples were incubated for 48h at 37°C. After hybridization, the samples were incubated in Formamide Wash buffer for 30min at 47°C two times. As per the protocol, samples were then embedded in a thin 4% polyacrylamide gel and treated with a clearing solution for 36h at 37°C. Slides were washed twice more in Sample Prep Wash Buffer and then stained with DAPI and poly-dT Staining Reagent. Slides were then washed with Formamide Wash Buffer and Sample Prep Wash Buffer. Then, slides were loaded into the MERSCOPE Instrument for data acquisition.

### MERFISH data processing and analysis

Output data from the MERSCOPE Instrument was loaded into the Vizgen MERSCOPE Vizualizer software. One to two fields of view (FOVs) spanning the somatosensory cortex were acquired for each animal, with *Ifnb1* as well as cell-type markers *Syp* (neurons), *Aldh1l1* (astrocytes), *Olig2* (oligodendrocyte lineage), *P2ry12* (microglia) and poly-dT to visualize cell soma. For each FOV, each *Ifnb1* punctus was identified and assigned to a cell-type of origin based on its colocalization with cell-type markers manually. Finally,

the percent of total *Ifnb1* puncti produced by a specific cell-type was quantified for neurons, astrocytes, oligodendrocytes, and microglia.

### Interferon β injection

A solution of 10ng interferon-β (IFN-β, R&D Systems, 8234-MB-010) diluted in PBS (2 $\mu$ l) was slowly delivered by intracerebroventricular injection into hypothermia-anesthetized P4 C57Bl/6J mice (coordinates: x = 1, y = 1.8, z = -2, from lambda) using a pulled and beveled glass pipette with 50 $\mu$ m outer diameter. Control mice were injected with an equal volume of PBS. The mice were perfused 24 hours later with ice-cold PBS followed by 4% paraformaldehyde, post-fixed in 4% PFA overnight at 4°C, cryoprotected and sectioned on a cryostat at 40 $\mu$ m (floating sections, used for IFITM3 quantification) and 18 $\mu$ m (slide-mounted sections, used for 53BP1 foci quantification). Images were acquired using the 40x objective of an LSM 800 (Zeiss) and 53BP1 foci+ neurons were manually counted using the Cell Counter tool in FIJI. 53BP1 foci+ neurons as a percentage of 53BP1 $^{+}$  nuclei was quantified in L2/3 within the region of IFITM3 $^{+}$  expression, which extended approximately 300 $\mu$ m from the injection site over primary and secondary motor cortex.

### Viral gain of function

Plasmids were created using VectorBuilder and received as purified plasmids. Plasmids were then packaged in the lab into ssAAV PHP.eB serotype envelopes following a protocol adapted from Negrini et al.<sup>119</sup> Briefly, a 15cm dish was seeded with 1.5x10<sup>7</sup> HEK293T cells and fresh DMEM Glutamax (Gibco 10566024) supplemented with 10% FBS and 1% Pen/Strep (Gibco 15140122) was added the day of transfection. For transfection, a mix was prepared containing 20 $\mu$ l helper plasmid (pAdDeltaF6), 7ug pUC-mini-iCAP-PHP.eB and 7ug AAV transgene plasmid diluted in 2.5mL OptiMEM (Gibco 31985070). Polyethenylamine diluted in 2.5mL OptiMEM was added to the plasmid mix at final concentration of 24 $\mu$ g/mL and incubated 15min at RT before pipetting on HEK cells. After 24h incubation, media was changed to 27mL OptiMEM. Cells were collected 60-72h later by scraping them from the dish and placing them in 50mL falcon tube. Chloroform was added at final concentration [1:10], cells were shaken vigorously and centrifuged at 3000g/5min/4°C. The supernatant was collected in a new tube, AAV precipitation solution (40% PEG8000, 2.5M NaCl) was added at final concentration [1:4] and incubated on ice minimum 1h before centrifugation 3000g/30min/4°C. Pellet was resuspended in 1.4mL 50mM HEPES pH 8.0 and incubated at 37°C for 20min with a mix of 14 $\mu$ l DnaseI (Sigma Aldrich D4263-5VL) and 1.4 $\mu$ l RNaseA (Thermo Fisher EN0531). Chloroform was added at concentration [1:1] and centrifuged at 3000g/5min/4°C. The aqueous phase was then added to an Amicon ultracentrifuge filter column and centrifuged at 14000g/5min/RT and flowthrough was discarded. The filter was washed 3x with dPBS. Column was eluted by flipping it upside down and centrifuged at 1000g/2min/RT. Viral solution was stored at 4°C. Viral titers were calculated based on Addgene protocol (<https://www.addgene.org/protocols/aav-titration-qpcr-using-sybr-green-technology/>) using the following qPCR primers: WPRE Fwd GGAGTTGTGGCCCGTTGTCAGG, WPRE Rev AGCTGACAGGTGGTGCAATGC. Control plasmid: pAAV[Exp]-SYN1>NLS-EGFP:WPRE. IFN $\beta$  expressing plasmid: pAAV[Exp]- SYN1>mIfnb1[NM\_010510.2](ns):P2A: NLS-EGFP:WPRE.

Plasmids and plasmid maps are available upon request.

Control (Syn1:NLS-EGFP) or IFN $\beta$  expressing virus (Syn1:mIfnb1:NLS-EGFP) were slowly delivered by bilateral intracerebroventricular injection (0.5 $\mu$ l/ventricle) into hypothermia-anesthetized P1 C57Bl/6J mice (coordinates: x = 1, y = 1.8, z = -1.5, from lambda) using a pulled and beveled glass pipette with 50 $\mu$ m outer diameter. Virus solution was diluted in saline at a final viral titer of 8.09x10<sup>9</sup> viral particles/ $\mu$ l. Mice were perfused 6 days later at P7 and brains were collected and processed as described above ("Immunohistochemistry"). For analysis, images were taken in regions of the somatosensory cortex with nuclear GFP $^{+}$  neurons.

### Poly(I:C) microinjection into zebrafish larvae

For poly(I:C) injection, 7 dpf *Tg(mpeg:EGFP-CAAX);Tg(NBT:dsRed)* zebrafish larvae were anesthetized with 0.2 mg/ml of tricaine in embryo medium. Larvae were injected with 2nl of 1 mg/ml poly(I:C) (Invitrogen) or PBS as a vehicle control into the optic tectal ventricle by microinjection. Zebrafish larvae were transferred to fresh embryo medium after injection for recovery and imaged at 4 hours post injection. We carefully monitored the larvae after injection to confirm that they recovered from anesthesia and did not exhibit abnormal swimming behaviors. Only healthy post-injection larvae were used for live imaging.

### Zebrafish live imaging

For live imaging, *Tg(mpeg:EGFP-CAAX);Tg(NBT:dsRed)* zebrafish larvae were anesthetized with 0.2 mg/ml of tricaine in embryo medium and mounted in 1.2% low-melting agarose gel on a glass bottom 35-mm dish (MatTek) and covered with embryo water containing 0.2 mg/ml tricaine. Time-lapse image was performed on a Nikon CSU-W1 spinning disk/high speed widefield microscope. We took time-lapse images from the optic tectum collecting 40-60 mm z-stacks (step size: 0.5 mm) at 5 min intervals for 30 min-1 hr. The images were processed by FIJI software. For analysis, we calculated the number of dsRed $^{+}$  neurons in microglia for the first 30 min of each video. For the analysis of process motility, we carefully observed each microglia process for the first 30 min of each video and classified all processes into three categories: 1) 'ramified' were defined as processes with or without movement that have no phagocytic cup formation, 2) 'cup formation' denoted processes with or without movement that contained or formed phagocytic cups, and 3) 'soma retraction' – processes that enclosed dsRed $^{+}$  cells that were subsequently trafficked toward the microglial soma).

**Quantitative PCR**

To extract RNA from cells isolated by FACS, freshly sorted cells were pelleted at 500 g for 10 minutes at 4° and then resuspended in RLT Plus buffer (Qiagen 1053393). Cells were vortexed and frozen for at least one day at -80° before being thawed on ice and processed for RNA using an Rneasy Plus Mini Kit (Qiagen). Purified mRNA was converted to cDNA with the High Capacity cDNA Reverse Transcription kit (Life Technologies) and amplified using either the Fast SYBR Green Master Mix (Thermo Fisher 43-856-12) and a 7900HT Fast Real-Time PCR System (Applied Biosystems).

**Generation of apoptotic cells**

The human neuroblastoma cell line, SH-S5Y5, was maintained in DMEM (Gibco 11965126) culture medium supplemented with 10% FBS and 1% Pen/Strep. To generate apoptotic corpses, cells were grown to 80% confluence and treated with 20uM Navitoclax (Bcl-2 family protein inhibitor,<sup>120</sup>) for 24h. We confirmed that >90% of the cells in the supernatant were dead cells (Trypan Blue<sup>+</sup>) (data not shown). Supernatant containing the dead cells was collected and centrifuged at 1000g/5min/RT. Cells were resuspended in PBS at concentration of 10<sup>6</sup>/mL. 1μl of 1 mg/ml pHrodo-SE (stock solution in DMSO, Thermo Fisher P36600) was added per 50 ml of cell suspension. Cells were incubated 30min at RT before washing twice in PBS before resuspending them in DMEM supplemented with 10% FBS and 1% Pen/Strep. Apoptotic cells were used immediately for microglia engulfment assays.

**Primary microglia culture and engulfment assay**

Mixed glia cultures were generated from P2-P4 pups from *Ifnar1*<sup>+/+</sup> or *Ifnar1*<sup>-/-</sup> and grown in T75 flasks with DMEM (Gibco 11965126) supplemented with heat inactivated 10% FBS (Gibco 10437028) and 1% Pen/Strep (Gibco 15140122) at 37°C 5% CO<sub>2</sub>. Media was changed the next day and cultures were grown for another 10-12 days. Microglia were detached by hitting the flasks 10x against the bench and plated in a 96-well plate at a density of 20 000 cells/well in 100ul final volume (4-6 replicate wells per condition). Cells were stained with Trypan blue (Invitrogen T10282) and counted using a Countess 3 Automated Cell Counter (Invitrogen). The next day, microglia were treated with vehicle or poly(I:C) (6ug/mL) and 10,000 pHrodo<sup>+</sup> apoptotic corpses (ratio 1:2) were added to the microglia 10-15min before the first image acquisition (T=0h). Images were acquired using an Incucyte S3 Live Cell Analysis Instrument (Sartorius) at 20x, 4 images per well, every hour for 24h total in 555nm red channel (apoptotic corpses within lysosomes) and phase contrast (microglia). Images were then thresholded using the Incucyte Software for Live Cell analysis and the integrated intensity of the red channel (apoptotic corpses within lysosomes) normalized to microglia surface area (determined with phase contrast) was used for analysis. This value was multiplied by 10<sup>3</sup> and is plotted as “pHrodo intensity (arbitrary units)” in Figures S4J and S4L. The slope of the curve was calculated by linear regression analysis from the peak of engulfment to T=24h for every well and normalized to WT untreated wells within each experiment. The value of the slope was multiplied by (-1) and plotted as “Digestion efficiency” in Figures S4K and S4M.

**Behavioral assay—Whisker nuisance test**

The whisker nuisance test paradigm was adapted from Balasco et al.<sup>72-74</sup> Mixed gender P15 littermate controls mice were used and a minimum of 2 experiments was performed for each genotype. Mice were habituated for 30 min to an empty cage previously rubbed with dirty bedding from their home cage. Each mouse was habituated to an individual cage on 3 consecutive days from P12 to P14. On the experimental day, the mouse was taken and placed in an empty cage rubbed with dirty bedding and habituated again for 30 min prior to the stimulation. Using the wooden end of a long q-tip, we then performed a sham stimulation, presenting the q-tip in front of the head of the mouse without touching it for a duration of 2 min followed by 3 consecutive 2 min trials gently stroking the whiskers on the right side of the face continuously, separated by 1 min intervals. All trials were recorded with a camera for later analysis. Using the video recording, five categories of behavioral responses to the whisker stimulation were scored as detailed in the table below. These parameters reflect increased avoidance, fear, and aggression towards the probe. Interpretation: Normal behavioral responses to stimulation were assigned a zero value, whereas meaningful abnormal behavioral responses were assigned a value of 2. The maximum whisker nuisance score is 10. High scores (6–10) indicate abnormal responses to the stimulation, in which the mouse freezes, becomes agitated or is aggressive. Low scores (0–3) indicate normal responses, in which the mouse is either soothed, curious or indifferent to the stimulation.

SCORE			
<b>BEHAVIORS</b>	0	1	2
<b>Response to stick</b>	Interested or ignore	Avoiding, anxious	Attacks, bites
<b>Evasiveness</b>	No evasive behavior	Runs away <50%	Runs away, moves to protect whiskers >50% time
<b>Grooming</b>	Normal grooming	No grooming	Irritated scratching, rubbing, pulling
<b>Freezing</b>	Walks around, exhibits curiosity	Frozen < 50% time	Frozen, defensive, fearful >50% time
<b>Breathing</b>	Normal range		Hyperventilating, gasping

### Single-cell sequencing preparation

B6 mice were perfused transcardially with ice-cold dPBS, mounted coronally in ice-cold isolation media (HBSS, 15 mM HEPES, 0.6% glucose, 1 mM EDTA pH 8.0) and 350 micrometer slices were prepared on a vibratome. A stereomicroscope was used to visually identify barrel regions; 1 mm<sup>3</sup> of tissue was collected per hemisphere. Microglia were isolated using tissue homogenization as described previously<sup>118</sup> followed by MACS bead isolation. Briefly, barrel cortices dissected as described above were mechanically dissociated using a glass tissue homogenizer in isolation medium (HBSS, 15 mM HEPES, 0.6% glucose, 1 mM EDTA pH 8.0). Cells were filtered and then pelleted at 300 g for 10 minutes at 4°C before being resuspended in 22% Percoll (GE Healthcare Cat#17-0891-01) and centrifuged at 900 g for 20 minutes with acceleration set to 4 and deceleration set to 1 in order to remove cellular debris. Pelleted microglia were then resuspended in staining media (PBS, 0.5% BSA, 2 mM EDTA) and incubated with CD11b MACS beads (Miltenyi, 1:50) for 15 minutes at 4°C. The cells were washed with staining buffer, pelleted at 300 g for 5 minutes at 4°C, and reconstituted in 500 µL staining buffer. Microglia were isolated as described in the manual for MACS LS columns and collected in staining buffer without EDTA, pelleted at 300 g for 5 minutes at 4°C, counted on a hemacytometer, and 15,000–20,000 cells were diluted in 30 µL in a BSA-coated plate for 10x sequencing.

### Microglial single-cell sequencing and analysis

Approximately 15,000 cells were loaded into each well of Chromium Chip B, libraries were prepared in-house as described in the 10x Manual, and sequenced on one lane of the NovaSeq S4 at the Chan-Zuckerberg BioHub.

Sequenced samples were processed using the Cell Ranger 2.1 pipeline (built on the STAR aligner)<sup>121</sup> and aligned to the GRCm38 (mm10) mouse reference genome. Clustering and differential expression analysis were conducted using Seurat version 3.1.4. Sequencing scripts can be found at <https://github.com/lcdorman/IFNresponseCode>, and original data can be found on GEO at GSE173173.

Microglial Isolation	
<b>Number of cells (thresholded)</b>	12,330 microglia
<b>Figures</b>	1 and 3
<b>Age</b>	Postnatal days 5 and 7
<b>Biological Replicates (mice)</b>	P5: 3 Males + 3 Females, P7: 1 Male + 3 Females
<b>Lanes</b>	4 (P5 Control/Deprived, 6 mice; P7 Control/Deprived, 4 mice)
<b>10x Chromium Kit</b>	Chip B/V3
<b>Feature thresholds</b>	2500–7500 genes/cell
<b>% Mitochondrial RNA thresholds</b>	0–7.5% mitochondrial RNA/cell
<b>Normalization</b>	Log normalization/scale factor 10,000
<b>Threshold for Diff. Exp. Analysis</b>	10% of cells expressing a gene
<b>Clustering resolution (Seurat)</b>	0.5

Sorted cells were sequenced using the 10x Chromium kit. Following alignment in Cell Ranger as described above, counts were imported into R and analyzed using the Seurat package.<sup>122,123</sup> Cells outside of the thresholds listed in the table were excluded from downstream analysis. Cells were identified as “female” or “male” based on their expression of the gene *Xist*; any cells expressing at least one count of *Xist* were labeled female, while all others were labeled male. Counts were then normalized, regressing out percent mitochondrial RNA and total counts per cell. The top 6000 most variable genes were used to calculate 50 principal components, and the top 30 PCs were used for nearest neighbor, UMAP, and cluster calculations with the resolutions shown in the table. Individual cell types were identified through calculation of marker genes using the Wilcox test for genes expressed in at least 50% of cells in the cluster and a natural log fold change of 1.2 or greater and adjusted p value less than 0.001.

Microglial and macrophage clusters were isolated based on expression of *Cx3cr1*, *Fcrls*, *P2y12*, and low expression of non-microglial genes. The filtered cells were re-normalized and analyzed with the Variance Partition package in R to determine the top genes determining sex, the first 8 of which were excluded from downstream analysis. The top 6000 most variable genes were used to re-calculate PCs, UMAP, and clusters. Clusters were determined using a resolution of 0.5, and the two sets of most closely related clusters (0/5 and 6/7) were combined due to low numbers of unique differentially expressed genes (log fold change >0.15, adjusted p-value < 10<sup>-5</sup>). Clusters were combined either due to relatively low numbers of uniquely upregulated genes (<30 between clusters 6/7, 34 between clusters 0 and 5). The resultant and remaining clusters had equal or more unique DEGs and importantly were not more closely related to any other clusters with few unique DEGs. Differential gene expression between clusters were calculated using the MAST test in Seurat. GO analysis was conducted using the Metascape webpage ([www.metascape.org](http://www.metascape.org)).<sup>22</sup> Volcano plots were generated using the EnhancedVolcano package in R, with gene labels chosen from the top differentially expressed genes. Cutoffs

were set at natural log fold change greater than 0.2 (22% increase) and adjusted p-value smaller than  $10^{-25}$ . Gene signature enrichment scores (Figures S1R and S3M) were calculated using Seurat's PercentageFeatureSet function.

#### Cell-cycle phase assignment

Cells were assigned to S phase, G1 phase, or G2/M phase (not distinguished) using a previously published dataset<sup>124</sup> and the CellCycleScoring function in Seurat.

**RNA Velocity analysis:** Spliced and unspliced transcript counts were calculated using Velocyto 0.17 and the velocyto run10x command with default settings. UMAP cell embeddings and annotation were exported from Seurat and used to plot all data shown. ScVelo 0.2.0 was run in Python and trajectories were calculated for all cells, then for each sample individually.<sup>55,116</sup>

#### Bar plot creation

Bar plots were created using ggplot2 in R. Coding details are available on github at ([https://github.com/lcdorman/IFNresponseCode/blob/main/P5\\_P7%20Microglia/D\\_BarPlots.Rmd](https://github.com/lcdorman/IFNresponseCode/blob/main/P5_P7%20Microglia/D_BarPlots.Rmd)). A table was made of cells per cluster per sample. Cell numbers were normalized by sample by dividing each entry by the total number of cells for that sample and multiplying by 2,000. Percents per cluster were then calculated by dividing the normalized cell numbers by the total number of cells in that cluster and multiplying by 100. Statistics were calculated individually for each cluster using a Chi-Square test on the raw cell numbers per cluster and sample. Plots with multiple bars had an additional Bonferroni correction applied, which multiplies the p-value by the number of comparisons.

#### Comparison with external bulk sequencing datasets

Computation can be found at [https://github.com/lcdorman/IFNresponseCode/blob/main/P5\\_P7%20Microglia/Comparison\\_otherdatasets.R](https://github.com/lcdorman/IFNresponseCode/blob/main/P5_P7%20Microglia/Comparison_otherdatasets.R). External dataset information was acquired from Friedman et al.,<sup>31</sup> Table S3. The IFN-1 cluster 8 upregulated gene signature was defined as any gene upregulated by at least 20% (log fold change  $>0.2$ ) with an adjusted p-value below 0.005 compared to all other clusters. This gene signature was then subset to include only genes whose log fold change values were shown in Friedman Table S3 for all the relevant genotypes. The log fold changes for each of the resulting 39 genes are shown in Figure 2A.

#### Comparison with external single-cell sequencing datasets

Computational details can be found at [https://github.com/lcdorman/IFNresponseCode/blob/main/P5\\_P7%20Microglia/revisions-singlecellmodel.Rmd](https://github.com/lcdorman/IFNresponseCode/blob/main/P5_P7%20Microglia/revisions-singlecellmodel.Rmd). The microglial sequencing dataset shown in this paper was used as a reference to which each dataset was aligned using a projection model described at <https://github.com/carmonalab/ProjecTILs>. Briefly, a new dimensional reduction was calculated for our dataset and the cells were then colored by the previously defined clusters. Each external dataset was projected onto this dimensional reduction, and the proportion of both control and treated cells that fell into the UMAP space occupied by Cluster 8 was calculated for each experimental condition. The ratio between these two proportions is plotted in Figure 2C.

## QUANTIFICATION AND STATISTICAL ANALYSIS

#### Statistical analysis

Graphpad Prism 9.3.1 was used for all statistical analyses of imaging data, and the Seurat package V3 in R was used for statistical analysis of single cell data. Statistical tests used, number of n replicates and p values are described in figures, text and figure legends, and in Table S4. All statistical analyses unless otherwise noted were performed on means of multiple technical replicates per animal. For sample sizes  $>15$ , normality of distribution was assessed using Kolmogorov-Smirnov test. In addition, for smaller sample sizes we visually evaluated the normal distribution of our data with QQ plots (Table S4). For all comparisons of two groups, we used t-test with Welch's correction to correct for unequal variance. For comparisons of multiple groups, equal distribution of variance was assessed on homoscedasticity (predicted values vs. residuals) plots.

Single cell RNA-seq data was analyzed in R as described in the methods section above. Categorical data shown in bar plots (cluster-specific differences in cell numbers) were analyzed in R using a Chi-Square test on each cluster with Bonferroni's correction for multiple comparisons. Statistical analyses were developed in collaboration with the UCSF biostatistics core, and summarized in Table S4. For all statistical tests shown: ns: non significant, \*p < 0.05, \*\*p < 0.01, \*\*\*p < 0.001, \*\*\*\*p < 0.0001.

## Supplemental figures

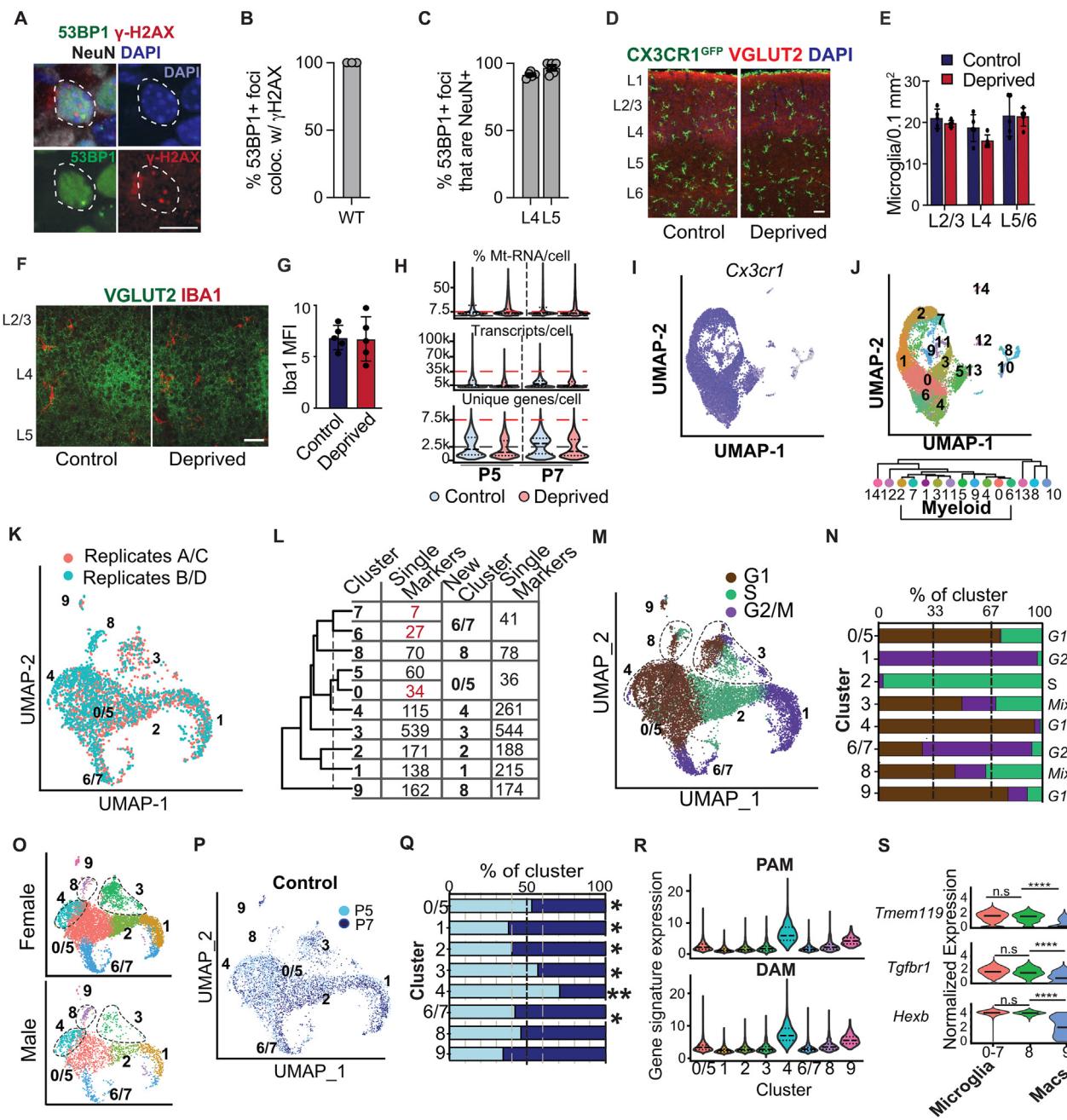


**Figure S1. Additional characterization of the partial whisker deprivation model and analyses of single-cell data, related to Figure 1**

- (A) Representative images showing colocalization of  $\gamma$ H2AX<sup>+</sup> and 53BP1<sup>+</sup> foci within a neuronal nucleus (NeuN<sup>+</sup>), P5. White circles outline the nucleus (scale bars, 5  $\mu$ m).
- (B) Percent of cells with 53BP1<sup>+</sup> foci that contained  $\gamma$ H2AX<sup>+</sup> foci at P5 in the wild-type barrel cortex ( $n = 3$  mice).
- (C) Percent of cells with 53BP1<sup>+</sup> foci that are NeuN<sup>+</sup> in the wild-type barrel cortex at P5 ( $n = 5$  mice).
- (D) Representative image of microglia (Cx3cr1<sup>GFP</sup><sup>+</sup>) at P7 in the barrel cortex (scale bars, 20  $\mu$ m).
- (E) Microglial density across cortical layers in control vs. deprived barrel cortex at P7 ( $n = 4$  mice).
- (F) Representative images of IBA1 intensity through control vs. deprived barrel cortex at P7 (scale bars, 25  $\mu$ m).
- (G) Quantification of IBA1 intensity through control vs. deprived barrel cortex at P7. Error bars show SD ( $n = 5$  mice).

(legend continued on next page)

- 
- (H) Quality control metrics for microglial single-cell sequencing in control and deprived conditions at P5 and P7. "% Mt-RNA/cell," mitochondrial RNA content per cell. Dashed lines indicate minimum and maximum threshold settings. Dotted lines inside violin plots represent median, 1<sup>st</sup> and 3<sup>rd</sup> quartiles.
- (I) Feature plot of myeloid marker *Cx3cr1* expression.
- (J) Unsupervised clustering of all thresholded cells. Clustering tree shows selected *Cx3cr1*<sup>+</sup> cells used in all subsequent analyses.
- (K) Comparison of biological replicates bioinformatically segregated via expression of male-specific (*Ddx3y* and *Eif2s3y*) and female-specific (*Xist* and *Tsix*) transcripts (replicate A: 3 female mice at P5, replicate C: 3 female mice at P7, replicate B: 3 male mice at P5; replicate D: 1 male mouse at P7).
- (L) Table showing the number of uniquely upregulated genes ( $|fc| > 0.15$ ,  $pAdj < 10^{-5}$ ) before and after combining clusters 6/7 and 0/5. The dotted line shows the clustering threshold used. The resultant clusters were not closely related to any other clusters with few unique DEGs.
- (M) UMAP plot showing cell-cycle phase assignment (annotation from Kowalczyk et al.<sup>124</sup>)
- (N) Quantification of cluster composition by cell-cycle phase. x axis = %cells per cluster in G1, S, or G2/M. Labels to the right indicate that cluster's predominant phase.
- (O) UMAP plots of cluster composition separated by sex.
- (P) UMAP plot showing cluster composition colored by age (P5 vs. P7) normalized for abundance.
- (Q) Quantification of cluster composition by age in control hemispheres. x axis represents percent of cells in each cluster from P5 (light blue) or P7 (dark blue) mice, normalized for the total number of cells per sample (chi-squared test with Bonferroni correction, \* $pAdj < 0.01$ , \*\* $pAdj < 10^{-25}$ ).
- (R) DAM gene signature expression by cluster (bottom). The signature represents the 83 genes upregulated by DAMs that were also expressed in this dataset ( $|fc| > 1.5$ ,  $pAdj < 10^{-8}$ ).<sup>30</sup> Dotted lines represent median and 1<sup>st</sup> and 3<sup>rd</sup> quartiles. PAM gene signature expression by cluster (top). The signature represents the 42 genes conserved between two published datasets of a developmental PAM signature that were also expressed in this dataset ( $|fc| > 1.5$ ,  $pAdj < 10^{-8}$ ).<sup>28,29</sup> Dotted lines represent median and 1<sup>st</sup> and 3<sup>rd</sup> quartiles.
- (S) Canonical microglial gene expression across microglial clusters 0–7 (pooled), microglial cluster 8, and putative macrophage cluster 9. Line shows median (MAST DE test, \*\*\* $p < 10^{-25}$ ).
- Data are represented as mean  $\pm$  SEM unless otherwise noted. Dots represent independent animals unless otherwise noted.

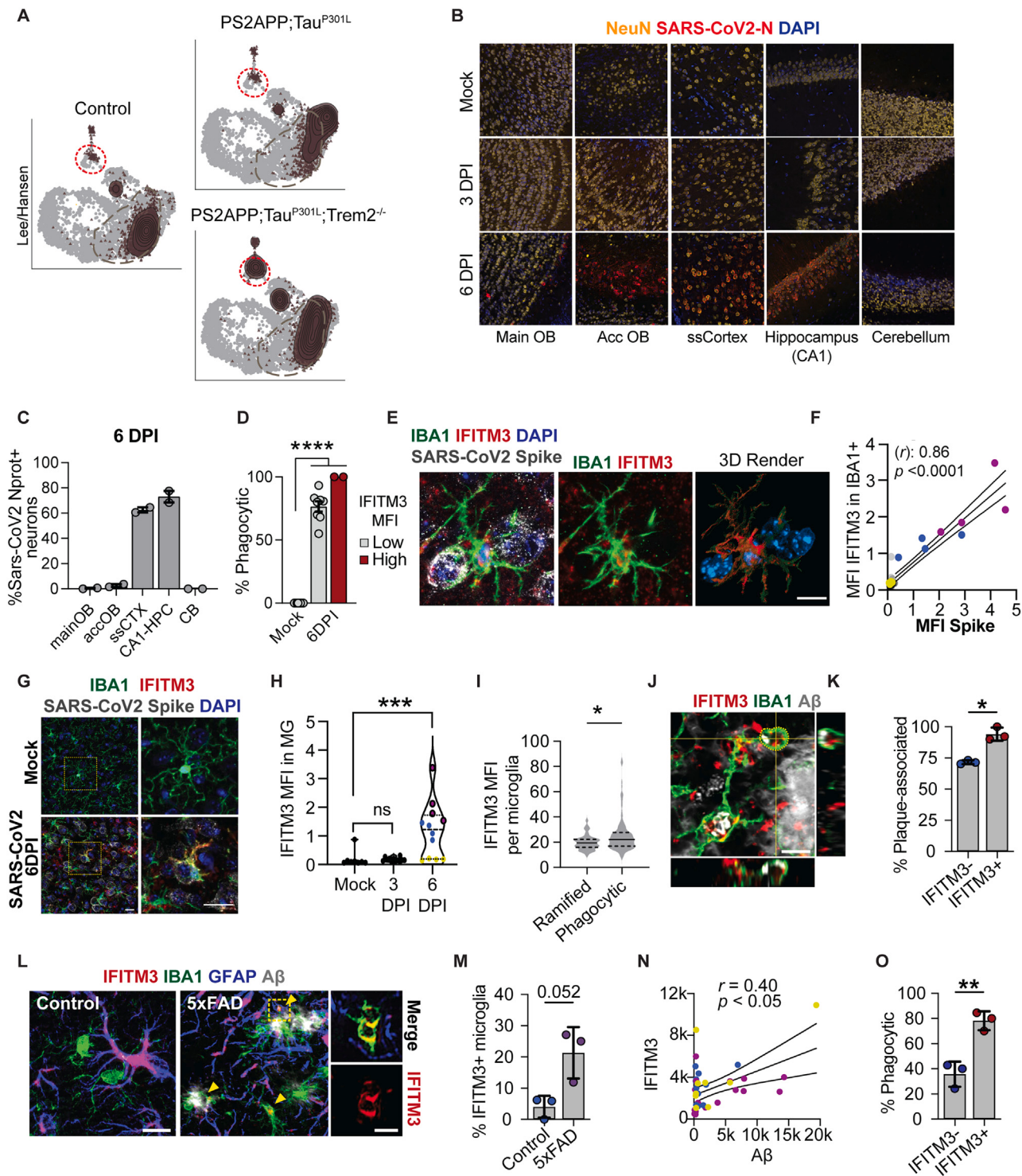


**Figure S2. Additional characterization of SARS-CoV-2 infection and AD models, related to Figure 2**

(A) Our microglial P5/P7 dataset (colored dots) was re-clustered to create a reference PCA and UMAP map to which other datasets (gray dots) were aligned. Brown triangles represent the external dataset from the Alzheimer's disease model dataset in Lee et al.,<sup>37</sup> red dotted circle highlight cluster 8, and gray dashed circle highlights homeostatic cluster 0/5.

(B) Representative images after mock infection, and 3 or 6 DPI, labeled for SARS-CoV-2 N-protein and NeuN (neurons). Main OB, olfactory bulb; Acc OB, accessory olfactory bulb; ssCortex, somatosensory cortex.

(C) Number of SARS-CoV-2 N-protein<sup>+</sup> cells in the indicated brain regions 6 DPI mice (n = 2 mice).

(legend continued on next page)

- (D) Percent phagocytic microglia (as defined by microglia containing DAPI-enveloping structures distinct from the microglia nuclei, see [STAR Methods](#) for details) in cortices of mock-infected vs. SARS-CoV-2-infected mice at 6 DPI, binned by IFITM3 expression per cell (see [STAR Methods](#) for details). Dot per image ( $n = 2$  mice per group).
- (E) Representative image and 3D reconstruction (3D render) of an IFITM3<sup>+</sup>IBA1<sup>+</sup> microglia engulfing a SARS-CoV-2-infected cell (Spike<sup>+</sup>) (scale bars, 10  $\mu\text{m}$ ).
- (F) Correlation of SARS-CoV-2 Spike protein with microglial IFITM3 mean fluorescence intensity per image. Each color represents an individual mouse ( $n = 3$  mice at 6 days post infection,  $r$  Spearman correlation coefficient = 0.86,  $p < 0.0001$ ).
- (G) Representative images in somatosensory cortex showing IFITM3 staining in IBA1<sup>+</sup> microglia from mock- vs. SARS-CoV-2-infected mice at 6 DPI (yellow square shows inset, scale bars, 20  $\mu\text{m}$ ).
- (H) Quantification of IFITM3 mean fluorescence intensity (MFI) within microglia. Data represented as violin plots with median in solid line, quartiles in dotted lines. Dot per technical replicate, colored by individual mouse ( $n = 2$  mock-infected mice, 3 each at 3 and 6 DPI).
- (I) Quantification of IFITM3 intensity in phagocytic and non-phagocytic (ramified) cells at 6 DPI. Data are represented as violin plots, median in black, quartiles in dotted line. Dot per cell ( $n = 40–145$  cells from 2 mice).
- (J) Confocal image and orthogonal projection of a plaque-associated IFITM3<sup>+</sup> microglia in hippocampus of 1 year old 5xFAD mouse showing A $\beta$ <sup>+</sup> (4G8 antibody) IFITM3<sup>+</sup> phagocytic cup (scale bars, 5  $\mu\text{m}$ ).
- (K) Percent of microglia in IFITM3<sup>+</sup> and IFITM3<sup>-</sup> populations within 10 mm of an A $\beta$  plaque in hippocampi of 1-year-old 5xFAD mouse ( $n = 3$  mice).
- (L) Representative images of microglia in hippocampi of 1-year-old control vs. 5xFAD, showing IFITM3, IBA1 (microglia), GFAP (astrocyte), and FSB dye (A $\beta$  plaques) staining. Inset (yellow dotted square) shows plaque-adjacent phagocytic cup (scale bars, 10  $\mu\text{m}$ ).
- (M) Percent IFITM3<sup>+</sup> microglia in control vs. 5xFAD hippocampi ( $n = 3$  mice per group).
- (N) Correlation of A $\beta$  with IFITM3 mean fluorescence intensity per phagocytic compartment. Dot per technical replicate, colored per individual mouse ( $r$  Spearman correlation coefficient = 0.40,  $p < 0.05$ ).
- (O) Percent of microglia in IFITM3<sup>+</sup> and IFITM3<sup>-</sup> populations containing a phagocytic compartment ( $n = 3$  mice).
- Data are represented as mean  $\pm$  SEM unless otherwise noted. Dots represent independent animals unless otherwise noted.
- Statistics: Kruskal-Wallis test (D and H), Mann-Whitney test (I), Welch's t test (K, M, and O).

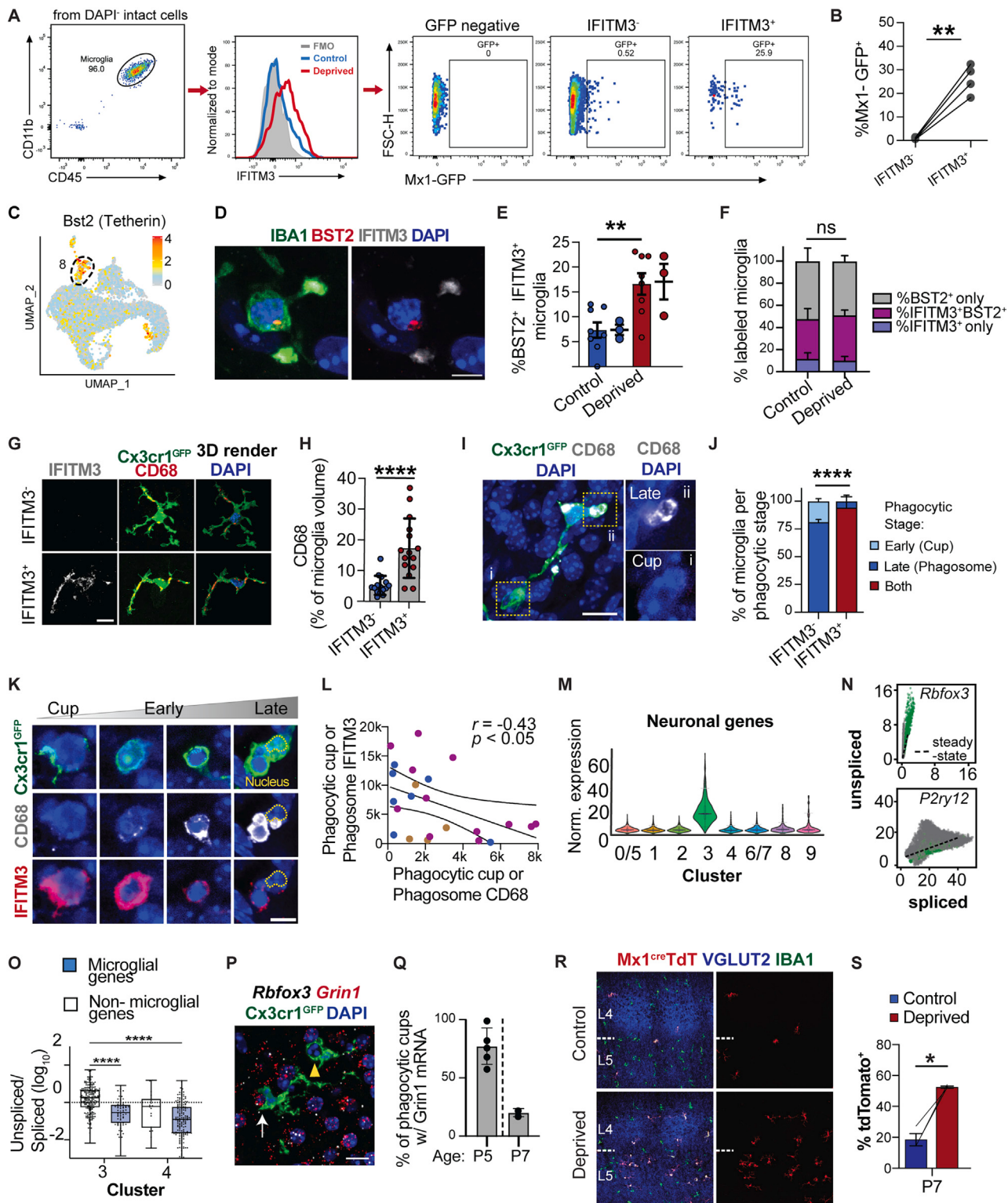
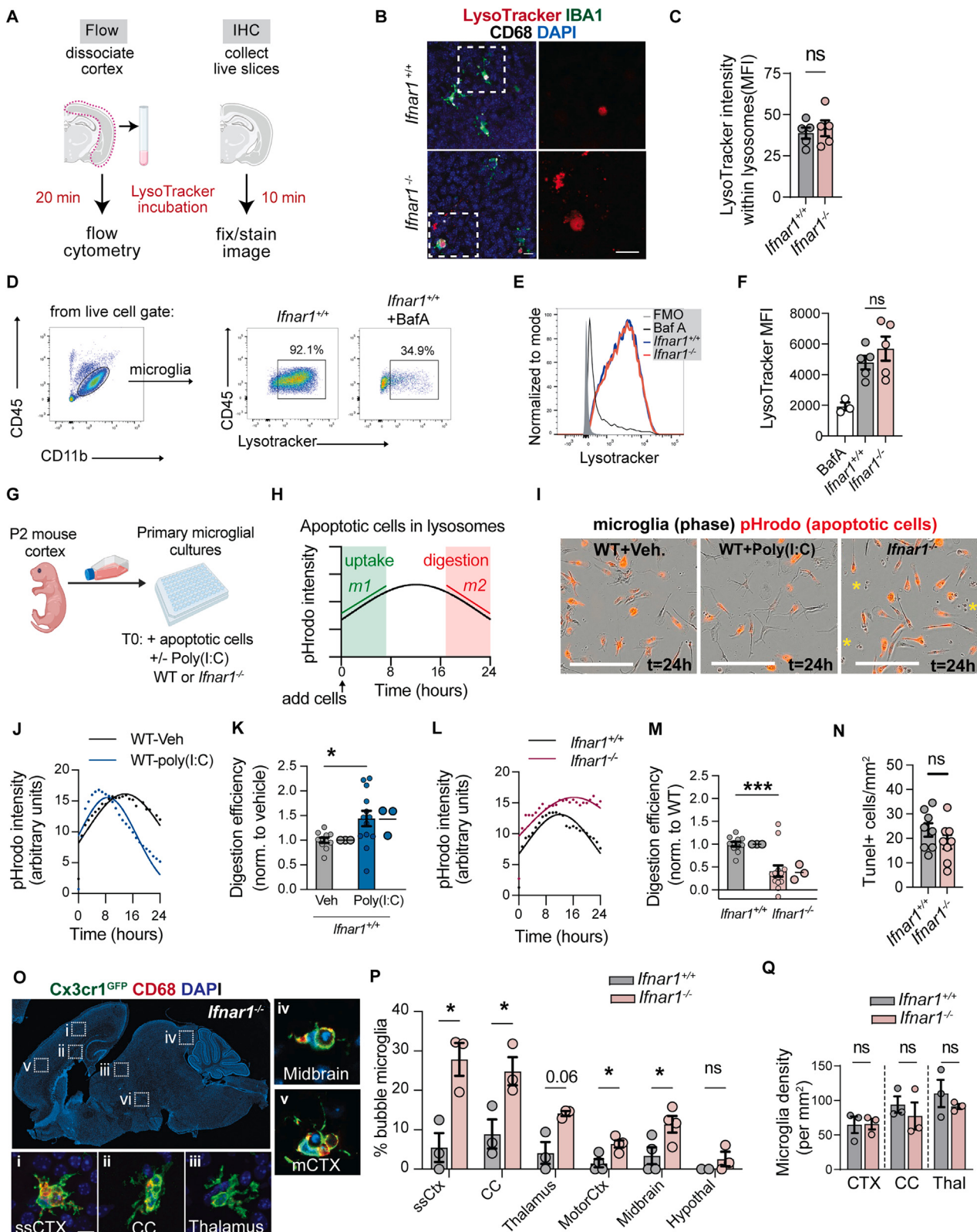


**Figure S3. Additional characterization of neuron-engulfing microglia during cortical remodeling, related to Figure 3**

(A) Representative gating of microglia (left), histogram of IFITM3 expression in CD11b<sup>+</sup>/CD45<sup>low</sup> microglia in control and deprived hemispheres at P5 (FMO, fluorescence minus one, negative control), and representative flow gating of Mx1<sup>GFP+</sup> microglia from IFITM3<sup>-</sup> vs. IFITM3<sup>+</sup> populations (right). (B) Mx1<sup>GFP+</sup> microglia within IFITM3<sup>+</sup> and IFITM3<sup>-</sup> populations at P5 (n = 4 mice).

(legend continued on next page)

- 
- (C) Feature plot showing normalized expression of *Bst2* in cluster 8 microglia.
- (D) Colocalization of BST2/Tetherin<sup>+</sup>, IFITM3<sup>+</sup>, and IBA1<sup>+</sup> microglia in deprived barrel cortex at P5 (scale bars, 10  $\mu$ m).
- (E) Percent microglia co-expressing BST2 and IFITM3 in control vs. deprived hemispheres, P5. Dot per image on the left, dot per mouse on the right ( $n = 8$  images per condition from 3 mice).
- (F) Percent IBA1<sup>+</sup> microglia expressing either IFITM3 only (blue), BST2/Tetherin only (gray), or both (purple), excluding double negative microglia, P5. Data are represented as a stacked bar graph  $\pm$  SEM ( $n = 3$  mice).
- (G) Representative images and 3D-rendering of CD68<sup>+</sup> lysosomes within IFITM3<sup>+</sup> and IFITM3<sup>-</sup> microglia in barrel cortex, P5 (scale bars, 10  $\mu$ m).
- (H) Percent CD68 volume of total microglial volume in IFITM3<sup>+</sup> and IFITM3<sup>-</sup> microglia, P5. Dot per cell (15 IFITM3<sup>-</sup> and 15 IFITM3<sup>+</sup> microglia from  $n = 3$  mice).
- (I) Representative image of a Cx3cr1<sup>GFP+</sup> microglia highlighting a phagocytic cup (i; CD68<sup>-</sup>, non-pyknotic DAPI signal, incomplete DAPI envelopment by microglial processes) and a late phagosome or phagolysosome at P5 (ii; CD68<sup>+</sup>, pyknotic DAPI signal, complete envelopment by microglial processes) (scale bars, 10  $\mu$ m).
- (J) Percent of early phagocytic cups and late phagosomes in microglia, P5 (microglia with no phagosomes not included in analysis). Data are represented as a stacked bar graph  $\pm$  SEM ( $n = 7$ –10 cells each from 3 mice per group).
- (K) Representative images showing changes in IFITM3 and CD68 expression at different stages of phagocytosis, P5 (yellow line outlines microglial nucleus, scale bars, 5  $\mu$ m).
- (L) Correlation between CD68 and IFITM3 mean fluorescence intensity per phagocytic compartment (either phagocytic cup or phagosome) at P5 ( $n = 23$  cells from 3 mice,  $r$  Spearman correlation coefficient =  $-0.43$ ,  $p < 0.05$ ).
- (M) Normalized expression of a neuronal eigengene across clusters, relevant to Figures 1I and 1J. The 45 differentially expressed genes in cluster 3 (natural log fold change  $> 0.25$ , pAdj  $< 1e-10$ ) that were neuron-specific (per Zhang et al.<sup>61</sup>) were used to define the eigengene. Data are represented as violin plots. Lines show 5<sup>th</sup>, 50<sup>th</sup>, and 95<sup>th</sup> percentiles.
- (N) Representative plots of transcript splicing state for a canonical neuronal gene (*Rbfox3*, which encodes NeuN) vs. a microglial gene (*P2ry12*). Each dot represents one cell; units are in transcript counts per cell. Green dots represent cluster 3; gray dots are cells in all other clusters.
- (O) Ratio of unspliced to spliced transcripts ( $\log_{10}$ ) for genes upregulated in clusters 3 and 4, for canonical microglial genes (blue) vs. genes enriched in other cell types (white). “Enriched” =  $10 \times$  higher FPKM in microglia than the mean of other cell types from Zhang et al.<sup>61</sup> Plots show range, median, and first to third quartiles.
- (P) Representative image of Cx3cr1<sup>GFP+</sup> microglia engulfing a DAPI<sup>+</sup> nucleus expressing neuronal mRNA transcripts *Rbfox3* and *Grin1* at P5. White arrow shows a microglial phagocytic cup that is not yet closed. Yellow arrowheads shows loss of mRNA detection upon phagocytic cup closure (scale bars, 10  $\mu$ m).
- (Q) Percent of microglial phagocytic cups enveloping nuclei containing *Grin1* transcripts in barrel cortex at P5 and P7 ( $n = 5$  mice at P5 and 2 mice at P7).
- (R) Representative images of TdTomato<sup>+</sup> cells (*Mx1*<sup>CRE</sup>;*Rosa26*<sup>LSL-TdT</sup>) in the barrel cortex co-labeled with microglial marker IBA1 and synapse marker VGLUT2 to highlight barrels at P7 (scale bars, 100  $\mu$ m).
- (S) Percent TdTomato<sup>+</sup> microglia from *Mx1*<sup>CRE</sup>;*Rosa26*<sup>LSL-TdT</sup> in control and deprived hemispheres at P7 ( $n = 3$  mice).
- Data are represented as mean  $\pm$  SEM unless otherwise noted. Dots represent independent animals unless otherwise noted. Lines connect values from the same mouse (B and S).
- Statistics: paired t test (B, E, and S), Fisher’s exact test (F and J), Mann-Whitney test (H), Welch’s ANOVA with Tamhane’s T2 test for multiple comparisons (O).



(legend on next page)

**Figure S4. IFN-I promotes phagocytic efficiency, related to Figure 4**

- (A) Schematic of lysosome acidification assay.
  - (B) Representative images of LysoTracker<sup>+</sup> lysosomes within microglia in *Ifnar1*<sup>+/+</sup> and *Ifnar1*<sup>-/-</sup> mice, P5 (scale bars, 10  $\mu$ m). Inset: microglia containing a LysoTracker<sup>+</sup> lysosome.
  - (C) LysoTracker mean fluorescence intensity (which reflects pH levels) within microglia in slices from *Ifnar1*<sup>+/+</sup> and *Ifnar1*<sup>-/-</sup> mice, P5 ( $n = 5$  mice per group).
  - (D) Gating strategy and representative flow plots of lysosome acidification in microglia using LysoTracker. After gating on scatter, doublets, and live cells, CD45<sup>+</sup>CD11b<sup>+</sup> microglia (left) were gated on LysoTracker, including controls incubated with LysoTracker + baflomycin A (BafA) to block lysosome acidification (right).
  - (E) Representative histogram of LysoTracker mean fluorescent intensity across conditions (FMO, fluorescence minus one).
  - (F) Quantification of LysoTracker mean fluorescent intensity by flow cytometry in P5 cortex ( $n = 3$  baflomycin-A-treated mice, 5 mice per genotype).
  - (G) Schematic of *in vitro* assay to quantify impact of IFN-I signaling on microglial phagocytosis of pHrodo-labeled apoptotic SH-S5Y5 cells by multiwell live cell imaging. Cells, and additives (poly(I:C)) added simultaneously at time = 0 (T0). See [STAR Methods](#) for details of apoptotic cell generation and validation.
  - (H) Schematic of typical phagocytosis curve. A slope of the linear regression of the pre-peak slope during the linear phase was used to estimate engulfment efficiency ( $m1$ ), and slope of the post-peak phase was used to estimate digestion efficiency ( $m2$ ).
  - (I) Representative images of primary microglial cultures 24 h after addition of pHrodo<sup>+</sup>-labeled apoptotic cells in WT microglia (left) or WT microglia with poly(I:C) 6  $\mu$ g/mL (middle), or in *Ifnar1*<sup>-/-</sup> microglia (right) (scale bars, 200  $\mu$ m, asterisks show apoptotic corpses).
  - (J) Representative intensity curves (dotted lines) and best fit (solid lines) from WT primary microglial cultures fed with pHrodo<sup>+</sup> labeled apoptotic cells at T = 0 h, with vehicle (black) or poly(I:C) (6  $\mu$ g/mL) (blue).
  - (K) Digestion efficiency shown as the inverse of slope  $m2$ , normalized to mean of control (see [Figure S4H](#)). Bars indicate technical replicates ( $n = 11$  vs. 13 wells) from three independent experiments (large dots show mean per experiment).
  - (L) Representative intensity curves and fitted lines from primary microglial cultures fed with pHrodo labeled apoptotic cells at T = 0 h, from *Ifnar1*<sup>+/+</sup> (black) or *Ifnar1*<sup>-/-</sup> animals (magenta).
  - (M) Digestion efficiency shown as the inverse of slope  $m2$  normalized to means of control (see [Figure S4H](#)). Bars indicate technical replicates ( $n = 11$  vs. 13 wells) from three independent experiments (large dots show mean per experiment).
  - (N) Density of TUNEL<sup>+</sup>DAPI<sup>+</sup> cells per mm<sup>2</sup> in the barrel cortex in *Ifnar1*<sup>+/+</sup> and *Ifnar1*<sup>-/-</sup> mice, P5 ( $n = 8$  mice).
  - (O) Representative images showing microglial morphology in different brain regions, P5 (scale bars, 50  $\mu$ m [left, low power], 10  $\mu$ m [inset, high power]). Regions include somatosensory cortex (ssCTX), corpus callosum (CC), thalamus (specifically ventroposteromedial thalamic nucleus), midbrain, and motor cortex (mCTX).
  - (P) Percent bubble morphology microglia in brain regions in [Figure S4O](#) in *Ifnar1*<sup>+/+</sup> and *Ifnar1*<sup>-/-</sup> mice, P5 ( $n = 3$ –4 mice per genotype). Thalamus quantification is from ventroposteromedial thalamus.
  - (Q) Microglial density in *Ifnar1*<sup>+/+</sup> and *Ifnar1*<sup>-/-</sup> mice by brain region, P5 ( $n = 3$  mice per genotype).
- Data are represented as mean  $\pm$  SEM unless otherwise noted. Dots represent independent animals unless otherwise noted.
- Statistics: Welch's t test (C, F, K, M, N, and P), two-way ANOVA with Sidak's post hoc test (Q).

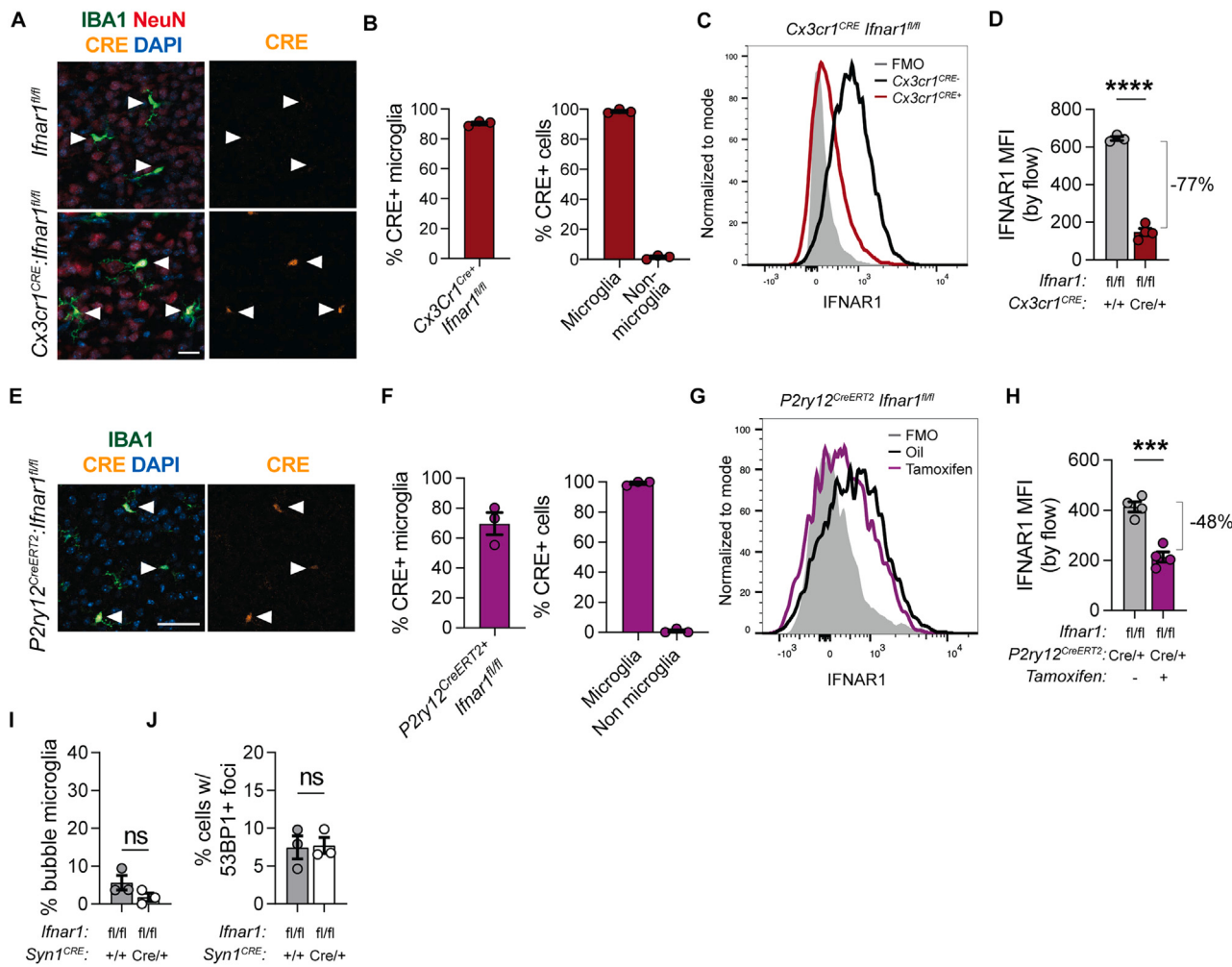


**Figure S5. Validation of myeloid and microglial conditional deletion strategies and impact of neuronal-specific deletion, related to Figure 5**

(A) Representative images showing CRE staining within IBA1<sup>+</sup> microglia in barrel cortex of P5 *Ifnar1*<sup>fl/fl</sup> mice (top) and *Cx3cr1*<sup>Cre/+</sup>:*Ifnar1*<sup>fl/fl</sup> mice (bottom) (scale bars, 20  $\mu$ m). White arrowheads show microglia nuclei.

(B) Quantification of percent of CRE<sup>+</sup> microglia in barrel cortex of P5 *Cx3cr1*<sup>Cre/+</sup>:*Ifnar1*<sup>fl/fl</sup> mice (left) and percent of CRE<sup>+</sup> cells that are microglia (IBA1<sup>+</sup>) vs. non-microglia (IBA1<sup>-</sup>) (n = 3 mice).

(C) Representative histogram of IFNAR1 staining by flow cytometry from cortex of P5 *Ifnar1*<sup>fl/fl</sup> mice (black) and *Cx3cr1*<sup>Cre/+</sup>:*Ifnar1*<sup>fl/fl</sup> mice (dark red) (FMO, fluorescence minus one). Gating strategy as in Figure S3A.

(D) Quantification of IFNAR1 mean fluorescent intensity by flow cytometry in P5 cortex (FMO value was subtracted) (n = 3 *Ifnar1*<sup>fl/fl</sup> mice vs. 4 *Cx3cr1*<sup>Cre/+</sup>:*Ifnar1*<sup>fl/fl</sup> mice).

(E) Representative images showing CRE staining within IBA1<sup>+</sup> microglia in barrel cortex of P5 *P2ry12*<sup>CreERT2</sup>:*Ifnar1*<sup>fl/fl</sup> mice (50  $\mu$ g tamoxifen at P1, P3, and P4) (scale bars, 20  $\mu$ m). White arrowheads show microglia nuclei.

(F) Percent of CRE<sup>+</sup> microglia (left) and percent of CRE<sup>+</sup> cells that are microglia (IBA1<sup>+</sup>) vs. non-microglia (IBA1<sup>-</sup>), all from barrel cortex of P5 *P2ry12*<sup>CreERT2</sup>:*Ifnar1*<sup>fl/fl</sup> mice given 50  $\mu$ g tamoxifen at P1, P3, and P4 (n = 3 mice).

(G) Representative flow cytometry histogram of IFNAR1 staining in cortex of P5 *P2ry12*<sup>CreERT2</sup>:*Ifnar1*<sup>fl/fl</sup> mice oil injected (black) or tamoxifen injected (purple) (FMO, fluorescence minus one). Gating strategy as in Figure S3A.

(H) Quantification of IFNAR1 mean fluorescent intensity by flow cytometry in P5 cortex from *P2ry12*<sup>CreERT2</sup>:*Ifnar1*<sup>fl/fl</sup> mice oil or tamoxifen injected (n = 4 per group).

(I) Percent bubble microglia in the barrel cortex from *Ifnar1*<sup>fl/fl</sup> vs. *Syn1*<sup>Cre/+</sup>:*Ifnar1*<sup>fl/fl</sup> mice, P5 (n = 3 mice per group).

(J) Percent of all cells containing 53BP1<sup>+</sup> foci in the barrel cortex from *Ifnar1*<sup>fl/fl</sup> vs. *Syn1*<sup>Cre/+</sup>:*Ifnar1*<sup>fl/fl</sup> mice, P5 (n = 3 mice per group).

Data are represented as mean  $\pm$  SEM unless otherwise noted. Dots represent independent animals unless otherwise noted.

Statistics: Welch's t test (D, H, I, and J).

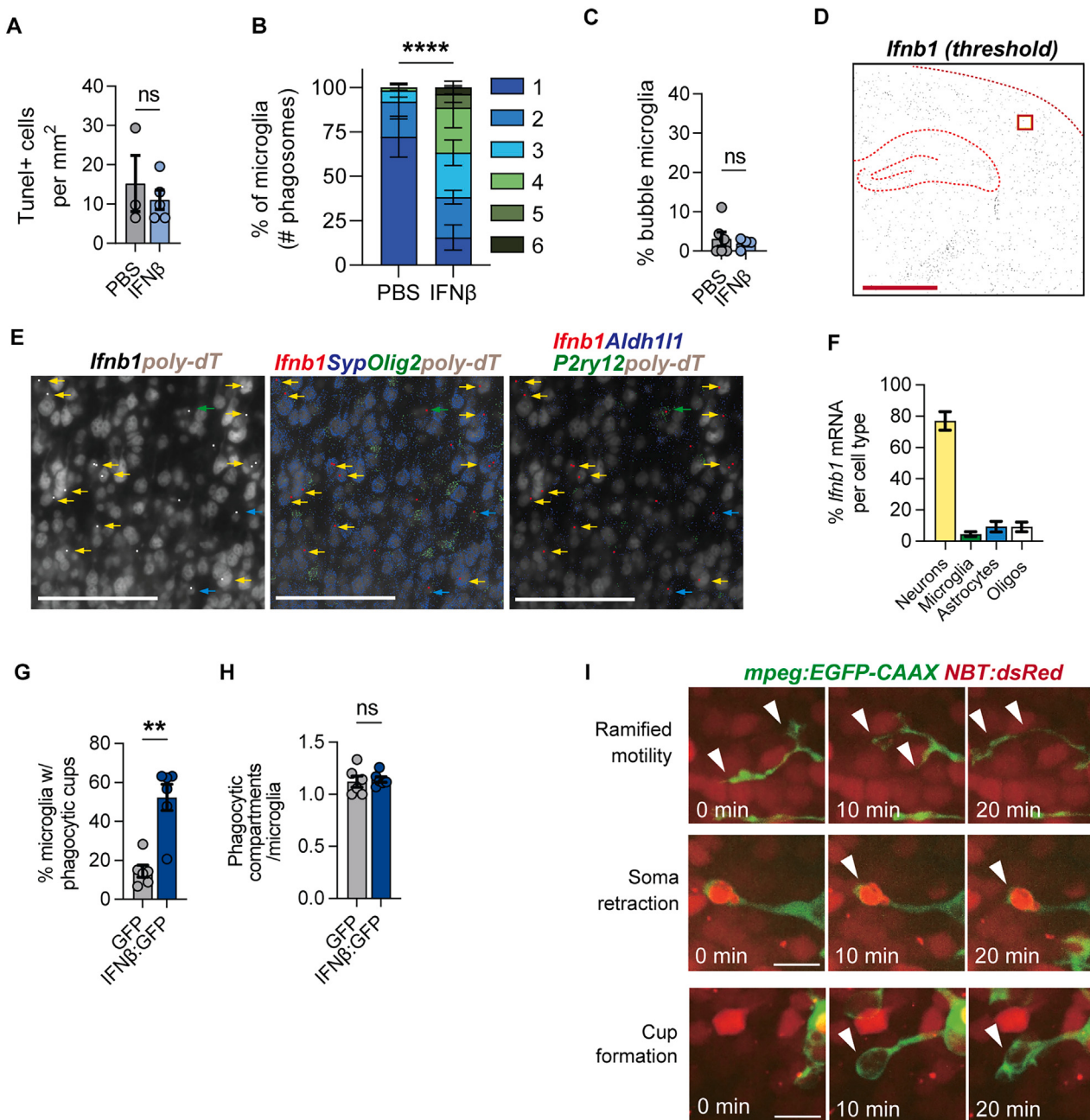


**Figure S6. Impact of gain-of-function models in mouse and zebrafish and cellular sources of Ifnb1, related to Figure 6**

(A) Density of TUNEL<sup>+</sup>DAPI<sup>+</sup> cells per mm<sup>2</sup> in PBS- vs. IFN- $\beta$ -injected mice motor cortex, P5 (n = 3 mice for PBS, 5 for IFN- $\beta$ ).

(B) Distribution of phagosome number per microglia among microglia with at least one phagosome in PBS- vs. IFN- $\beta$ -injected mice motor cortex at the injection site, P5. Data represented as a stacked bar graph  $\pm$  SEM (n = 36–37 cells per group from 5 mice per group).

(C) Percent bubble microglia in PBS- vs. IFN- $\beta$ -injected mice at P5. (n = 6 mice for PBS, 4 for IFN- $\beta$ ).

(D) Distribution of Ifnb1 mRNA in a low-power image of P7 mouse brain from MERFISH-based spatial sequencing. Black signal represents thresholded Ifnb1 signal for visualization. Dotted red lines indicate brain landmarks. Solid red box indicates inset area for (B) (scale bars, 1 mm).

(E) Representative images (inset region from A) of Ifnb1 mRNA together with cell-type-specific markers from MERFISH spatial sequencing. Ifnb1 is shown as white dots in the left panel and red dots in the middle and right panels. Grayscale background shows boundaries as detected by MERSCOPE imaging. Yellow arrows: Ifnb1 mRNA in neurons. Blue arrows: Ifnb1 mRNA in astrocytes. Green arrow: Ifnb1 mRNA in microglia. Puncta enlarged for visualization (scale bars, 250  $\mu$ m).

(F) Percent of Ifnb1 mRNA puncta detected in the respective cell types: neurons (Syp<sup>+</sup>, synaptophysin), microglia (P2ry12<sup>+</sup>), astrocytes (astro, Aldh1l1<sup>+</sup>), and oligodendrocyte lineage cells (oligo, Olig2<sup>+</sup>). Error bars show SD (n = 4 mice, 1–2 fields of view per mouse).

(G) Percent of microglia containing phagocytic cups in the barrel cortex at P7 after Ifnb1 overexpression in neurons (n = 6 per group).

(legend continued on next page)

- 
- (H) Average number of phagocytic compartments in microglia with at least 1 phagocytic compartment in the barrel cortex at P7 after *Ifnb1* overexpression in neurons ( $n = 6$  per group).
- (I) Representative images defining the following zebrafish microglial morphologies: ramified, cup formation, and soma retraction. White arrowheads show interactions between the microglial process (*mpeg:EGFP-CAAX*) and surrounding neuronal cell bodies (*NBT:dsRed*) (scale bars, 10  $\mu$ m). Data are represented as mean  $\pm$  SEM unless otherwise noted. Dots represent independent animals unless otherwise noted.
- Statistics: Welch's t test (A, C, G, and H), Fisher's exact test (B).

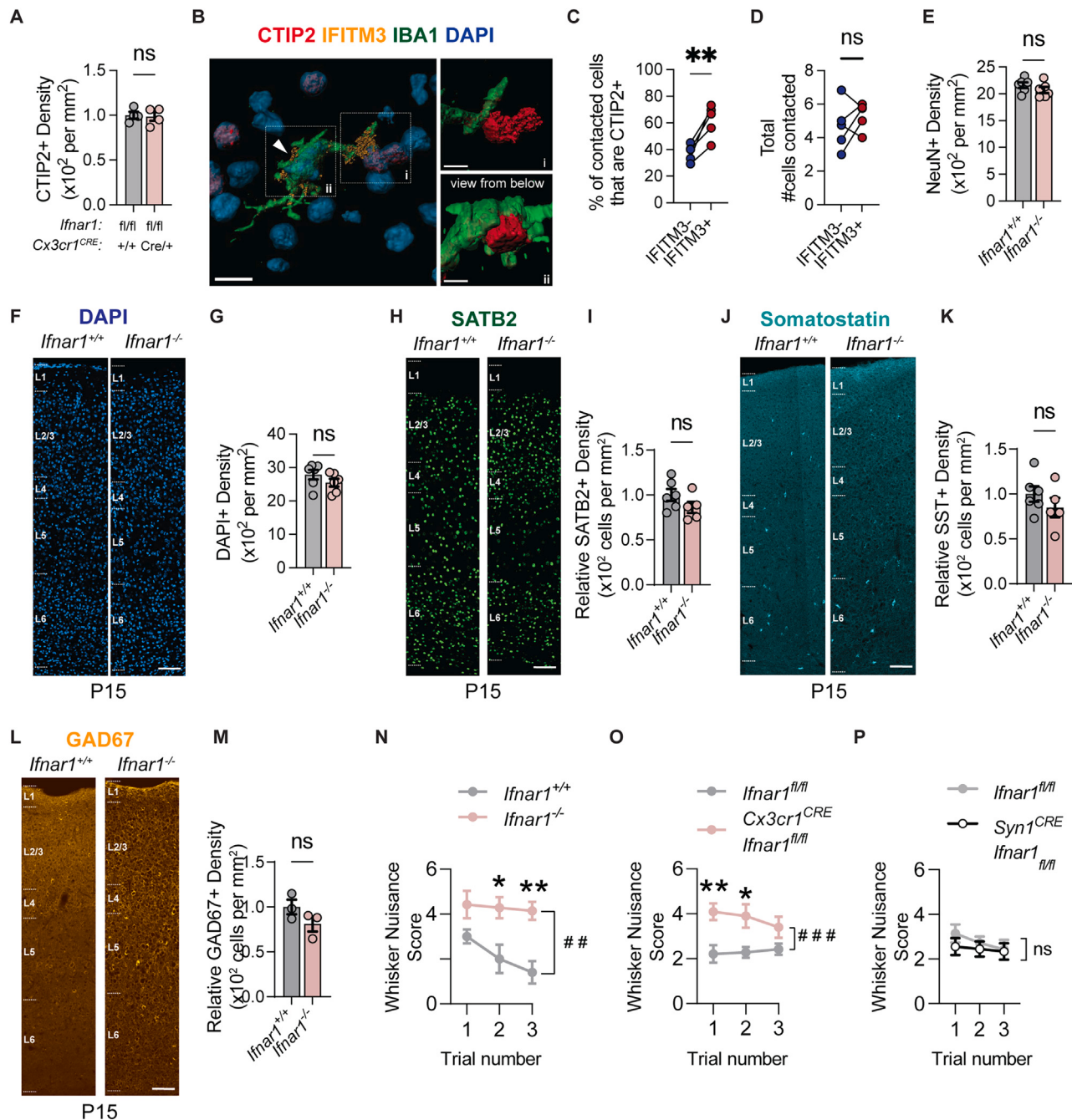


**Figure S7. Additional characterization of the cortical layers' alterations and tactile hypersensitivity, related to Figure 7**

- (A) Relative CTIP2+ neurons density in layer 5 in *Ifnar1*<sup>fl/fl</sup> vs. *Cx3cr1*<sup>CRE</sup>; *Ifnar1*<sup>fl/fl</sup> mice. (n = 4 mice per group).
- (B) 3D rendering of representative IFITM3+ microglia from WT-deprived cortex contacting a CTIP2+ neuron (insert i) and soma hugging another CTIP2+ neuron (insert ii, view from below) in barrel cortex L5, P5 (scale bars, 10  $\mu$ m).
- (C) Percent of CTIP2+ neurons among all cells contacted by IFITM3- vs. IFITM3+ microglia in WT-deprived cortex L5, P5 (n = 32 IFITM3- vs. 21 IFITM3+ microglia from 5 mice per group).
- (D) Total number of cells contacted by IFITM3- vs. IFITM3+ microglia in WT-deprived cortex L5, P5 (n = 32 IFITM3- vs. 21 IFITM3+ microglia from 5 mice per group).
- (E) Relative NeuN+ cell density in all cortical layers of the somatosensory cortex in P15 *Ifnar1*<sup>+/+</sup> and *Ifnar1*<sup>-/-</sup> mice (n = 6 mice per group).
- (F) Representative images of DAPI+ nuclei in the somatosensory cortex in P15 *Ifnar1*<sup>+/+</sup> and *Ifnar1*<sup>-/-</sup> mice. White dashed lines on the left highlight the cortical layers (scale bars, 100  $\mu$ m).
- (G) Relative DAPI+ nuclei density in all cortical layers of the somatosensory cortex in P15 *Ifnar1*<sup>+/+</sup> and *Ifnar1*<sup>-/-</sup> mice (n = 6 mice per group).

(legend continued on next page)

(H) Representative images of SATB2<sup>+</sup> neurons in the somatosensory cortex in P15 *Ifnar1*<sup>+/+</sup> and *Ifnar1*<sup>-/-</sup> mice. White dashed lines on the left highlight the cortical layers (scale bars, 100  $\mu$ m).

(I) Relative SATB2<sup>+</sup> neurons density in all cortical layers of the somatosensory cortex in P15 *Ifnar1*<sup>+/+</sup> and *Ifnar1*<sup>-/-</sup> mice (n = 6 mice per group).

(J) Representative images of Somatostatin<sup>+</sup> neurons in the somatosensory cortex in P15 *Ifnar1*<sup>+/+</sup> and *Ifnar1*<sup>-/-</sup> mice. White dashed lines on the left highlight the cortical layers (scale bars, 100  $\mu$ m).

(K) Relative Somatostatin<sup>+</sup> neurons density in all cortical layers of the somatosensory cortex in P15 *Ifnar1*<sup>+/+</sup> and *Ifnar1*<sup>-/-</sup> mice (n = 6 mice for *Ifnar1*<sup>+/+</sup> and 5 for *Ifnar1*<sup>-/-</sup>).

(L) Representative images of GAD67<sup>+</sup> neurons in the somatosensory cortex in P15 *Ifnar1*<sup>+/+</sup> and *Ifnar1*<sup>-/-</sup> mice. White dashed lines highlight the cortical layers (scale bars, 100  $\mu$ m).

(M) Relative GAD67<sup>+</sup> neurons density in all cortical layers of the somatosensory cortex in P15 *Ifnar1*<sup>+/+</sup> and *Ifnar1*<sup>-/-</sup> mice (n = 3 mice per group).

(N) Whisker nuisance score per consecutive trial in P15 *Ifnar1*<sup>+/+</sup> and *Ifnar1*<sup>-/-</sup> mice (n = 5 *Ifnar1*<sup>+/+</sup> mice, 7 *Ifnar1*<sup>-/-</sup>, 3 independent experiments, genotype factor p = 0.0013).

(O) Whisker nuisance score per consecutive trial in P15 *Ifnar1*<sup>flox/flox</sup> and *Cx3cr1*<sup>CRE:Ifnar1</sup><sup>flox/flox</sup> mice (n = 10 *Ifnar1*<sup>flox/flox</sup> mice, 14 *Cx3cr1*<sup>CRE:Ifnar1</sup><sup>flox/flox</sup>, 4 independent experiments, genotype factor p < 0.0001).

(P) Whisker nuisance score per consecutive trial in P15 *Ifnar1*<sup>flox/flox</sup> and *Syn11*<sup>CRE:Ifnar1</sup><sup>flox/flox</sup> mice (n = 7 *Ifnar1*<sup>flox/flox</sup> mice, 9 *Syn11*<sup>CRE:Ifnar1</sup><sup>flox/flox</sup>, 2 independent experiments, genotype factor p = 0.3666).

Data are represented as mean  $\pm$  SEM unless otherwise noted. Dots represent independent animals unless otherwise noted. Lines connect values from the same mouse (C).

Statistics: Welch's t test (A, E, G, I, K, and M), paired t test (C and D), two-way RM ANOVA with Sidak post hoc test (N and O).